Filamentation and Formation of Imposed Patterns in Low-Pressure Magnetized Electric Discharges: A Numerical Approach

By

Mohamad Menati

A dissertation submitted to the Graduate Faculty of
Auburn University
in partial fulfillment of the
requirements for the Degree of
Doctor of Philosophy

Auburn, Alabama
August 8, 2020

Keywords: Low-Pressure Plasma, Magnetized Plasma, Filamentation, Pattern Formation, Gridding Phenomenon, Dusty Plasma, Transport in Magnetic Field

Approved by

Uwe Konopka, Chair, Associate Professor of Physics
Edward Thomas, Jr., Co-chair, Charles W. Barkley Endowed Professor of Physics and Associate Dean for Research and Graduate Studies
Yu Lin, Professor of Physics
Stuart Loch, Professor of Physics
Konrad Patkowski, Associate Professor of Chemistry & Biochemistry

Abstract

Presence of strong magnetic fields ($B \geq 1.0\ T$) in magnetized dusty plasma experiments can result in a variety of phenomena in the background plasma and in the dust cloud. In the background plasma, the magnetic field induces a new type of filamentary structures that are extended in the plasma parallel to the external magnetic field. Filamentary structures are defined as regions within the plasma that have distinct properties such as optical brightness and appear in the plasma in different forms such as columns and target or spiral like structures. Some of the effects of strong magnetic field on dust particles include rotation of dust particles around the filaments and the formation of imposed, ordered structures in the dust cloud due to placing a wire mesh in the plasma bulk (gridding phenomenon). Gridding of a dust cloud suspended in a magnetized plasma is defined as the flow of the dust particles along paths which have the same shape and size of a metal mesh embedded in the bulk of the discharge. Both filamentation and gridding phenomena are primarily observed at high magnetic fields ($B \geq 1.0\ T$) and low pressure ($P \leq 100\ m\ Torr$)/low-temperature electric discharges (electron temperatures of few electron-volts and room temperature ions) and therefore they are thought to be originating from the same underlying physics. To investigate the origin and the characteristics of these phenomena, a 3-dimensional (3D) fluid model has been developed that can reproduce the experimental observations and enables us to investigate the physics of the filamentation and gridding phenomena. In this 3D model, plasma fluid equations are solved along with Poisson's equation. The simulation using this model revealed that filamentation is the consequence of the difference between the reduced diffusion of the electrons and ions across the magnetic field. In the presence of strong magnetic fields, electrons mainly flow parallel to the field lines while the less magnetized ions can also have a limited cross-field

diffusion which results in non-ambipolar diffusion of the plasma. This non-ambipolar diffusion is thought to be the underlying physics behind filamentation phenomenon.

Acknowledgment

To Dr. Edward Thomas, Jr., Charles W. Barkley Endowed Professor and Associate Dean for Research and Graduate Studies, I cannot thank you enough. Thank you for the great opportunity to be a member of MPRL, for guiding me through this project and for your patience until the end. Thank you for providing the chances to travel, to meet new people, and to learn. You have set such a high standard as a researcher, leader, and mentor for me that if in my future career I get to be half as good as you are, it would be a great success.

To Dr. Uwe Konopka, Thank you for all the helps, precious hints, and valuable discussions during this project. This project would never get where it is without your guidance and your brilliant thoughts. I cannot thank you enough for what I have learned from your professionalism and your knowledge in physics. Thank you also for all the jokes that always made the discussions and the learning process even more interesting.

To my Committee members, Dr. Lin and Dr. Loch for serving on my committee and all the helps throughout these years at Auburn University. Thank you to Dr. Patkowski for his time and effort serving as my university reader. Also, Thank you to all MPRL group members, past and present.

To my mom and dad who their hard work, sacrifices, and support got me from a small village on the borders of Iran to where I am standing right now. There are absolutely no words in Kurdish, Persian, and English that could describe what you have done for me and my siblings. Also, thank you to my beloved siblings for their supports and all friends and family who helped me along the way.

Table of Contents

List of Figures

List of the Tables

List of Abbreviations

CCP …… Capacitively Coupled Plasma

MDP ……...…. Magnetized Dusty Plasma

MDPX ……. Magnetized Dusty Plasma eXperiment

T ……... Tesla

Pa ……... Pascal

m Torr ...…… milli Torr

eV ……. electron Volt

RF …….. Radio Frequency

mm ……..……..... Millimeter

cm ……..……. Centimeter

2D ……...……2-dimensional

3D ……...……... 3-dimensional

HPEM …….....… Hybrid Plasma Equipment Model

SOR ……..... Successive Over Relaxation

PDE ……..……..…….. Partial Differential equation

1 Introduction

****It has to be noted that parts of this dissertation have been already published in a few articles** [1]- [5].

Plasma is a combination of electrons, ions and usually neutral atoms that move in random directions and is often electrically neutral. Debye Shielding is the main characteristic of plasmas through which the charged particles in the plasma exhibit collective behavior in shielding any source of electric potential [6]. By increasing the temperature of a solid to its melting temperature, it becomes liquid and increasing the temperature of the liquid converts it into gas. If the gas temperature is then sufficiently increased, the gas molecules can decompose to create a mixture of neutral atoms, electrons and ions which is called plasma state. Therefore plasma is usually called the fourth state of matter [7].

In another definition, complex (dusty) plasma, is defined as a four-component plasma which includes electrons, ions, neutral gas atoms, and charged solid particles. These dust particles in dusty plasmas can have diameters from nanometers to microns. Due to higher mobility of the electrons compared to ions, the dust particles usually become negatively charged in a laboratory dusty plasma [8] [9]. In these systems with micron-sized particles, the dust can acquire charges of the order ~1000 to 5000 elementary charges [10] [11]. Therefore, considering their large mass (~10^{-14} to 10^{-15} kg for silica dust particles) compared to the mass of electrons and ions, the charge-to-mass ratio of the dust particles is quite small ($10^{-12} - 10^{-13}\ e/m_e$, where "e" is the elementary charge and m_e is the mass of an electron) [12]-[14].

Many of the plasma environments, such as the plasmas in fusion devices and astrophysical systems, are subjected to magnetic fields [15] [16]. Therefore, recent interest in dusty plasma

physics has included investigation of magnetized dusty plasmas (MDPs) in which an external magnetic field is applied to magnetize the electrons, ions, and eventually the dust particles. Due to the small charge-to-mass ratio of the dust particles, large magnetic fields of $B \geq 1.0$ T are needed in order for the magnetic force on the dust particles to be comparable to the other forces that are acting upon them. With the recent development of relatively low cost, low maintenance variable field superconducting magnets that can produce magnetic fields of several Tesla, it has now become technologically feasible to explore phenomena in low temperature, weakly ionized plasmas that are subjected to high magnetic fields. As a result, this regime, which has been relatively unexplored, has become accessible and experiments reveal a wide variety of previously unidentified plasma and dusty plasma phenomena. This work seeks to develop a self-consistent numerical model to understand the behavior of low temperature plasma under the influence of large magnetic fields and make qualitative comparisons with experimental observations.

A commonly used configuration for studying MDPs is a parallel plate capacitively coupled plasma (CCP) sustained in a rare gas such as argon having pressures of a few to hundreds of Pa's (Pascal), at powers of a few to tens of Watts with external magnetic fields of the order $B \geq 1.0$ T applied perpendicular to the electrodes. The presence of strong magnetic fields in the plasma experiments with and without dust particles can lead to phenomena such as shear flow and Kelvin-Helmholtz instabilities [17]-[19], $E \times B$ drift of the plasma and dust particles [20], dust particle charge fluctuation [21], dust crystallization [22] and, of particular interest to the current work, plasma filamentation and gridding of the dust particles [23]-[28].

The filamentation phenomenon is defined as the formation of optically bright structures that are extended in the bulk of the magnetized plasma parallel to the magnetic field. By contrast, the gridding phenomenon is the alignment of dust particles in MDPs to the spatial structure of a

metal mesh placed in the plasma bulk or in the top electrode. Through this work, it will be shown that the gridding phenomenon arise from the plasma filaments imposed by the metal mesh embedded in the plasma and filamentation and gridding phenomena indeed share the same underlying physics. Through the results of numerical simulations, the underlying physics behind these two phenomena will be studied.

1.1 Formation of Filamentary Patterns in Magnetized Plasmas

Pattern formation and self-organization have been observed in a variety of natural and laboratory systems [29]-[39]. In plasma systems, self-organized patterns have been observed in arc discharges [40]-[45], glow discharges [46]-[48], streamers [49]-[51] and dielectric barrier discharges [52]-[54]. Examples of these pattern formations in plasmas are displayed in figure 1.1. This section will discuss a few different types of pattern formation in plasmas especially the formation of filamentary structures in low-pressure, low-temperature magnetized plasmas.

Plasma environments that produce self-organized patterns often have large aspect ratios, suggesting that plasma-surface interactions play a dominating role [55] in these phenomena. For a cylindrical plasma chamber, aspect ratio is defined as the ratio of the radius of the chamber to its height. In a magnetized plasma, the motion of the charged components is further limited across the magnetic field lines and therefore it takes longer for the charge species to diffuse across the magnetic field to the side walls of the plasma chamber. As a result, the presence of the magnetic field increases the effective aspect ratio of the plasma and it can support the formation of self-organized structures.

The presence of the magnetic field can stimulate instabilities in the plasma that, in return, can lead to the formation of self-organized patterns. In the low temperature isothermal plasma

regime, Kent et al. performed experiments and modeling of self-organization triggered by a transverse Kelvin-Helmholtz instability in a Q-machine [19]. In their experiments the neutral gas pressure was very low ($P = 2\times10^{-4}\ Pa$), the electron and ion temperature was about $0.2\ eV$, and the magnetic field was varying from $0.05\text{-}0.5\ T$. Shear-flow instability in plasmas under the influence of a magnetic field ($B \leq 0.5\ T$) can lead to vortex or spiral structure formation as was reported in the references [56]-[58]. The main characteristic of this type of pattern formation is the flow of the plasma in the chamber. Also, Driscoll et al. reported on how relaxation of a 2D turbulence in a magnetized electron column (a single component plasma) can develop filamentary structures [59].

Multiple numerical and analytical models have been developed to explain pattern formation in magnetized plasmas. Evolution and saturation of Kelvin-Helmholtz instabilities at the interface of a shear flow configuration in the presence of parallel and antiparallel magnetic fields, have been investigated by Keppens et al. [60]. Kono et al. [61] [62] reproduced the formation of spiral structures in a magnetized rotating plasma using numerical simulations and showed that the degree of thermodynamic non-equilibrium and thermal instability play the main role in this type of pattern formation.

It is noted that in the aforementioned examples, self-organized patterns form in magnetized electric discharges in which the plasma is either isothermal ($T_e=T_i$) at very low-pressure and low-temperature regime [19], single species electron plasma [59], flowing against a wall, or it is in rotation inside the plasma chamber to impose Kelvin-Helmholtz or shear-flow instabilities to appear [56]-[62]. The strength of the applied magnetic field in these experiments could be as high as $0.5\ T$.

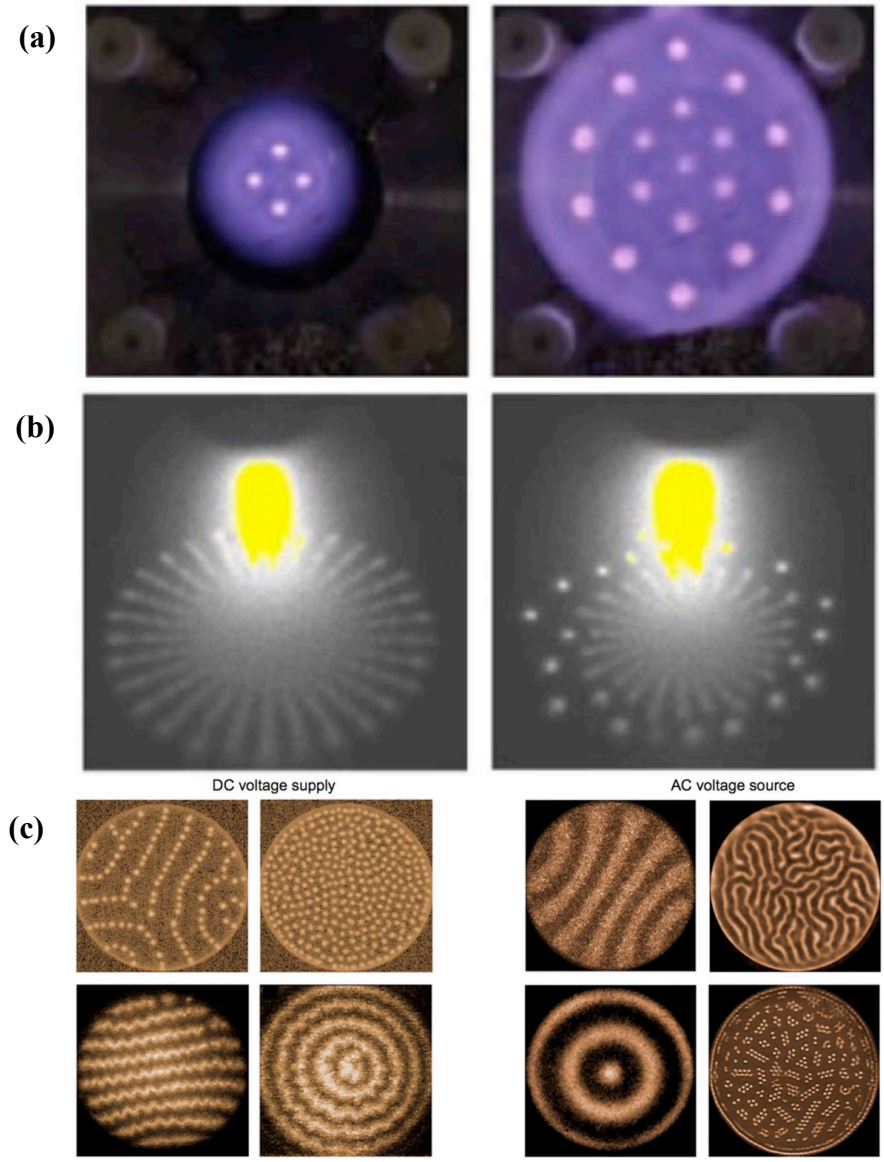

Figure 1.1: Examples of pattern formation in plasma. (a) Patterns in a high-pressure argon dielectric barrier discharge [53]. (b) Patterns in atmospheric pressure glow discharge, [46]. (c) Different patterns in DC and AC planar discharges, [47] and [48].

Self-organized patterns are also likely to form in stationary plasmas at low gas pressures ($P \leq 40$ Pa), low power deposition (power ≤ 40 W), non-isothermal low temperature (electron temperature ≤ 5 eV and room temperature ions) exposed to strong magnetic fields (magnetic field ≥ 0.5 T) [23]-[25] [63]. In this regime, single column plasma filaments and/or filamentary patterns form parallel to the magnetic field and perpendicular to the electrodes of the plasma chamber. These filamentary structures are diagnosed by their optical emission and bridge the inter-electrode gap in the plasma. The filaments are typically non-stationary and often form patterns of dots, circles and spirals when viewed from the top [24]. The typical spacing of the filaments is a few millimeters having a width or diameter of 1-2 millimeters. The filaments appear to maintain their gap-crossing bright structures while moving horizontally parallel to the electrodes. This motion may be oscillatory with a spatial period of up to *1 cm* or moving many millimeters to a few centimeters, from one quasi-stationary position to another.

The first observations of the phenomena were reported by Konopka et al. [23] and it was further studied by Schwabe, et al. [24] and Bandyopadhyay et al. [64]. In these works, different aspects of pattern formation in magnetized RF-plasmas have been investigated as a function of pressure and magnetic field strength. More recent experiments using the Magnetized Dusty Plasma eXperiment (MDPX) at Auburn University [25] have confirmed a number of the earlier observations. [2] [25]-[27] [65]

An experimental example of these filamentary structures is shown in figure 1.2. Here, the filaments are observed in visible light emission from an argon CCP plasma in the MDPX device at Auburn University. The filaments form between a powered, *30 cm* diameter, lower electrode and a grounded, *30 cm* diameter, upper electrode that has a *15 cm* diameter hole that is covered by an indium-tin-oxide (ITO)-coated (i.e., conducting surface) glass plate. The filaments are viewed

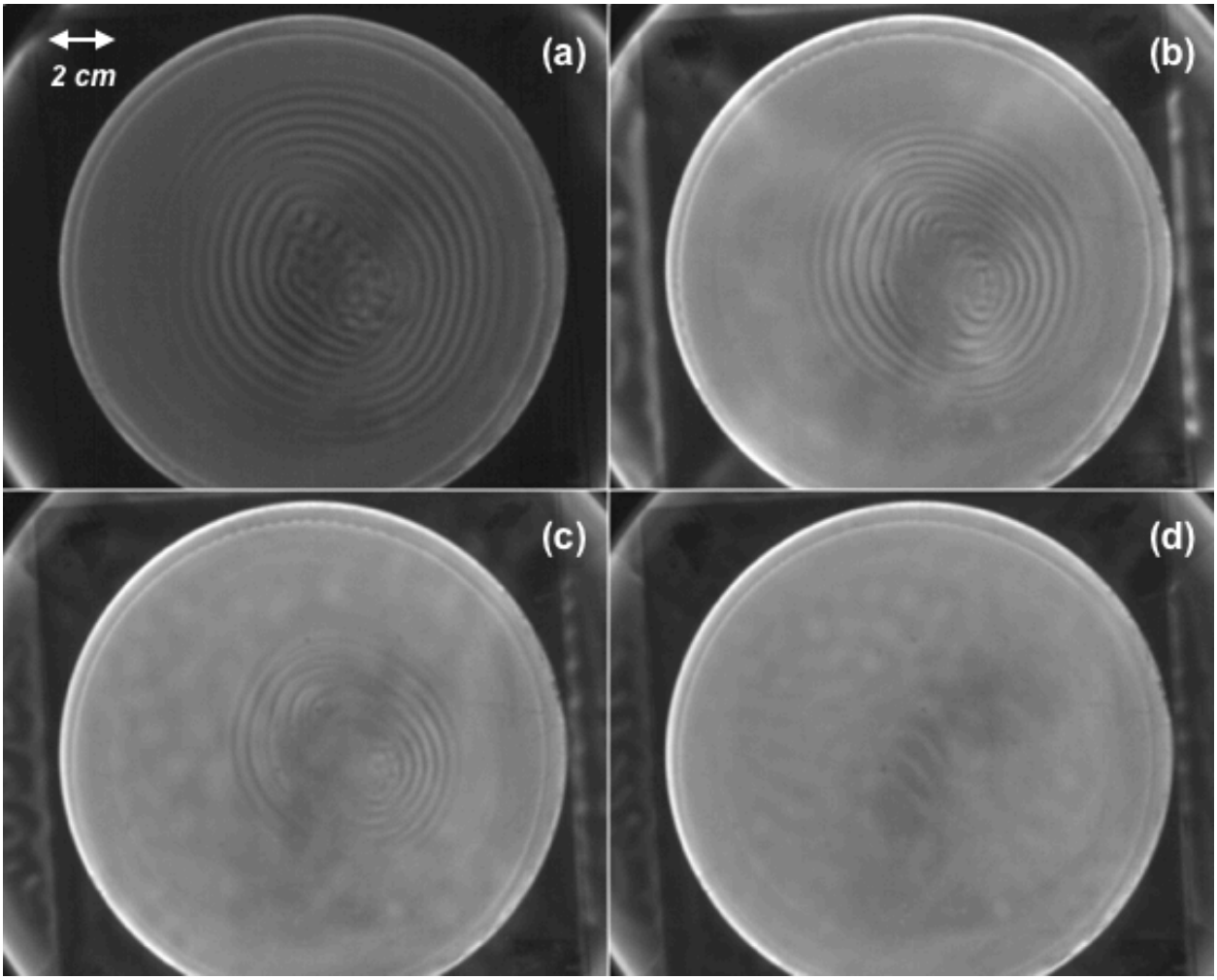

Figure 1.2 Filaments observed in the visible light in an argon CCP plasma in the Magnetized Dusty Plasma Experiment (MDPX) device. The filaments are viewed through an indium-tin-oxide coated glass plate embedded in the top electrode. The gray "spots" and spiral structures are the filaments that are formed in the plasma. The neutral pressure is p = 13.3 Pa and the magnetic field was B = 1.0 T. The applied RF power is increasing from: (a) 5 W, (b) 15 W, (c) 25 W and (d) 40 W. At low power, individual filaments (near the center) and concentric circular structures are observed [1].

through a *25 cm* diameter viewport from above the vacuum chamber. For this experiment, the neutral pressure was fixed at p = 13.3 Pa and the magnetic field was $B = 1.0\ T$. The applied RF power is increasing from figure 1.2(a) to 1.2(d). At low power, individual filaments (near the center) and concentric circular structures are observed. With increasing power, the individual filaments and the circular structures become less pronounced and start to fade.

Unlike pattern formation in other plasma regimes, this recent category of pattern formation is lacking an extensive study. Exploring plasma pattern formation in the presence of strong magnetic fields could also help to explore filamentary pattern formation imposed by a metal mesh placed in the bulk of the plasma and the appearance of gridding phenomenon.

1.2 Gridding Phenomenon in Magnetized Dusty Plasma Experiments

In dusty plasmas, under conditions of B ≥ 0.5 T and in the presence of shaped electrode boundaries (e.g., using a wire mesh), it has been observed that the dust particles levitated in the plasma can form "imposed, ordered structures" whose spatial patterns reflect the spatial ordering of the electrode boundaries [26]-[28]. The appearance of this "gridding" phenomenon and the filamentation occur under similar conditions in the plasma. Although these are distinct features of plasmas and dusty plasmas at high magnetic fields, their concurrence suggests that they may arise in the plasma as a result of similar physical principles. This section will begin with a discussion on the observed properties of the gridding phenomenon and will discuss the potential similarities with the filamentation.

Dusty plasmas are unique platforms for the study of non-ideal systems. The Coulomb coupling parameter is defined for dusty plasmas as $\Gamma = Z_d q^2 N_d^{1/3}/T_d$, where Z_d is dust charge number, q is the elementary charge, N_d is the dust particles number density and T_d is the particles

kinetic temperature [67]. This parameter is a measure of Coulombic potential energy compared to the random thermal energy of the system [66]. Γ can have a range that extends from much less than 1 (i.e., gas-like behavior) to several hundred (i.e., solid-like behavior), making dusty plasmas an ideal platform for investigating thermodynamic transitions [67]-[70], soliton wave propagation [71] [72], and self-organization [73]-[75]. Also, These plasmas have been a topic of interest in studying astrophysical objects [76], such as interstellar clouds [77] [78], planetary rings [79] [80], comet tails [81] [82], and controlled plasma systems [83] such as fusion devices where hot ablated material from the walls can cause disruptions [84] [85]. In a variety of low temperature plasma applications, such as plasma etching for microelectronics fabrication [86] or nano-particle synthesis in plasma, [87] [88] controlling the presence of these solid particles can be of technological and industrial importance.

Recently, Thomas et al. [26] [27] reported on the observation of a new phenomenon in MDPX device at Auburn University. In these studies in which a wire mesh was embedded in the top electrode of the MDPX, it was observed that at magnetic fields of $B \geq 0.5\ T$, the dust particles would begin to flow along paths which had the same shape and size of the mesh. These imposed ordered structures were primarily observed at high magnetic fields and low pressure ($P \leq 40\ Pa$). Hall et al. [28] noted that the behavior of the dust particles in the imposed structures are correlated to the ion dynamics. It was shown that the effects of the imposed, ordered structures become more prevalent as the ions became increasingly magnetized. It is thought that the presence of the wire mesh, imposes a spatial potential structure that can trap the dust particles. An example of this phenomenon [28] is displayed in figure 1.3. The figure shows the imposed flow of the dust particles matching the spatial structure of a metal mesh placed below the top electrode in the MDPX device. The image of the dust particles flow is obtained by summing over 600 video frames.

Since the wires width and their spacing are very small ($\leq 1\ mm$), this mesh configuration would not allow for spatially resolved probe measurements. Therefore, a wide mesh (called "waffle" electrode) was designed to enable detailed probe measurements beneath the mesh wires (see figure 1.4). In the experiments on gridding phenomenon using the newly designed "waffle" electrode, it was shown that the location where the dust particles get trapped beneath the mesh wires can vary with the width of the mesh. Figure 1.5 shows the side-view of the position of dust particles beneath the "waffle" electrode.

In figure 1.5, the locations of the wires of the "waffle" electrode are indicated using red rectangles. The yellow arrows point to the dust particles. The position of the dust particles is displayed for two cases with and without applied magnetic field and a neutral pressure of $3.3\ Pa$. At $B = 0$ the dust particles are randomly distributed beneath the "waffle" electrode and do not get affected by it, while at $B = 1.02\ T$, the dust particles are mostly trapped beneath the edges of the "waffle" electrode wires. As mentioned earlier, because of the very fine structure of the narrow mesh displayed in figure 1.3.a, it is not experimentally possible to define the exact location of the trapped dust particles in that experiment (figure 1.3.b) with respect to the mesh wires.

1.3 Motivation of the Work

The dust pattern formation and filamentation of magnetized plasmas can occur simultaneously in the plasma and the presence of dust particles does not significantly affect the filamentation [24]. Both phenomena critically depend on the magnetic field and neutral gas pressure and only appear in plasmas/dusty plasmas that are exposed to strong magnetic fields($B \geq 0.5$ T). The neutral gas pressure is an important factor in both filamentation and gridding as both processes become degraded at high pressures [24] [28]. Therefore, the motivation of this work was

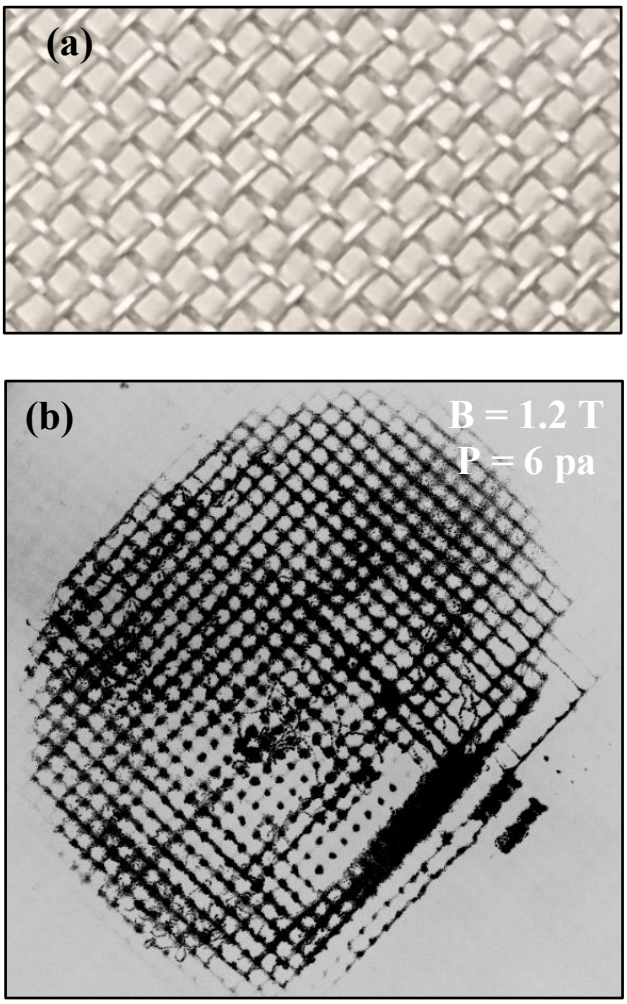

Figure 1.3 An example of gridding phenomenon in magnetized dusty plasma experiments. a) The metal mesh that is placed below the top electrode in the MDPX device. b) Summed image of the dust particles flow through paths imposed by the spatial structure of the metal mesh in (a) [28].

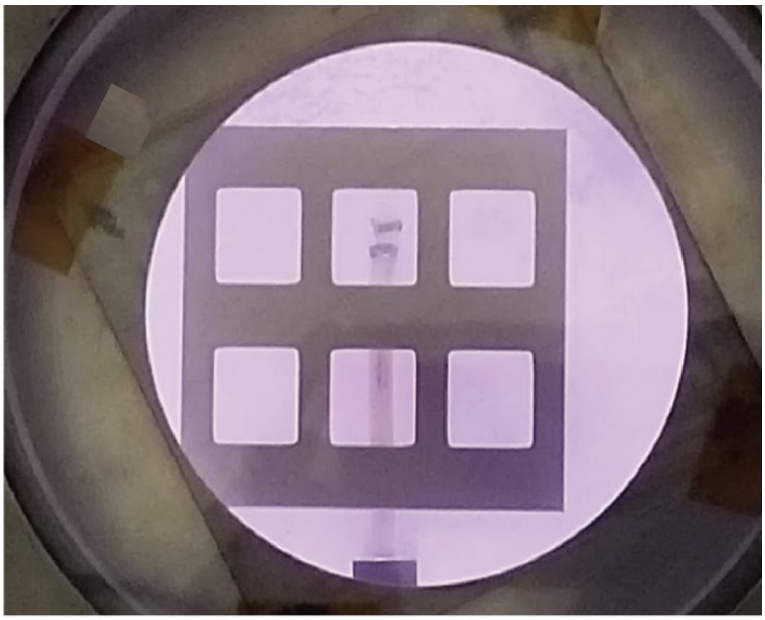

Figure 1.4: Top down view of the "waffle electrode in the vacuum chamber of MDPX [3].

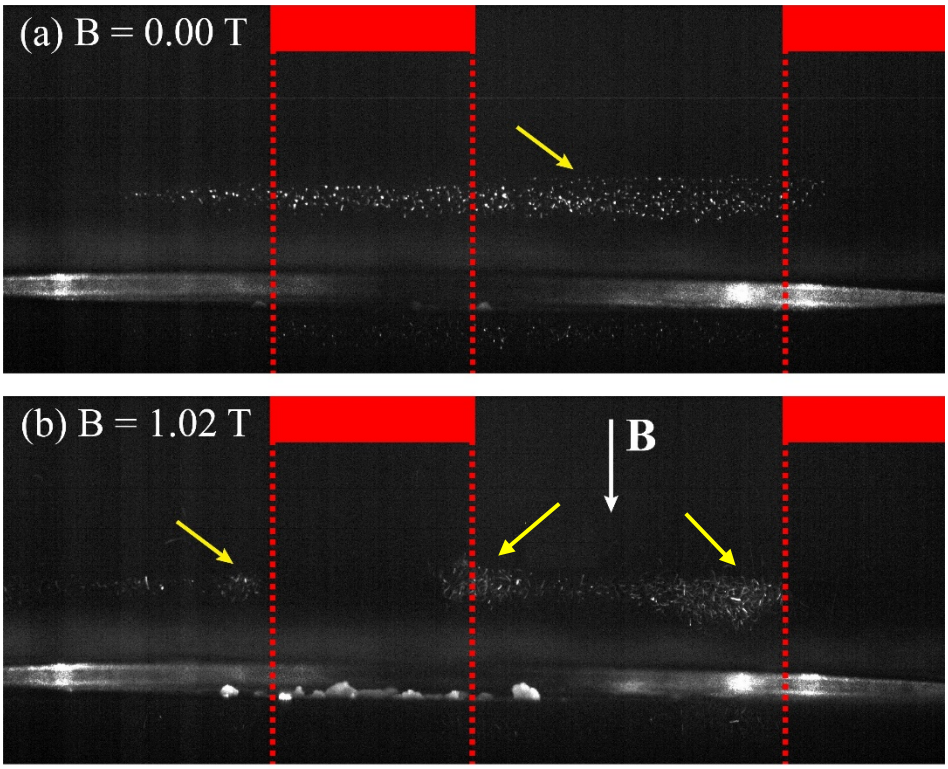

Figure 1.5: The position of dust particles beneath the electrode with and without applied magnetic field for a neutral pressure of *3.3 Pa* and "waffle" electrode bias of *+40 V*. The positions of the wires of the "waffle" electrode are indicated red rectangles. The yellow arrows point to the dust particles. At *B = 0* the dust particles are randomly distributed beneath the "waffle" electrode and do not get affected by it while at *B = 1.02 T*, the dust particles are mostly trapped beneath the edges of the "waffle" electrode wires [3].

to consider whether these phenomena arise from the same underlying physical mechanism. This work will show that these two phenomena arise due to the effects of strong magnetic field on the cross-field diffusion of electrons/ions and the presence of the metal mesh creates the gridding phenomenon by imposing filamentation in the magnetized dusty plasmas.

Study of these phenomena is relatively new and there have been few theoretical or numerical investigations on either the gridding [89] or on filamentation [1] [2] [90]. The biggest challenge in the experimental investigation of these phenomena is that, these highly magnetized plasmas are poorly diagnosed. The measurements of the properties of low-temperature plasmas such as plasma density and temperature are normally done using local probe measurements. Measurements from theses regular probes are significantly distorted in the presence of magnetic field and there exists very limited theoretical guidance for interpreting probe measurements at high magnetic field. Furthermore, the use of optical diagnostics approaches such as emission spectroscopy or laser induced fluorescence are also severely limited under the typical operating conditions where these studies are performed. Consequently, in order to investigate these rather new phenomena in these highly magnetized electric discharges, theoretical and numerical studies are crucial.

To study the underlying physics behind filamentation and gridding phenomena, a 3-dimensional (3D) fluid model is developed. In this 3D model, the plasma fluid equations are solved along with the Poisson's equation. Also, because of the need to run the model to resolve both electron and ion fluids at realistic mass ratios, the model is GPU accelerated using NVIDIA CUDA [91].

The simulation model will be used to explore a wide range of experimental configurations to attempt to reveal the key physical processes that are driving the filamentation/gridding

processes. Trying to simulate the detailed geometry and arrangements of the experiments would create unnecessary complications. For example, the cylindrical geometry of the plasma chamber and the details of the power deposition configuration in the experiments are not believed to be playing a critical role in determining the formation of the filaments. Therefore, a 3D rectangular grid is used to model a plasma chamber in these simulations. For cases that overlap with experimental conditions, qualitative comparisons will be made with experimental data. However, the ultimate goal here is to gain understanding of the physics of the filamentation and gridding and to use that insight to guide the next generation of experimental and computational research on this topic.

Using results from numerical simulations, the origins of plasma filamentation and dust particles gridding in low-pressure/low-temperature magnetized electric discharges are discussed. Although the motivation of this work is in the use of magnetized CCPs in the study of dusty plasmas, cross-magnetic field transport is also an important phenomenon in many applications of low temperature plasmas, such as magnetrons [92] and Hall effect thrusters [93]. Discovering the underlying physics would allow to derive an analytical description and potentially give an insight into pattern formation and self-organization for other environments which are governed by a similar set of equations such as those based on anisotropic heat transfer.

The following chapters of this dissertation are presented as follows. In Chapter 2, there will be a discussion on the numerical model and the simulation algorithm. In Chapter 3, the simulation results for filamentation and gridding phenomena will be presented, and the results will be discussed. Finally, Chapter 4 will present a summary of the work and present a brief discussion of new insights for future experiments that could be performed based on these numerical studies.

2 Numerical Model

The experimental observations of filamentation in low-pressure and low-temperature discharges would benefit from computational modeling to aid in interpreting the experiments and determining the origin of the filaments. As discussed in Chapter 1, there have only been a few limited attempts to model these strongly magnetized, low-temperature and low-pressure plasma systems. In this chapter, Sec. 2.1 will discuss some previous works that have used two-dimensional numerical models to understand the properties of filamentation. It is these works that motivated the development of the 3D fluid model that is the basis of this dissertation. Sec. 2.2 will introduce the two-fluid plasma equations and the required boundary conditions that form the physics basis for the numerical models. Sec. 2.3 will then present an assessment of the different numerical approaches that are considered in order to perform the calculations and the benefits/limitations of each one. Finally, Sec. 2.4 will discuss the algorithm and the implementation of the numerical model.

2.1 Previous 2D Studies of Pattern Formation in Magnetized Plasmas

There have been recent 2-dimensional (2D) simulations on filamentation phenomenon in low-pressure, low-temperature, magnetized plasmas [1] [90]. In reference [90], the formation of filamentary structures in a magnetized plasma is studied using a 2D kinetic model. In this model, neutral pressure is assumed to be very low (*0.01 Pa*) and the weak magnetic field (0.00*25-0.005 T*) is oblique to the electrodes. Although the article presents a very good discussion on dependency of the filamentary structures on electron's Larmor radius and Debye length, the orientation of magnetic field with respect to the electrodes and the magnitudes of pressure and magnetic field in this article, are not comparable to the experiments presented in the current work.

In reference [1], Menati et al. have investigated the dependency of the filamentary structures on the dielectric strength and secondary electron emission from the electrodes. In this article, the origins of plasma filaments in low pressure, argon CCPs are discussed using results from computational investigations performed on Hybrid Plasma Equipment Model (HPEM) [94] [95]. The goal of this 2D simulation was to offer new insights for a particular experimental configuration that could lead to the formation of filaments and to motivate continued experimental studies. The article indicates that the filaments are quasi-stationary structures that originate from statistical variations in the local plasma potential and charging of surfaces. Consistent with the experimental observations by Schwabe et al., [24], the filaments dissipate as magnetization parameter, $\chi = \frac{\lambda_{mfp}}{\rho_{ion}} = \frac{ion\ mean\ free\ path}{ion\ gyroradius} \sim \frac{B}{N}$ (*i.e.*, strength of magnetic field/gas number density) decreases. In the HPEM simulations, the onset of filaments occurs at B = 0.01 – 0.05 T for gas pressure of 5.3 Pa. For B = 0.1 T, the filaments begin to dissipate in the simulations for pressures exceeding 33.3-40 Pa.

The configuration of the CCP investigated in the HPEM simulations is a metal powered electrode and a grounded metal electrode placed behind a dielectric window. In these simulations, the strongest correlation of filaments with operating conditions is the surface conductivity of the dielectric window. Despite the interesting results, the simulations using HPEM fail to reproduce some important aspects of the experiments. For instance, in these simulations, filaments do not form if the grounded electrode opposite the powered electrode is directly exposed to the plasma or if the dielectric has significant surface conductivity. A sample of the electron density profile from HPEM as a function of electrode conductivity is given in figure 2.1. It can be seen in this figure that, by increasing the conductivity of the window covering the lower electrode (which is considered to be a dielectric by default), the filaments begin to dissipate in the configuration.

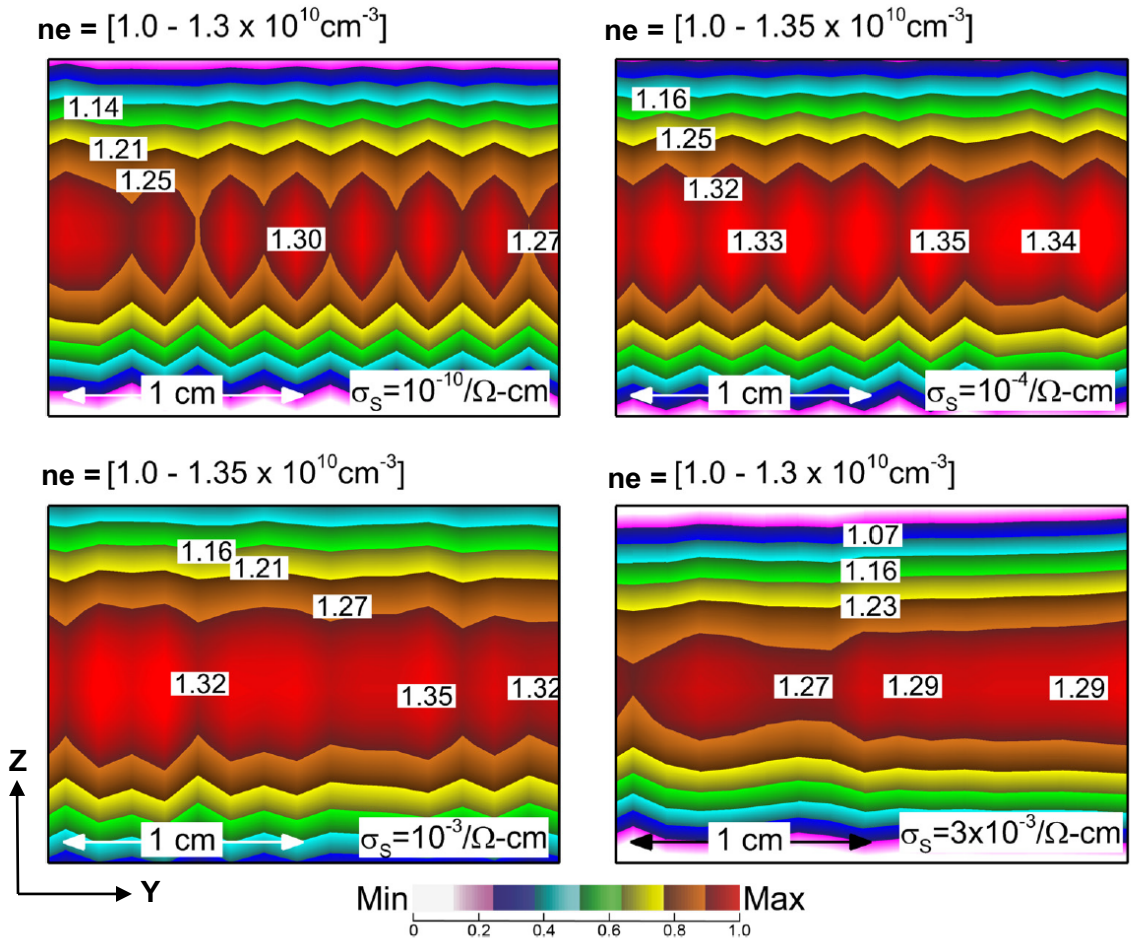

Figure 2.1: Y-Z Electron density profile at the center of a plasma chamber for B_z = 0.35 T as a function of the lower electrode conductivity obtained from HPEM. The top electrode is fully metallic. The default conductivity of the dielectric is $10^{-10}\Omega^{-1}$cm. Increasing the electrode conductivity to $10^{-4}\Omega^{-1}$cm, has little effect on the filaments. As conductivity is increased to $10^{-3}\Omega^{-1}$cm and higher, the filaments begin to dissipate. Contour labels are multipliers of 10^{10} cm^{-3} and give electron density at different locations in the chamber [1].

Also, due to the fact that HPEM is a 2D model, it does not reveal the differences between different filamentary patterns such as individual columns, spiral and target like structures by only providing a side view of these patterns. HPEM is mainly developed to duplicate real plasma sources employed in microelectronics and semiconductor industry. In the model, setting the neutral gas pressure and input power will automatically give rise to other plasma parameters such as electron/ion temperature, ionization fraction, and electron/ion densities. Despite practical applications of this aspect of HPEM, it does not allow for independently controlling individual plasma parameters which is crucial for studying the physics of filamentation phenomenon as will be discussed later. Therefore, despite revealing some aspects of filamentation phenomenon, two previous models are not able to fully capture the underlying physics behind the phenomenon.

To determine the nature of the observed filamentation instability, a 3D fluid model was developed here at Auburn University. The numerical model is intended to cover the dynamics of the electrons and ions, subject to neutral collisions, and to understand how those dynamics could cause the formation of filamentary structures in the plasma. The model will show how a density perturbation, in form of a single column, aligned to the magnetic field direction, will result in a series of filamentary structures parallel to the magnetic field. This fluid model is also modified by adding a metal mesh in the bulk of the plasma to investigate the gridding phenomenon. It is shown through these sets of simulations that filamentation and gridding phenomena can be indeed explained through the same physical mechanism.

2.2 Assumptions and Base Set of Equations for the Numerical Model

The development of the 3D model was influenced by choosing the minimum set of plasma transport equations that would address the phenomena of filamentation and gridding while also being numerically efficient. It has to be mentioned here that, since the time scale of the

dynamics of the dust particles is much longer than that of the electrons and ions (see equation 2.1), developing a 3D model including the dust particles along with the electrons and ions is not practical at the moment. Therefore, only electrons, ions and neutral particles as the background gas are considered in the current 3D model and dust particles are not included. Such a complete model will be the subject of future studies.

$$\Delta t_{\text{Filamentation,Gridding}} \gg \frac{1}{\omega_{p\alpha}}, \frac{1}{\omega_{c\alpha}} \quad , \alpha = e, i \text{ (for electrons and ions)}, \tag{2.1}$$

in which $\Delta t_{\text{Filamentation,Gridding}}$ is dynamics time scale of the filaments, $\omega_{p\alpha}$ is plasma frequency, and $\omega_{c\alpha}$ is cyclotron frequency for species α.

In the 3D model, the electric potential φ is obtained from the solution of Poisson's equation:

$$\nabla^2 \varphi = \frac{\rho}{\varepsilon} \tag{2.2}$$

where ρ is the charge density given by e($n_i - n_e$), and ε is the electric permittivity that we have assumed to be constant throughout the plasmas. The dynamics of the plasma fluid elements of the individual species α (= e, i - for electrons and ions) are addressed by the fluid equation of motion:

$$q_\alpha n_\alpha (\boldsymbol{E} + \boldsymbol{V}_\alpha \times \boldsymbol{B}) - \boldsymbol{\nabla} P_\alpha - m_\alpha n_\alpha \upsilon_{\alpha-n} \boldsymbol{V}_\alpha = m_\alpha n_\alpha (\frac{\partial \boldsymbol{V}_\alpha}{\partial \boldsymbol{t}} + (\boldsymbol{V}_\alpha . \boldsymbol{\nabla}) \boldsymbol{V}_\alpha), \tag{2.3}$$

where, q_α is charge, n_α is density, E is electric field vector given by - $\boldsymbol{\nabla}\varphi$, $\boldsymbol{V}_\alpha$ is velocity vector, $\boldsymbol{B}$ is magnetic field vector, P_α is pressure, m_α is mass, and $\upsilon_{\alpha-n}$ is collision frequency with neutral atoms.

It is assumed that the background neutral gas is stationary and contributes to the plasma only through collisions with electrons and ions. We do not consider separate fluid equations for the neutrals and we have not included excited states of the gas in the model. Additionally, in order

to further simplify the model, the plasma is considered to be isothermal with no heat transfer, so we do not solve for electron/ion temperatures and assume that they are constant (typically $T_e = 2$ *eV* and $T_i = 0.025$ *eV*) [20] [96]-[98]. The plasma is sustained by a simple ionization model that will be discussed in detail later in this section.

Our experiments have shown that the dynamical timescale of the filamentary structures, once they are established, is of the order of seconds and thus much slower than the dynamics of electrons and ions. Therefore, for slow evolution of the phenomenon (steady state), by neglecting acceleration and the nonlinear term on the right-hand side of equation (2.3), we get:

$$q_\alpha n_\alpha (\boldsymbol{E} + \boldsymbol{V}_\alpha \times \boldsymbol{B}) - \boldsymbol{\nabla} P - m_\alpha n_\alpha \upsilon_{\alpha n} \boldsymbol{V}_\alpha = 0 \tag{2.4}$$

The flux of each species, ($\Gamma_{\boldsymbol{\alpha}}$), is given by:

$$\Gamma_{\boldsymbol{\alpha}} = n_\alpha \boldsymbol{V}_{\boldsymbol{\alpha}} , \tag{2.5}$$

The collision frequencies are calculated using:

$$\upsilon_{\alpha n} = n_g \sigma_\alpha V_{th}, \tag{2.6}$$

in which, n_g is the neutral gas density, σ_α is electron/ion collision cross-section with neutral atoms, and V_{th} is the electron/ion average thermal velocity. All Collision cross sections are obtained from recent resources [99]-[101] based on the assumed electron/ion temperatures in the simulations.

Finally, we solve the continuity equation that governs the relation between the fluxes of the electrons/ions and their local densities including the source and the loss terms:

$$\frac{\partial n_\alpha}{\partial t} + \nabla \cdot \Gamma_\alpha = \sigma_I - \sigma_L, \tag{2.7}$$

in which σ_I and σ_L are ionization and recombination rates, respectively.

Unlike equation (2.4), we keep the time derivative term in continuity equation to cover the slow dynamics of the plasma filamentation. Without the time derivative in equation (2.7) the whole model will be time independent and we cannot investigate the time evolution of the pattern formation in the plasma. This approach has been employed in many previous plasma simulations, as a validated approach to allow a system to evolve to a steady state as described in the following references [102]-[110]. Because our systems are weakly ionized with ionization fractions of the order 10^{-6} to 10^{-8}, electron-ion and electron-electron collisions can be neglected.

In solving equation (2.7), therefore, we assume that electron-ion recombination only takes place on the surfaces of the discharge *($\sigma_L = 0$* in the bulk of plasma), while ionization occurs only in the bulk of the plasma. That is, there is no secondary electron emission from the walls of the chamber. If the total number of electrons in the simulation is S_i, and the total number of the lost particles at the walls for a given time interval is assumed to be S_L, our ionization model reads:

$$\sigma_I = \gamma n_e(x, y, z) \tag{2.8}$$

$$\gamma = \frac{S_L}{S_I - S_L}, \tag{2.9}$$

With electrons and ions produced at the same rate proportional to the local electron density, the continuity equation in the bulk of the plasma becomes:

$$\frac{\partial n_\alpha}{\partial t} + \nabla \cdot \Gamma_\alpha = \gamma n_e(x, y, z) \tag{2.10}$$

The loss rate of the electrons to the walls is more than the ions due to their smaller mass and higher mobility. Therefore, in order to sustain the plasma in our simulation, we keep the overall number of electrons constant by replacing any losses of electrons to the walls through the proposed ionization model. For each ionization process, an electron/ion pair is added to the bulk of the plasma at the target temperatures (mostly $T_e = 2\ eV$ and $T_i = 0.025\ eV$). In this ionization model, the total number of the added ions in each cycle of the simulation are more than the number of ions lost at the walls, but this slight excess of ions will eventually diffuse towards the walls and steady state will be reached. To show that steady state will be achieved through this model, the total number of electrons and ions in the simulation as a function of time are depicted in figure 2.2.

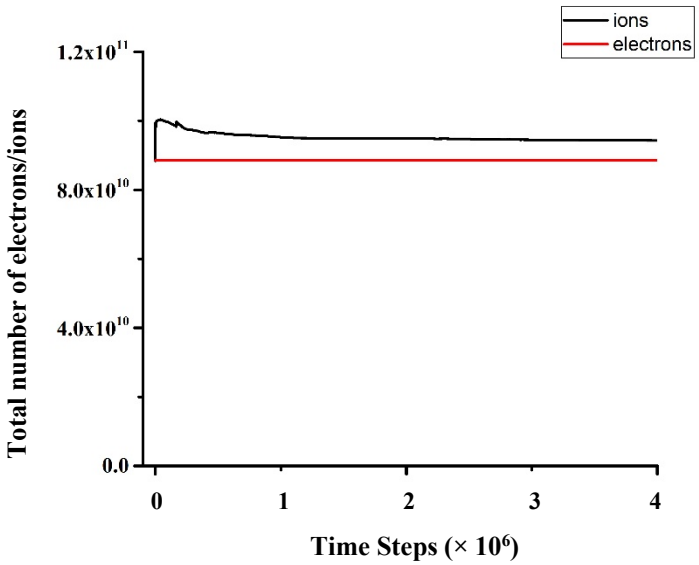

Figure 2.2: Total number of electrons (red line) and ions (black line) in the simulation over time.

2.3 Different Numerical Methods Employed in the 3D Model

In order to use the 3D model, appropriate numerical methods should be employed to discretize and numerically solve these equations. There are various methods for numerically solving the selected set of equations in our 3D model. In any model, the numerical methods are picked based on the efficiency to minimize the run time of the model and the required accuracy to minimize the error in the results obtained from the model in order to gain the expected spatial/temporal resolution in the solutions. The next few subsections briefly discuss different numerical methods utilized to build the 3D model. There are three main numerical methods used in the development of the code: (a) the finite difference method for evaluating the electric field vector and to discretize all partial derivative terms in the model equations, (b) the successive over relaxation method for solving Poisson's equation, and (c) the Runge-Kutta method for solving the continuity equation.

2.3.1 Finite Difference Method

Throughout Physics and other fields of science, partial derivatives appear frequently in the mathematical equations describing a variety of systems. Finding exact analytical solutions to these equations is rare and therefore numerical analysis of these equations through computer programing has become a crucial part of any scientific research. By that means, it is necessary to find a numerical form for partial derivatives that could be employed in computer programing. The most common way to discretize partial derivatives is using Finite Difference (FD) method.

For a given function $f(x)$, any mathematical equation in the form of $f(x+b) - f(x+a)$ is called a finite difference of function $f(x)$. In this context, three different forms of finite difference approximation of partial derivative of $f(x)$ at an arbitrary point can be defined:

Forward-Difference: $$f'(x) = \frac{\partial f}{\partial x} = \frac{f(x+\Delta x)-f(x)}{\Delta x}, \quad (2.11)$$

Backward-Difference: $$f'(x) = \frac{\partial f}{\partial x} = \frac{f(x)-f(x-\Delta x)}{\Delta x}, \quad (2.12)$$

Central-Difference: $$f'(x) = \frac{\partial f}{\partial x} = \frac{f(x+\Delta x)-f(x-\Delta x)}{2\Delta x}, \quad (2.13)$$

Here, the smaller the value of Δx is considered, the better the approximation of the partial derivative will be obtained. These three equations give numerical approximations of the slope of $f(x)$ at an arbitrary point. An example of these approximations for $x = x_0$ is displayed in figure 2.3.

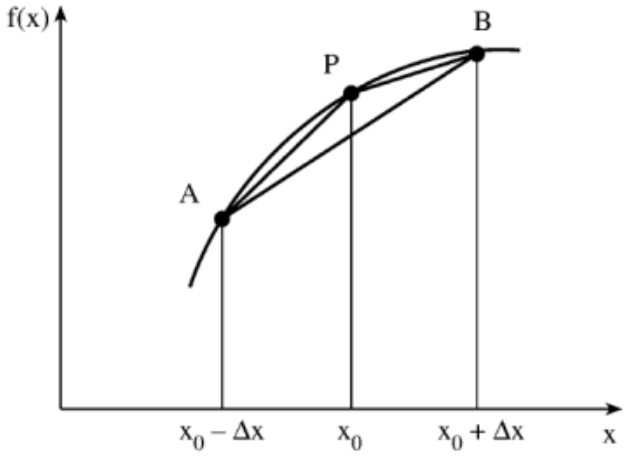

Figure 2.3: Finite difference approximations of the slope of *f(x)* at x_0 in which P-B is the forward-difference approximation, A-P is backward-difference approximation, and A-B is central-difference approximation.

By assuming $x = i\Delta x \equiv i$ for numerical applications on a computational grid, equations (2.11)-(2.13) can be rewritten as:

Forward-Difference: $$\frac{\partial f}{\partial x} = \frac{f(i+1)-f(i)}{\Delta x}, \tag{2.14}$$

Backward-Difference: $$\frac{\partial f}{\partial x} = \frac{f(i)-f(i-1)}{\Delta x}, \tag{2.15}$$

Central-Difference: $$\frac{\partial f}{\partial x} = \frac{f(i+1)-f(i-1)}{2\Delta x}, \tag{2.16}$$

in which $f(i+1) \equiv f(x+\Delta x)$, $f(i) \equiv f(x)$, and $f(i-1) \equiv f(x-\Delta x)$.

Although finite difference approximation of partial derivatives is explained here with respect to variable x, it can be applied in the same way for partial derivative with respect to time. In general the process will be the same for finite difference approximation of partial derivatives with respect to any of the variables x, y, z, or t in the function $f(x,y,z,t)$. In this case the function $f(x,y,z,t)$ can be expressed as:

$$f(x,y,z,t) \equiv f(i\Delta x, j\Delta y, k\Delta z, l\Delta t) \equiv f(i,j,k,l) \tag{2.17}$$

FD method is used to discretize any partial derivative in our equation set. In some equations such as calculating electric field vector from the plasma potential ($\boldsymbol{E} = -\nabla\varphi$), and solving momentum equation (equation 2.4), FD is sufficient to calculate the required variables. On the other hand, in solving Poisson's equation and continuity equation, FD is only used to discretize the equation so that more advanced methods can be applied to solve the equations.

2.3.2 Successive Over Relaxation (SOR) Method

Beyond the 1-D PDEs described in Sec. 2.3.1, a reliable method is required to solve more complex second order PDEs. The general form of second-order PDE's in 2D (X, Y) is given by [83]:

$$A\frac{\partial^2 f(x,y)}{\partial x^2} + 2B\frac{\partial^2 f(x,y)}{\partial x \partial y} + C\frac{\partial^2 f(x,y)}{\partial y^2} = D\frac{\partial f(x,y)}{\partial x} + E\frac{\partial f(x,y)}{\partial y} + Ff(x,y) + G, \quad (2.18)$$

in which A-G are coefficient of the PDE which can be a function of x, y or be constant and *f(x,y)* is a function of variables x and y. The goal of solving a PDE is to find *f(x,y)* for given boundary condition and initial value. In equation (2.18), by letting the coefficients to be positive, negative, or zero, different classes of PDE's such as hyperbolic ($B^2 - 4AC > 0$), elliptic ($B^2 - 4AC < 0$) or parabolic ($B^2 - 4AC = 0$) can be obtained [111]. One of the most famous forms of equation 1 is Poisson's equation which is obtained for A = C = 1, B = D = E = F = 0, and G to be a function of variables x and y:

$$\frac{\partial^2 f(x,y)}{\partial x^2} + \frac{\partial^2 f(x,y)}{\partial y^2} = G(x,y) \quad (2.19)$$

Poisson's equation appears in a variety of problems such as electrostatics, magnetostatics, diffusion, heat conduction, groundwater flow, pressurized membrane, and elastic torsion [112]. Similar to many other PDE's, when solving Poisson's equation, it is often very hard to find exact analytical solutions and therefore, numerical solutions must be employed. In order to numerically solve Poisson's equation, first the equation must be discretized using finite difference method.

Therefore, by using central finite difference approximation for the two terms on the left-hand side of equation (2.19) and ignoring the terms including Δx^2 or Δy^2, we get:

$$\frac{\partial^2 f(x,y)}{\partial x^2} = \frac{f(i+1,j)-2f(i,j)+f(i-1,j)}{\Delta x^2}, \tag{2.20}$$

$$\frac{\partial^2 f(x,y)}{\partial y^2} = \frac{f(i,j+1)-2f(i,j)+f(i,j-1)}{\Delta y^2}, \tag{2.21}$$

in which *(i,j)* represent $(i\Delta x, j\Delta y) \equiv (x,y)$. By substituting equations (2.20) and (2.21) in equation (2.19) and assuming $\Delta x = \Delta y = h$, we get:

$$f(i,j) = \frac{1}{4}\big(f(i+1,j) + f(i-1,j)f + f(i,j+1) + f(i,j-1) - h^2 G(i,j)\big), \tag{2.22}$$

which gives the value of function *f* at point *(i,j)* in terms of its values in the neighboring points as it is schematically drawn in figure 2.4.

Band matrix and iterative methods are two major ways to numerically solve equation (2.22). The band matrix method is usually used to solve limited number of equations (in our case the total number of grid points in the computational space). By contrast, iterative methods can handle large systems of simultaneous equations and therefore are more often used in numerical simulation of physical systems. In iterative methods, an initial estimate of the solution of f at *(i,j)* is assumed to obtain a second estimate of the solution using the governing PDE. In the same way, the next estimates of the PDE solution are calculated using the previous estimates until the solution reaches convergence. Also, there are three different iterative methods; Gauss-Seidle, Jacobi and Successive Over Relaxation (SOR) method. Among these three methods, SOR method converges

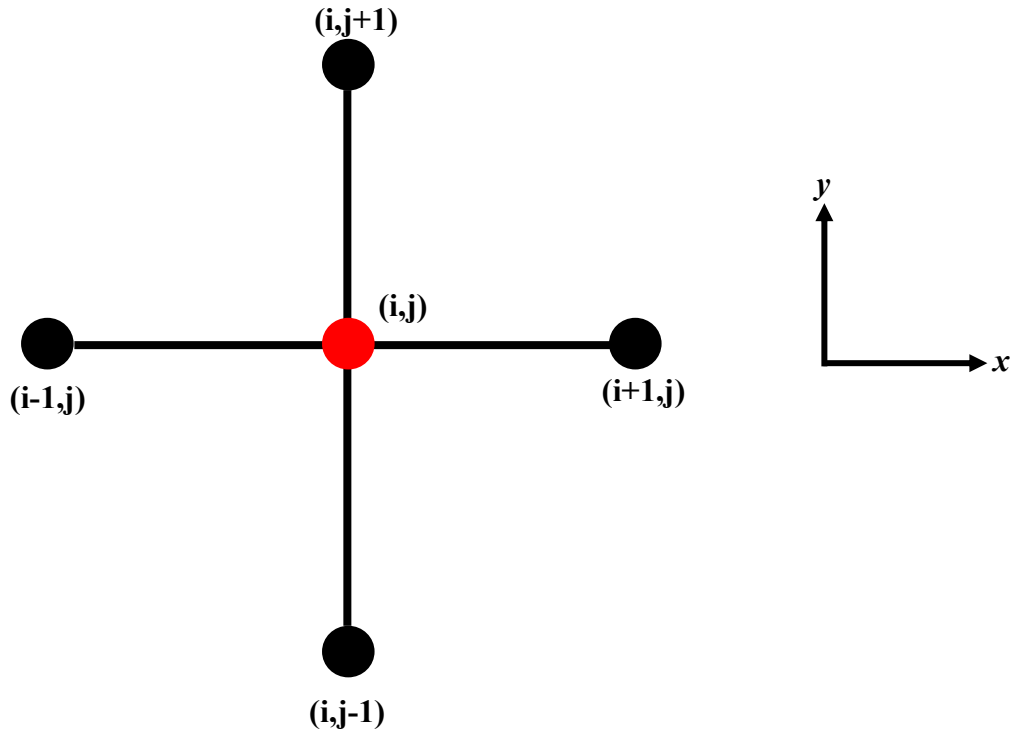

Figure 2.4: The relation between the value of function *f* at point *(i,j)* and its values in the neighboring points in *x* and *y* direction as described by equation 2.22.

faster than the other two and its implementation is also more straightforward so, it is used more frequently in numerical simulations.

To apply SOR method, the residual term *R(i,j)*, which is the amount by which the approximation of *f(i,j)* differs from the exact solution of equation (2.22), is defined at *(i,j)*:

$$R(i,j) = f(i+1,j) + f(i-1,j) + f(i,j+1) + f(i,j-1) - h^2 G(i,j) - 4\,f(i,j), \qquad (2.23)$$

R(i,j) can be also viewed as a correction that could be added to the estimate of *f(i,j)*, in order to improve it. By repeating this process, the initial approximation of *f(i,j)* gets closer step by step to its actual solution. Then, the SOR algorithm can be written as:

$$f^{k+1}(i,j) = f^{k}(i,j) + \frac{\omega}{4} R^{k}(i,j)\,, \qquad (2.24)$$

in which $f^{k+1}(i,j)$ is the *(k+1)th* approximation of *f(i,j)*, $f^{k}(i,j)$ is the (*k)th* approximation of *f(i,j)*, $R^{k}(i,j)$ is the *(k)th* approximation of the residual term defined by equation (2.23), and ω is called relaxation factor which has a value between 1 and 2 and is picked in a way to guarantee enhance the convergence of SOR method. ω only depends on the number of grid points and the number of dimensions in the computational space. For a 3D computational space with *m*, *n*, and *l* grid points in X, Y, and Z direction, ω is given by [113]:

$$\omega = \frac{2}{1+\sin\left[\cos^{-1}\left(\frac{1}{3}\left(\cos\frac{\pi}{m}+\cos\frac{\pi}{n}+\cos\frac{\pi}{l}\right)\right)\right]} \qquad (2.25)$$

2.3.3 Runge-Kutta Method

The most repeated differential equations in physics and other fields of science are the ones in the form of:

$$\frac{\partial y}{\partial x} = f(x, y) \tag{2.26}$$

This form of differential equations are specifically interesting because even the higher orders of this differential equation can still be represented in the form presented in equation (2.26). For instance, for a second order differential equation given as:

$$\frac{\partial^2 z}{\partial x^2} = g(x, z), \tag{2.27}$$

if a dummy function is defined as $y = \frac{\partial z}{\partial x}$, then equation (2.27) will be taking the exact form as equation (2.26). Therefore, the method of solving the first order differential equation can be also applied for solving higher order equations.

Several methods have been proposed to numerically solve equation (2.26). The most straightforward method is Euler's method. If we consider $\Delta x = h$ as the step size, Euler's method gives the finite difference approximation of equation (2.26) as:

$$\frac{y(n+1) - y(n)}{h} = f(x, y), \tag{2.28}$$

in which $y_{n+1} \equiv y(x_{n+1}) = y((n+1)h)$ and $y_n \equiv y(x_n) = y(nh)$. In Euler's method the right-hand side of equation (2.26) is evaluated using forward-finite-difference method. Equation (2.28) can be rearranged as:

$$y_{n+1} = y_n + hf(x, y) \tag{2.29}$$

Equation (2.29) is used to numerically find y_{n+1} (the value of function y at point $x_{n+1} = (n+1)h$) knowing y_n (the value of function y at point $x_n = nh$). It has to be mentioned again that the variable x can be any arbitrary variable. For instance, if the derivative in equation (2.26) is taken with respect to time, then the problem becomes solving an initial condition differential equation. In order to solve for y_{n+1} in equation (2.29), first the function $f(x,y)$; which is the slope of function $y(x)$, should be evaluated. Indeed, the question that needs to be answered is that "which set of (x,y) [(x_n, y_n) or (x_{n+1}, y_{n+1})] should be used to evaluate $f(x,y)$?"

If $f(x,y)$ is evaluated at point (x_n, y_n), the method is called Euler method:

$$k_1 = f(x_n, y_n) \tag{2.30}$$

$$y_{n+1} = y_n + k_1 \tag{2.31}$$

So, Euler method is assuming a linear relationship between y_{n+1} and y_n which of course is not always correct and therefore despite the easy procedure for the application of Euler method, the method is not very accurate and not very common. Assuming $y(x_n) = y_n$ (initial value problem), the Euler Method is schematically depicted in figure 2.5.

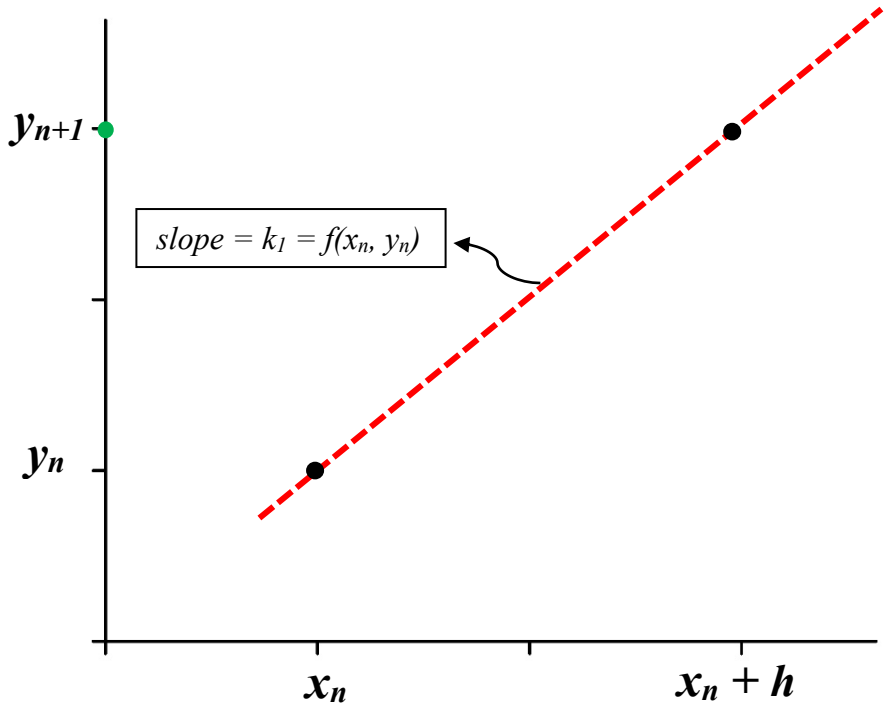

Figure 2.5: Schematic graph of Euler method to numerically find the value of y at x_{n+1} knowing its value at x_n.

Euler method has an accuracy of the order of (h) which is the selected step size for the numerical solution [111]. Among different methods that can numerically solve equation (2.26) with a high level of accuracy, Runge-Kutta method has been widely adopted. Different orders of Runge-Kutta method are defined based on multiple evaluations of function *f(x, y)* in equation (2.26) that can yield different levels of accuracy. Here, second order and fourth order Runge-Kutta method will be explained and the other orders of this method can be calculated through the same procedure. Second order Runge-Kutta method includes three steps. In step 1, function *f(x, y)* will be evaluated at the point (x_n, y_n) to give $k_1 = f(x_n, y_n)$. In step 2, function *f(x, y)* will be evaluated at the point $(x_n + \frac{h}{2}, y_n + k_1 \frac{h}{2})$ that yields $k_2 = f(x_n + \frac{h}{2}, y_n + k_1 \frac{h}{2})$. In step 3, k_2 is used in the final step to solve for $y(x_n+h)$ through the equation $y_{n+1} = y_n + k_2 h$. The steps in the second order Runge-Kutta method are:

Step 1: $$k_1 = f(x_n, y_n), \tag{2.32}$$

Step 2: $$k_2 = f(x_n + \frac{h}{2}, y_n + k_1 \frac{h}{2}), \tag{2.33}$$

Step 3: $$y_{n+1} = y_n + h\, k_2 \tag{2.34}$$

These steps are schematically depicted in figure 2.6. The accuracy of second order Runge-Kutta method is of the order of (h^2) [111]. In order to reach higher levels of accuracy, higher orders of Runge-Kutta method can be employed. Fourth order Runge-Kutta method is one of the most common forms of Runge-Kutta method that is easy to apply and provides an accuracy of the order of (h^4). In the fourth order Runge-Kutta method, five steps have to be taken to numerically calculate $y(x_n+h)$ knowing $y(x_n)$:

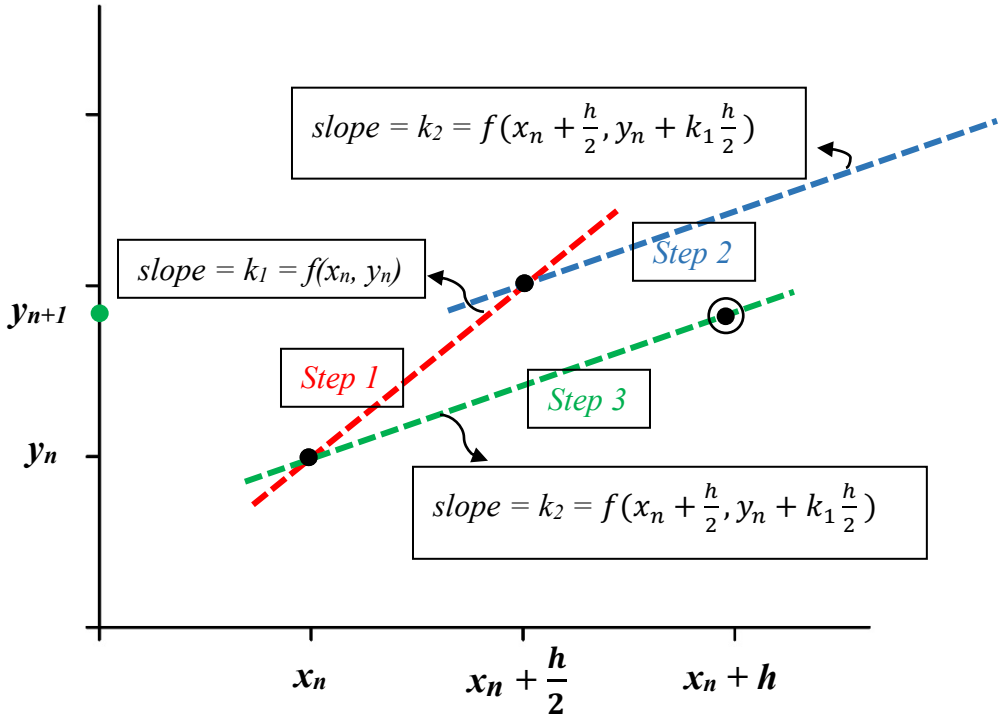

Figure 2.6: Schematic graph of second order Runge-Kutta method to numerically find the value of y at x_{n+1} knowing its value at x_n. In step 1, function $f(x, y)$ will be evaluated at the point (x_n, y_n) to give $k_1 = f(x_n, y_n)$. In step 2, function $f(x, y)$ will be evaluated at the point $(x_n + \frac{h}{2}, y_n + k_1\frac{h}{2})$ that yields $k_2 = f(x_n + \frac{h}{2}, y_n + k_1\frac{h}{2})$. In step 3, k_2 is used in the final step to solve for $y(x_n+h)$ through the equation $y_{n+1} = y_n + k_2 h$.

Step 1: $$k_1 = f(x_n, y_n), \quad (2.35)$$

Step 2: $$k_2 = f(x_n + \frac{h}{2}, y_n + k_1 \frac{h}{2}), \quad (2.36)$$

Step 3: $$k_3 = f(x_n + \frac{h}{2}, y_n + k_2 \frac{h}{2}), \quad (2.37)$$

Step 4: $$k_4 = f(x_n + h, y_n + k_3), \quad (2.38)$$

Step 5: $$y_{n+1} = y_n + \frac{h}{6}(k_1 + 2k_2 + 2k_3 + k_4) \quad (2.39)$$

So, in 4th order Runge-Kutta method, the function *f(x, y)* is evaluated at four different points (different sets of *(x, y)*) and in the final step the weighted average of these four different estimate of *f(x, y)* is used to numerically calculate $y(x_n+h)$. Now that $y(x_n+h)$ is evaluated through 4th order Runge-Kutta method, the same procedure should be repeated to evaluate $y(x_n+2h)$ and the next points after that.

In our 3D model, 4th order Runge-Kutta method is used to solve the continuity equation. The time evolution of the model is only implemented in this equation and therefore, an accurate and stable solution for it, is crucial.

2.4 Algorithm and Computational Space

In order to numerically solve the selected set of equations, the computational space must be discretized into mesh points at which the physical variables are going to be evaluated. The plasma source in our model is assumed to be rectangular and a 3D multi-mesh configuration is used to simulate plasma chamber with metal walls on all sides. As shown in figure 2.7, the electric potential and electron/ion densities are calculated on the main mesh points (black circles in figure

2.7), while electric field and electron/ion fluxes are derived at midpoints between two main mesh points in X, Y and Z direction.

The Successive Over-Relaxation (SOR) method [113] is employed to solve Poisson's equation with the boundary condition of zero potential at the metal walls. The electric field at the midpoints is then calculated from the potential which will be substituted into the momentum equation to evaluate the electron/ion fluxes at halfway between the main mesh points. A 4^{th} order Runge-Kutta method is used to evaluate continuity equation, equation (2.10), and update electron and ion densities on the grid. Once this step is completed, the simulation is advanced to the next time step. The overall simulation algorithm is illustrated in figure 2.8.

Typical electron density and temperature in the MDPX device at $B = 0$ are $4\text{-}10\times10^{14}\ m^{-3}$ and $2\text{-}4\ eV$ respectively. In the simulations, a uniform plasma at a background electron/ion density of $1\text{-}15\times10^{14}\ m^{-3}$ is considered with an applied, uniform magnetic field (0.8-2.0 T) in Z direction. The electron and ion temperatures are initialized at $1.5\text{-}3\ eV$ and $0.025\ eV$ respectively and are assumed to be constant. The volume of the simulated plasma is $6.3\ cm\times6.3\ cm\times4.2\ cm$.

It was noted in the experiments and other simulations that, electron Debye length and ion mean-free-path play a role in the filamentation and gridding phenomena [24] [90]. Therefore, in various simulations, the grid size in X/Y direction (perpendicular to the magnetic field) is assumed to be $h_x = 3.5\times10^{-4}\ m$ or 2×10^{-4} to be smaller than these two characteristic lengths. In Z direction (parallel to the magnetic field) on the other hand, the grid size is considered to be $h_z = 6\times10^{-4}\ m$. Since the fluxes and the dynamic of the charged species parallel to the magnetic field will not be affected by the magnetic field, the mesh spacing in this direction is considered larger than the spacing perpendicular to the magnetic field. This is computationally beneficial, resulting in a reduction of the total number of grid points.

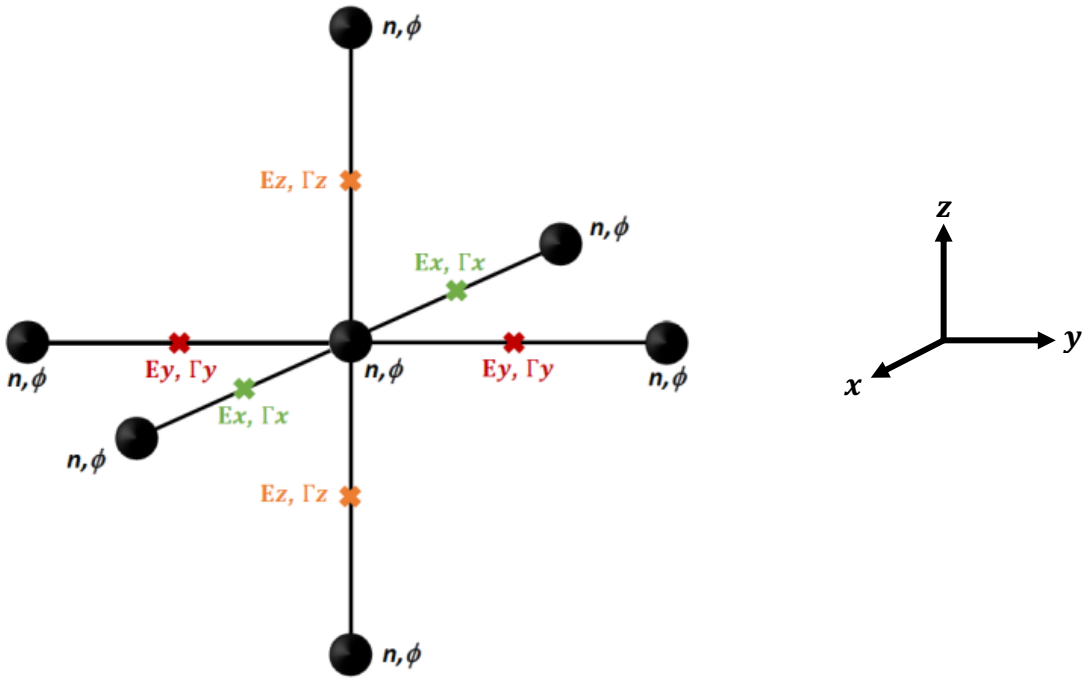

Figure 2.7: The multi-mesh computational grid. The electric potential and electron/ion densities are calculated on the main grid points (black circles) while the electric field and electron/ion fluxes are obtained at the corresponding midpoints.

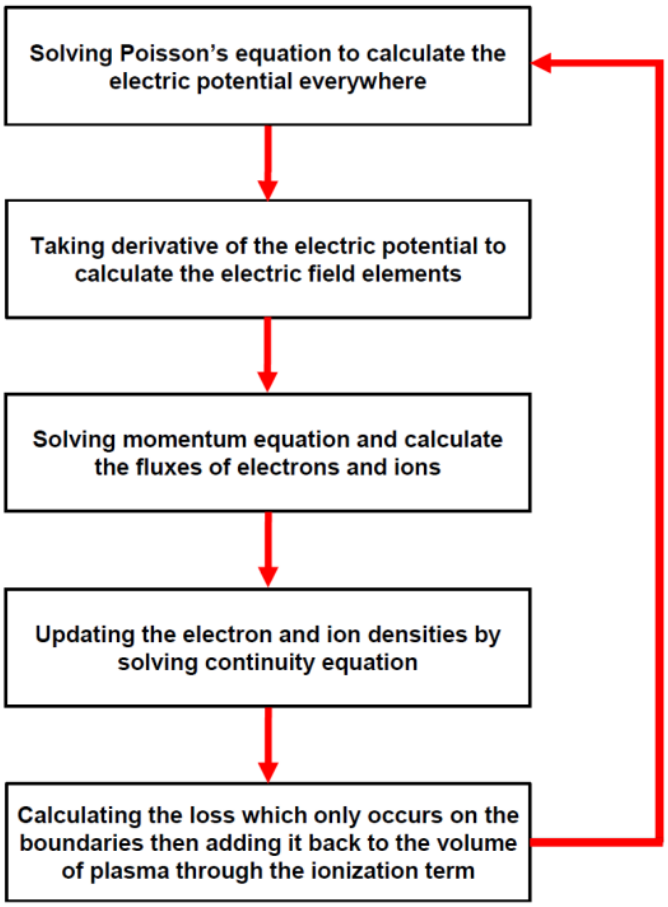

Figure 2.8: The simulation algorithm

Since our simulation is explicit, in order to avoid numerical instabilities, a simulation time step of $10^{-11}\ s$ is used in most of the simulations to ensure that the time step is not larger than the dielectric relaxation time of the plasma [114]:

$$\Delta t_d = \frac{\varepsilon_0}{\sigma} \tag{40}$$

where σ is the plasma conductivity.

The time step in the simulation is very small and the dynamic of the filaments in the filamentation experiments occur at timescales of the order of milliseconds to seconds. As a result, it is not currently feasible to simulate the dynamic of the filaments in the chamber with respect to each other. Also, the equations are solved using a graphics processing unit (GPU) parallel code using NVIDIA CUDA [91] to accelerate the simulation. Table 2.1 presents typical length and time scales for the plasma parameters mentioned above.

$\Delta x = 3.5\times10^{-4}\ m$	$\lambda_{De} \approx 5.0\times10^{-4}\ m$	$r_{Li} \approx 2.5\times10^{-4}\ m$	$\lambda_i \approx 7\times10^{-4}\ m$	$L_x \approx 6\ cm$
$\Delta t = 1\times10^{-11}\ s$	$\frac{1}{\omega_{pe}} \approx 9.0\times10^{-10}\ s$	$\frac{1}{\omega_{ci}} \approx 2.0\times10^{-7}\ s$	$\frac{1}{\upsilon_i} \approx 1.5\times10^{-6} s$	$t_f \approx 1ms–1s$

Table 2.2: Typical length and time scale in the simulation for a plasma density of 5×10^{14}, electron temperature of *2.5 eV*, room temperature ion, neutral gas pressure of *10 Pa*, and *1.0 T* magnetic field. In this table Δx is step size in *X* and *Y* direction, λ_{De} is electron Debye length, r_{Li} is ion Larmor radius, λ_i is ion mean-free-path, L_x is the length of the plasma chamber in X and Y direction, Δt is time step, ω_{pe} is electron plasma frequency, ω_{ci} is ion gyro-frequency, υ_i is ion collision frequency and t_f is typical time scale for the motion of filaments with respect to each other in the experiments.

Simulations are performed by varying pressure, plasma density (power), electron temperature, gas type, and the height of the plasma chamber to independently discover the effect of these parameters on filamentation and gridding phenomena. For the simulations of gridding phenomenon, an additional variable of the width of the mesh wires is also considered. In all of these cases, filamentary structures form in the plasma in the *X*-*Y* plane transverse to the magnetic field, while along the magnetic field (*Z* direction), the density behaves like a one-dimensional plasma. Consequently, we mostly look at the pattern formation as seen from the top (*X*-*Y* plane cross-section) and the simulations are stopped at about $t = 20\text{-}40\ \mu s$ ($2\text{-}4\times10^{6}$ time steps of simulation) at which the patterns are stablished. About this time scale, the filamentary structures are fully formed in the simulation and their shapes do not significantly change.

After defining the mesh configuration and the simulation algorithm as the last steps, everything is set in model and it can be run. In the first simulations, filamentation and gridding phenomena should be generated and then their physics could be explored by repeating the simulation using different plasma parameters. It is noted that, although, the simulations presented here are inspired by the experimental observations of filamentation and gridding phenomena, the simulations are not exactly duplicating any experimental set up. For instance, in the most filamentation and gridding experiments a circular ring was placed on the lower electrode for the confinement of the plasma but, a rectangular plasma chamber is assumed in the numerical simulations of these phenomena. The rectangular configuration was picked because it was noticed in the experiments that the shape of the plasma chamber was not an important factor in the formation of filamentary patterns and also solving a set of differential equations in cylindrical coordinate system would require difficult computational implementation.

3 Filamentation of Magnetized Plasmas

It is believed that filamentary patterns imposed by a metal mesh placed in the bulk of a strongly magnetized plasma are responsible for gridding phenomenon. Therefore, studying filamentation phenomenon is not only important for understanding the behavior of strongly magnetized plasmas but also to accurately explain the gridding phenomenon. This chapter starts with presenting benchmarking simulations for filamentation phenomenon in section 3.1. In section 3.2, the simulation results for filamentation under variation of different plasma parameters will be presented and discussed in section 3.3.

3.1 Benchmarking Simulations

Before trying to simulate filamentation phenomenon, it would be useful to evaluate the performance of the model in the simulation of a uniform unmagnetized plasma. Therefore, a rectangular plasma chamber with grounded metal walls is considered, which is displayed in figure 3.1. The chamber contains uniform argon plasma ($n_e = n_i = 5.4 \times 10^{14}\, m^{-3}$) with constant electron and ion temperatures of $T_e = 2.5\, eV$ and $T_i = 0.025\, eV$, respectively. Figure 3.2 displays a horizontal (X-Y) cross section of the electron density and plasma potential profile from the simulation of the unmagnetized plasma. Although different in magnitude, the shape of ion density profile is similar to that of the electrons and is not shown here. The simulation is terminated at $t = 40\, \mu s$ and the cross-section profiles are taken from the middle of the plasma chamber at $Z = 2.1\, cm$. It can be seen in these figures that, in the absence of a perturbation and magnetic field, electrons/ions simply diffuse to the walls of the plasma chamber and recombine there. Due to the much higher mobility

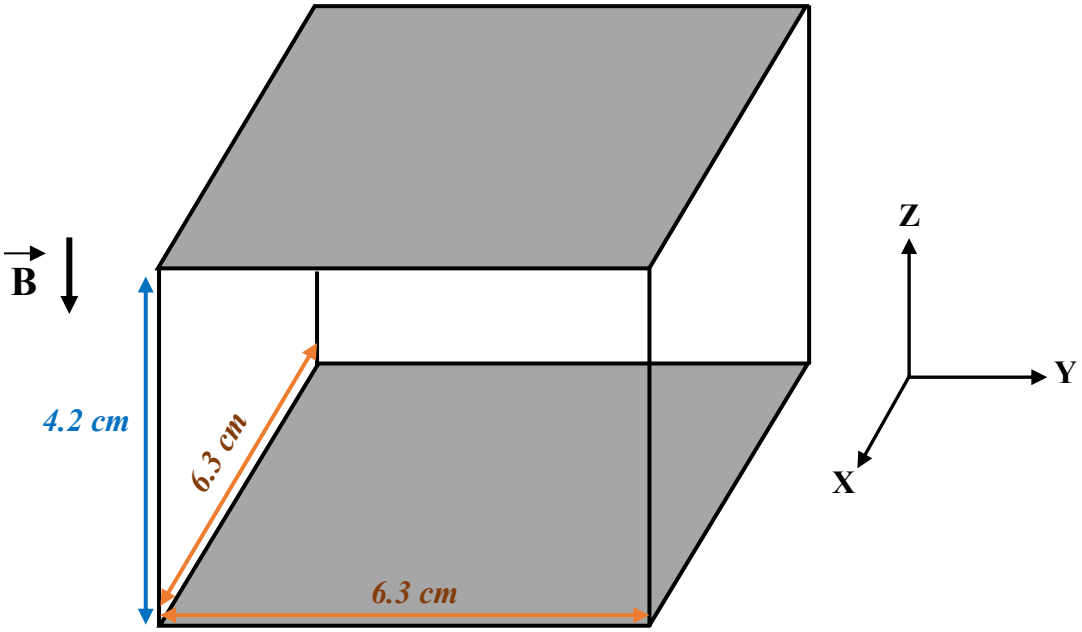

Figure 3.1: Schematic drawing of the rectangular plasma chamber with grounded metal walls, considered in the simulation of filamentation phenomenon.

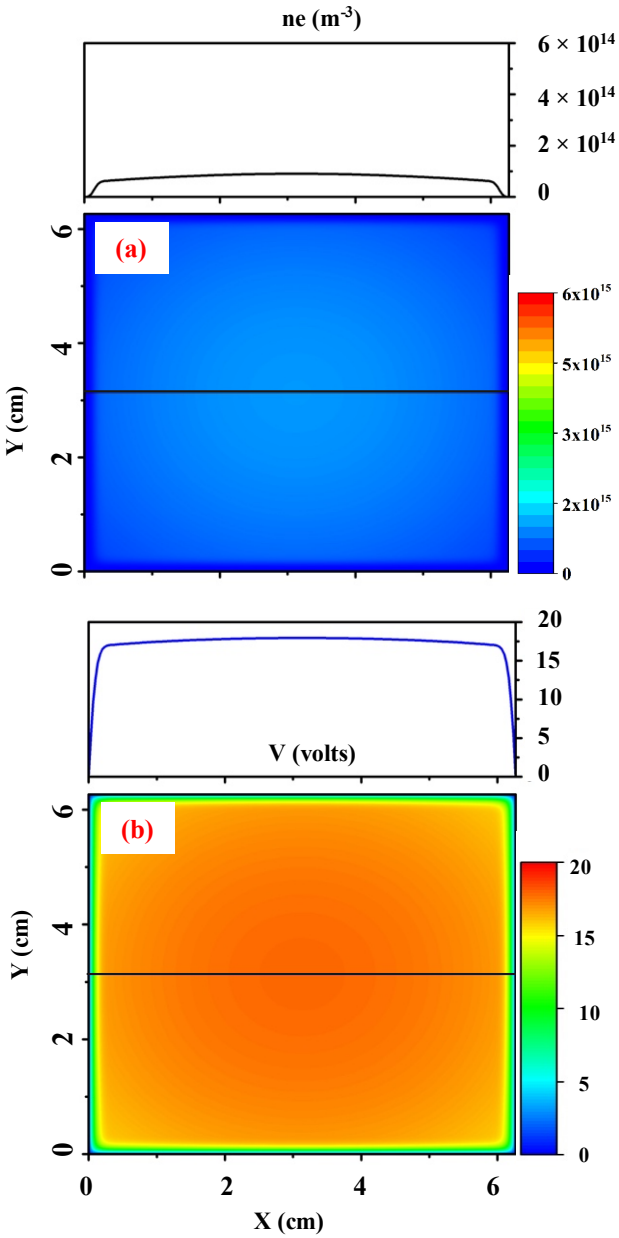

Figure 3.2: X-Y cross section of the electrons density (a) and plasma potential (b) profile from the simulation of the unmagnetized plasma. The solid black line indicates where the top plots have been taken from. The background plasma density is $5.4\times10^{14}\ m^{-3}$, the neutral pressure is 9 Pa, and the electron and ion temperature are $T_e = 2.5\ eV$ and $T_i = 0.025\ eV$. In the absence of magnetic field and perturbation, the plasma simply diffuses to the walls without generating any significant phenomenon. The formation of plasma sheath is clearly seen near the walls.

of the electrons, the loss of the electrons is more than the ions and the plasma is electropositive. It is seen in these figures that sheath regions have formed self-consistently near the walls.

In the second benchmarking simulation, a magnetic field of $B = 0.8\ T$ is applied to the plasma in negative Z direction. Since no perturbation is added to break the homogeneity of the magnetized plasma, the electrons and ions diffuse to the walls of the plasma chamber mostly parallel to the magnetic field. Figure 3.3 displays the X-Y cross section of electron density and plasma potential profile at the midplane of this undisturbed magnetized plasma at $t = 40\ \mu s$. Even in presence of magnetic field filamentary patterns are not forming in the uniform plasma and the only significant phenomenon is what seems to be the excitation of Kelvin-Helmholtz instability in the sheath regions of the plasma. The excitation of Kelvin-Helmholtz instability is due to the rotation of the plasma ($\boldsymbol{E} \times \boldsymbol{B}$ drift of the electrons and ions) against the walls. The plasma is again electro-positive, but because of the lower rate of plasma loss to the walls in the magnetized plasma, the plasma potential is smaller compared to the unmagnetized plasma (see figure 3.2(b)).

To trigger the formation of filamentary patterns, some form of perturbation must be introduced to the magnetized plasma to break the symmetry of the model. Therefore, we chose to introduce a high-density plasma column along Z direction (parallel to the magnetic field) to break the initial homogeneity of the background plasma. The introduced perturbation to the plasma has a density 10 times the background plasma, a diameter of about $2\ mm$, and is extended from the top to the bottom electrode, as it is depicted in figure 3.4 for $t = 0\ s$. Although the perturbation is considered to be 10 times the background plasma density, a smaller perturbation would result in the same pattern configuration but the smaller the initial perturbation, the longer it takes for the patterns to appear in the plasma.

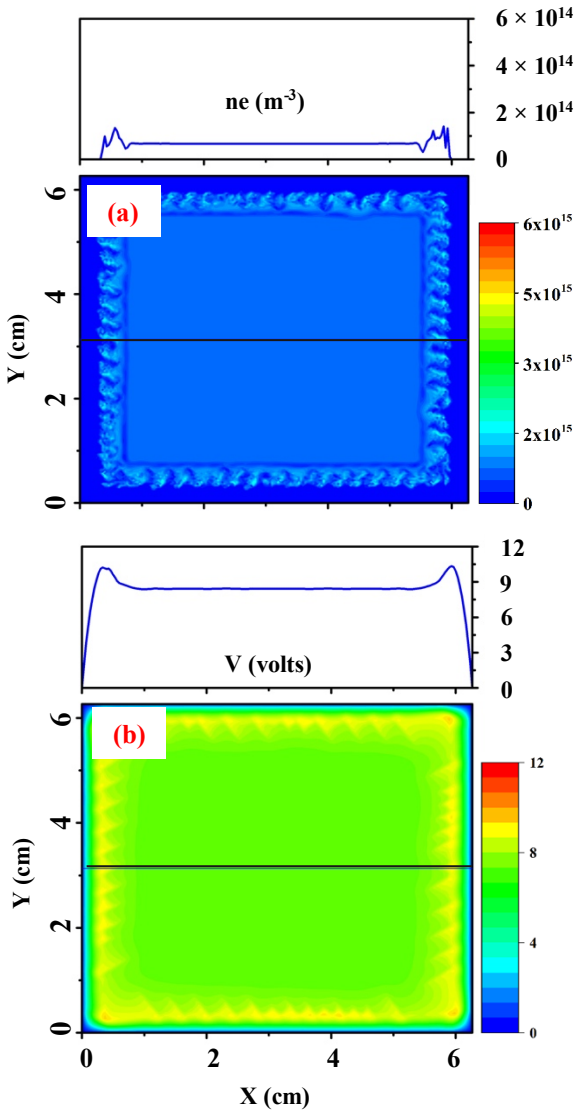

Figure 3.3: X-Y cross section of electron density and plasma potential profile in the middle of the undisturbed magnetized plasma at *t = 40 μs.* The only significant phenomenon in this plasma is the excitation of Kelvin-Helmholtz instability in the sheath region of the plasma due to rotation of the plasma against the walls under the effect of magnetic field. *B = 0.8 T* is applied to the plasma, the background plasma density is *5.4×10^{14} m^{-3}*, the neutral pressure is 9 Pa, and the electron and ion temperature are *$T_e = 2.5$ eV* and *$T_i = 0.025$ eV.*

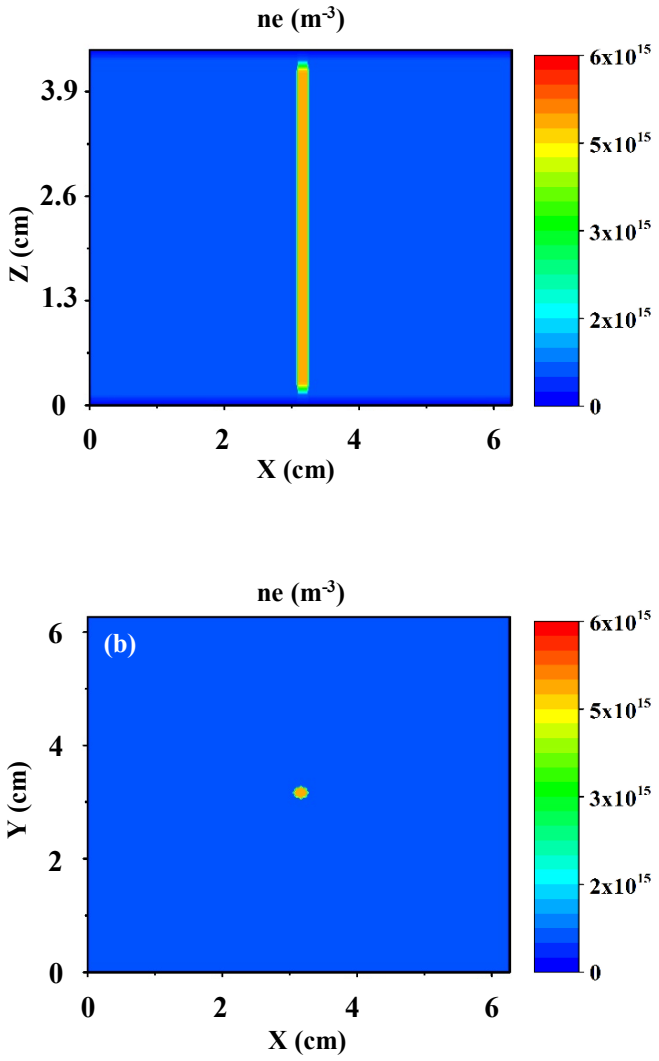

Figure 3.4: Cross section of initial electron density at *t = 0 s* with a high density column introduced to break the homogeneity of the plasma. a) side view (*Y = 3.2 cm*), b) top view (*Z = 2.1 cm*).

By introducing the perturbation to the background uniform plasma, the filamentary patterns emerge in the magnetized plasma. The same filamentary patterns appear in the electron/ion density as well as in the plasma potential which can be seen in the example presented in figure 3.5. The X-Y cross-section profiles presented in this figure are taken from the middle of the plasma chamber at $Z = 2.1\ cm$, and the X-Z cross section profile is taken at $Y = 3.2\ cm$. In all other simulations, the X-Y and X-Z cross section profiles are taken at the same points. In figure 3.5, the background plasma density is $5.0\times10^{14}\ m^{-3}$, neutral gas pressure is $9\ Pa$, the applied magnetic field is $0.8\ T$, electron temperature is $T_e = 2.5\ ev$, and ion temperature is $T_i = 0.025\ ev$.

Each graph in figure 3.5 is labeled with a set of three length parameters; ($r_i\ (mm)$, $\lambda_i\ (mm)$, $\lambda_{De}\ (mm)$), which represent ion gyro-radius, ion-neutral mean-free-path, and electrons Debye length, respectively. In an unmagnetized plasma, these parameters are calculated through the following equations:

$$r_i = \frac{m_i V_{th_i}}{qB} \tag{3.1}$$

$$\lambda_i = \frac{V_{th_i}}{\upsilon_i} \tag{3.2}$$

$$\lambda_{De} = \sqrt{\frac{\varepsilon_0 K_b T_e}{e^2 n_e}} \tag{3.3}$$

in which m_i is the mass of the ions, V_{th_i} is thermal velocity of the ions, q is the charge of the ions, B is the magnetic field, υ_i is ion-neutral collision frequency, ε_0 is electric permittivity of free space, K_b is the Boltzmann constant, T_e is electron temperature, e is the unit charge, and n_e is the

background electron density.

Similar to figure 3.3, instabilities appear in the sheath regions of figure 3.5. The instabilities can be seen in both electrons and ions X-Y density profiles. These also seem to be again Kelvin-Helmholtz instabilities due to the $\boldsymbol{E} \times \boldsymbol{B}$ drift of the electrons and ions, moving in the same direction (counter-clockwise) in both profiles. It is noted that $\boldsymbol{E} \times \boldsymbol{B}$ drift is independent of the electric charge and is the same for electrons and ions. Also, from 3.5.d, it is clear that the filamentary patterns are extended in the bulk of the plasma parallel to the applied magnetic field. Another feature of figure 3.5 is that, the shape of the filamentary patterns in X-Y cross section profile of the electron density, ion density, and plasma potential are the same and the patterns are uniformly extended in the bulk of the plasma in Z direction. Because of this similarity, the rest of this work will primarily present just the X-Y electron density plots.

In order to numerically compare the filamentation properties of the plots of plasma simulations under different conditions, we define a dimensionless filamentation parameter "*F*" as below:

$$F = \frac{d_s}{w_f} n_f \tag{3.4}$$

in which, d_s is the distance from the first filamentary ring to the sheath edge perpendicular to the magnetic field, w_f is the average width of the filamentary rings, and n_f is the total number of the filamentary rings in the plasma as viewed from the top. These parameters are indicated on the electron density profile example featured in figure 3.6. The higher the filamentation parameter is in an specific graph, the higher the number of filamentary rings in the graph and the narrower those filamentary rings are.

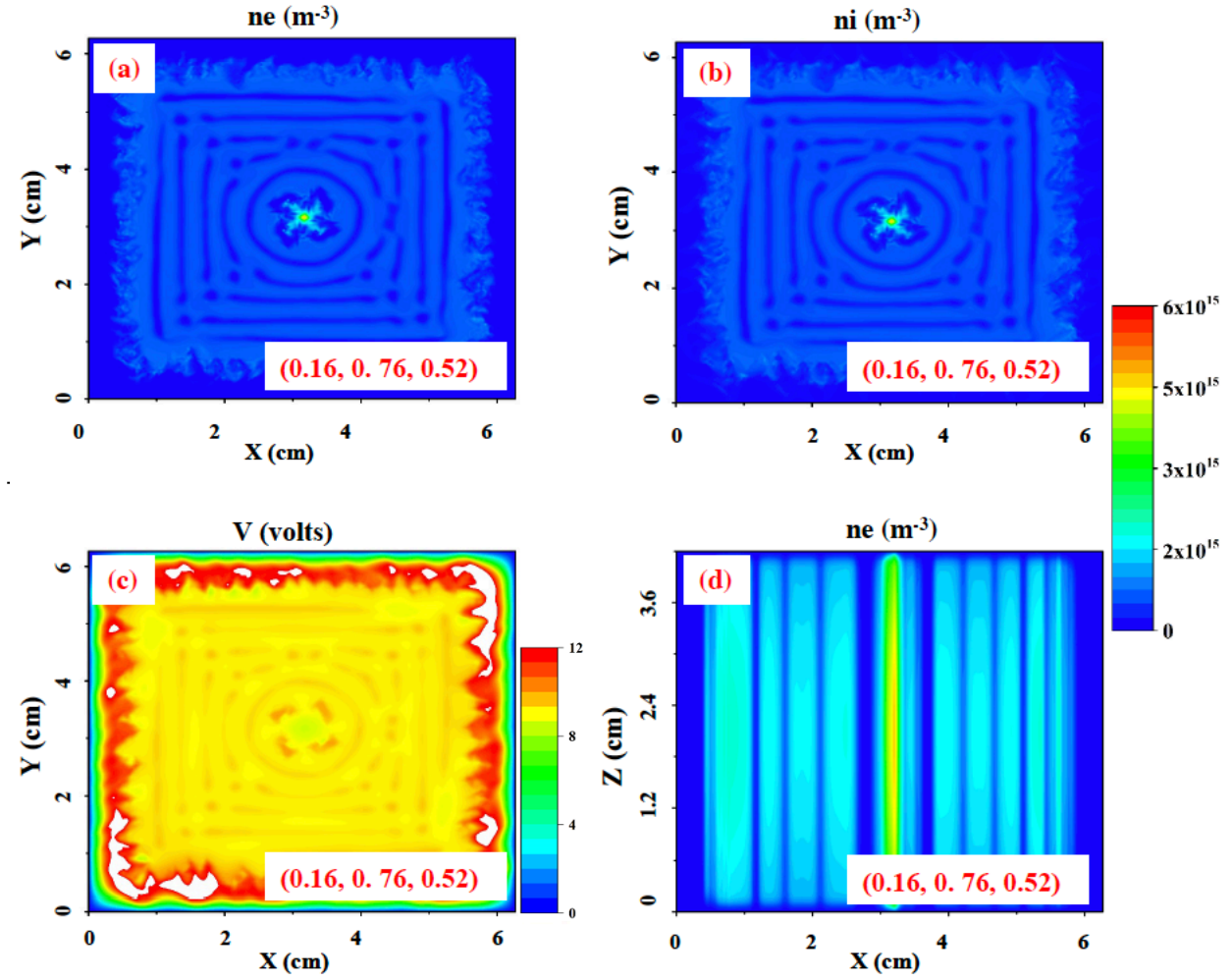

Figure 3.5: Top view of an example of filamentary pattern formation in: a) electron density, b) ion density, and c) plasma potential. The side view of electron density profile is given in (d). The X-Y cross-section profiles presented in this figure are taken from the middle of the plasma chamber at $Z = 2.1\ cm$, and the X-Z cross section profile is taken at $Y = 3.2\ cm$. The background plasma density is $5.0\times10^{15}\ m^{-3}$, neutral gas pressure is $9\ Pa$, the applied magnetic field is $1.0\ T$, electron temperature is $T_e = 2.5\ eV$, and ion temperature is $T_i = 0.025\ eV$. Each graph is labeled with a set of three length values; ($r_i\ (mm)$, $\lambda_i\ (mm)$, $\lambda_{De}\ (mm)$), which represent ion gyro-radius, ion-neutral mean-free-path and electron Debye length respectively.

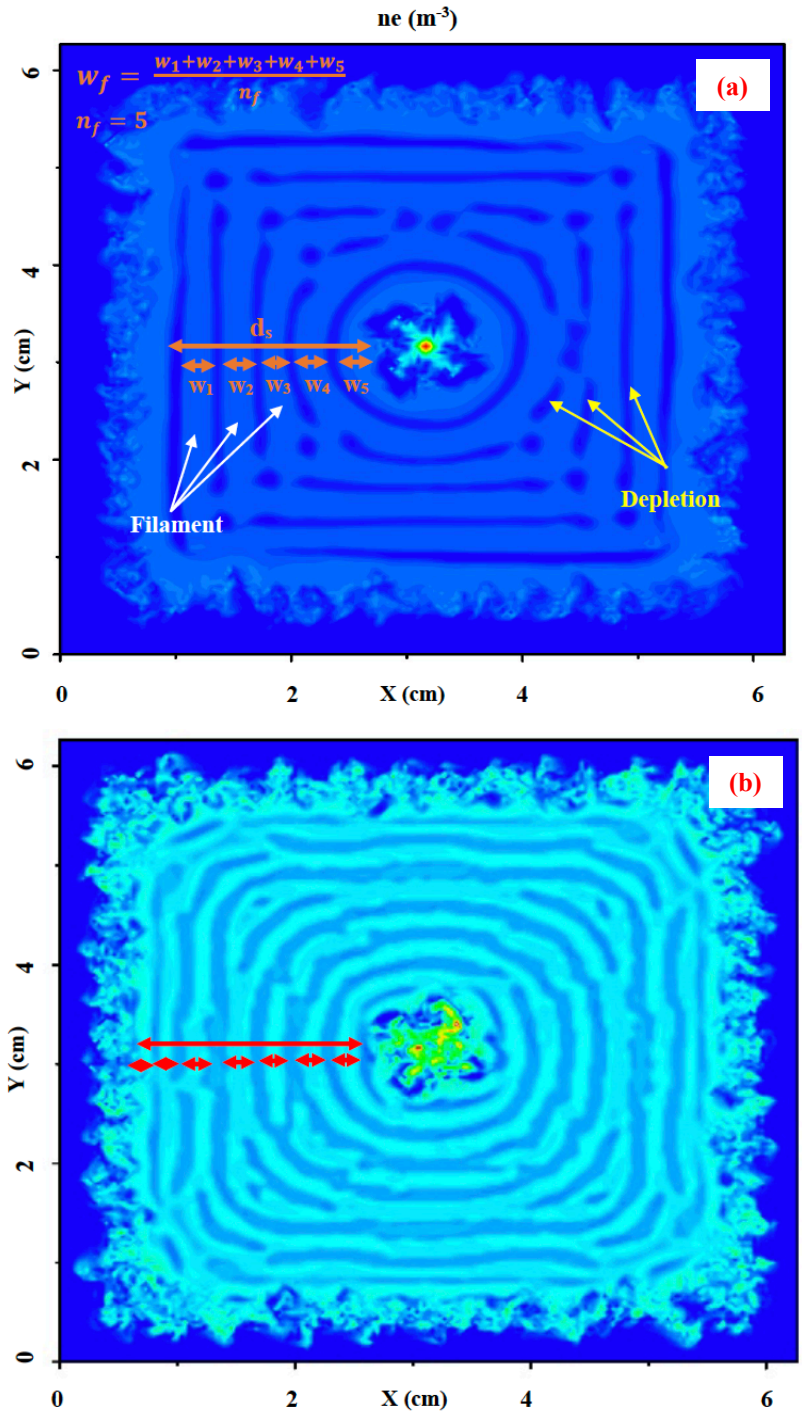

Figure 3.6: Example of filamentary structures in electron density profile to indicate the length parameters needed to calculate the defined equation for filamentation parameter (equation 3.4). Filamentation parameter for these graphs are calculated to be $30.6 = \frac{17.15\ mm}{2.8\ mm} \times 5$ in (a) and $84 = \frac{18\ mm}{1.5\ mm} \times 7$ in (b).

3.2 Simulation results

In this section, the results of the filament simulations are presented. In order to gain an insight into the physical processes that govern this process, a series of simulations are performed that consider key variables, one at a time. These variables include neutral gas pressure (neutral density), electron/ion density, gas species, and the gap between the electrodes. We will show that controlling these control parameters correspond to particular plasma scale lengths, specifically the electron Debye length, ion-neutral mean-free-path, and ion gyro-radius. This work will show that these length scales (and ratios of these length scales) may be important in determining the properties of the filaments.

In general, all of the simulations will start with a uniform background plasm (equal density for ions and electrons) within the *6.3 cm* × *6.3 cm* × *4.2 cm* simulation volume. The constant electrons and ions temperatures are $T_e = 2.5\ eV$, and $T_i = 0.025\ eV$, respectively and remain constant for the duration of the simulations. A perturbation in the form of a high-density plasma column with a density *10* times that of the background plasma, is introduced at the geometric center of the plasma chamber to trigger the formation of the filamentary patterns.

3.2.1 Filamentation Under Variation of Neutral Gas Pressure

In order to see the effect of neutral gas pressure on pattern formation in magnetized plasmas, the pressure was varied while other plasma parameters were kept constant. In these simulations, the electron/ion densities were $n_e = n_i = 5.4\times10^{15}\ m^{-3}$, electron temperature was $T_e = 2.5\ eV$, ion temperature was $T_i = 0.025\ eV$, and magnetic field was $B = 0.8\ T$. The neutral gas pressure was varied from *2.5 Pa* to *46 Pa* (*18.75 mTorr* to *345 mTorr*). The X-Y cross section of the electron density profiles for these simulations are displayed in figure 3.7.

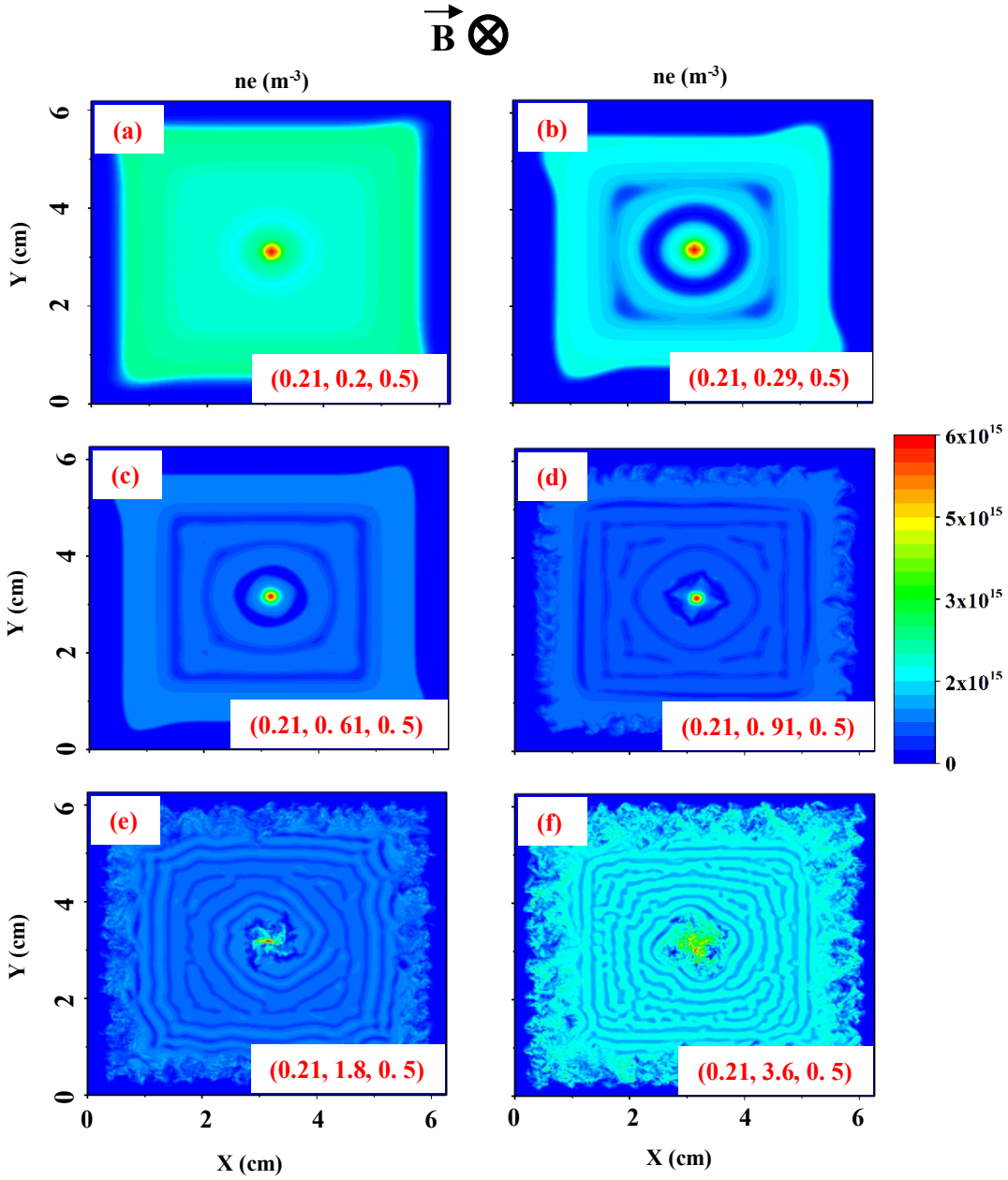

Figure 3.7: X-Y cross section of the electron density profile in magnetized argon plasma at different neutral gas pressure. a) ***46 Pa*****, b)** ***31 Pa*****, c)** ***15 Pa*****, d)** ***10 Pa*****, e)** ***5 Pa*****, f)** ***2.5 Pa*****. The electron/ion densities are 5.4 ×10^{14} m^{-3}, the plasma is exposed to** ***B = 0.8 T*** **magnetic field,** ***T_e = 2.5 eV*** **and** ***T_i = 0.025 eV*****. The profiles are taken from the middle of the plasma chamber at** ***Z = 2.1 cm*****. The set of three length parameters; (*r_i *(mm),* λ_i *(mm),* λ_{De} *(mm)*), **is also displayed on each graph. By decreasing the pressure (increasing ion mean-free-path) the pattern formed in the plasma get narrower and transition from target like to spiral structures. The graph of filamentation parameter for these plots is given in figure 3.10.**

The same patterns appear in the ion density and plasma potential profile and therefore they are not being shown here. From figure 3.7, it can be seen that by decreasing the pressure (increasing ion mean-free-path) the pattern formed in the plasma get narrower and transition from target like to spiral structures. Also, it can be seen in figure 3.7.a that, when the ion mean-free-path gets smaller than the ions gyro-radius at high pressures, no pattern forms in a magnetized plasma. This observation was checked with different sets of plasma parameters.

Based on the definition given in equation 3.4, our filamentation parameter is calculated for the six cases displayed in figures 3.7. Figure 3.8 shows the variation of the filamentation parameter with the ions mean-free-path. It can be seen in this figure that by increasing the mean-free-path (decreasing neutral gas pressure), the filamentation parameter increases significantly (second order relation). Also, the filamentation parameter drops to zero as the mean-free-path drops below the ion gyro-radius. Therefore, it can be said that the higher the fraction of $\frac{\lambda_i}{r_i}$ (ions Hall parameter) gets, the degree of filamentation increases.

The side view (X-Z cross section) of the filamentary patterns displayed in figure 3.7 are presented in figure 3.9. These graphs are in agreement with the experimental observations presented in references [23] and [24]. It is clear from these plots that the filamentary patterns are uniformly extended in Z direction along the magnetic field and behave like a one-dimensional system. Therefore, we believe that it is sufficient to rely only upon the X-Y plots to provide visual evidence for the formation of the filaments. This also demonstrates that, the actual characteristic of the pattern formation cannot be deduced from only looking into the side view of these structures, which was also noticed through the numerical works in reference [85], and a 3D modeling is needed to precisely analyze the phenomenon.

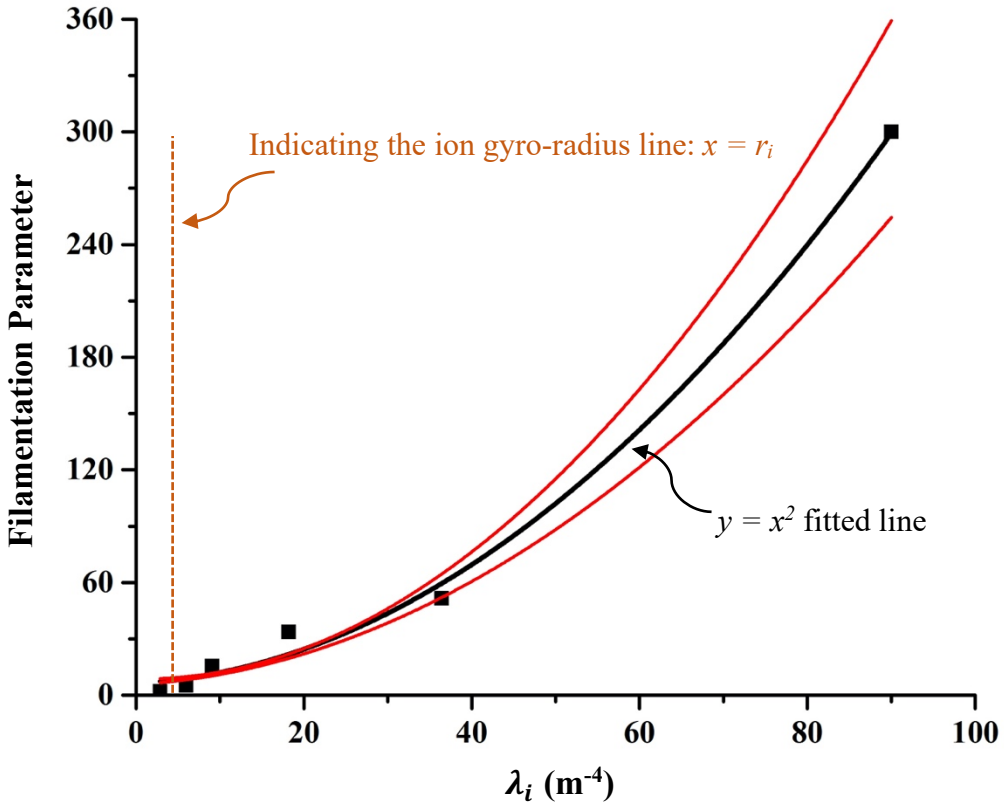

Figure 3.8: Filamentation parameter for argon plasma as a function of ion mean-free path. The red lines show upper and lower error margins in the measurement of the filamentation parameter. By increasing the mean-free-path (decreasing neutral gas pressure), filamentation parameter increases significantly (second order relation). Also, the magnetization drops to zero as the mean-free-path drops below the ion gyro-radius.

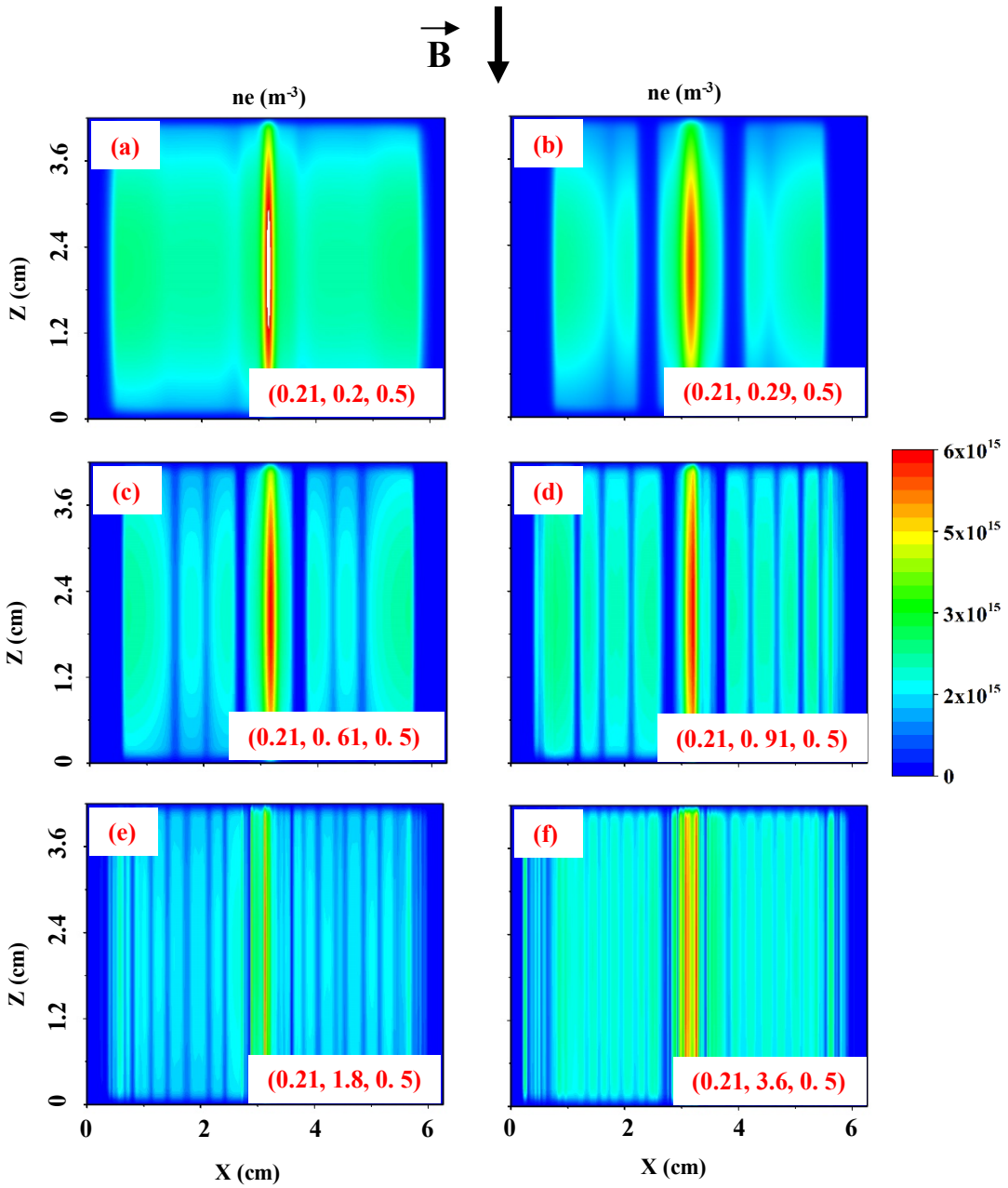

Figure 3.9: X-Z cross section of the electron density profile in magnetized argon plasma at different neutral gas pressure. These are the side view of the plots presented in figure 3.7. a) *46 Pa*, b) *31 Pa*, c) *15 Pa*, d) *10 Pa*, e) *5 Pa*, f) *2.5 Pa*. The electron/ion densities are 5.4 $\times 10^{14}\ m^{-3}$, the plasma is exposed to $B = 0.8\ T$ magnetic field, $T_e = 2.5\ eV$ and $T_i = 0.025\ eV$. The profiles are taken from the middle of the plasma chamber at $Y = 3.2\ cm$. The set of three length parameters; ($r_i\ (mm)$, $\lambda_i\ (mm)$, $\lambda_{De}\ (mm)$), is also displayed on each graph. By decreasing the pressure (increasing ion mean-free-path) more filaments appear in the plasma and they also get narrower.

To check the observations in figures 3.7.a, 3.8 and 3.9.a that ion gyro-radius must be smaller than ions mean-free-path in order to form filamentary structures, the ion gyro-radius (r_i) was reduced to *0.1 mm* by increasing the magnetic field from *0.8 T* to *1.6 T*. Figure 3.10, shows the X-Y cross section of the electron density profile for this case. It is clear from this graph that, by decreasing the ion gyro-radius below the ion mean-free-path, filamentary patterns form again in the plasma compared to figures 3.7.a and 3.9.a. This observation was also tested and demonstrated in simulations using different sets of plasma parameters.

Moreover, the continuous patterns formed in these simulations are rectangular closer to the walls and more curved in the center of the discharge. This suggests that the rectangular boundary condition assumed in these simulations is imposing its shape to the filamentary patterns. It is noted that in the experiments, a circular ring was usually placed on the electrode which may be enforcing the observed circular patterns.

In addition to that, the whole plasma rotates due to the presence of magnetic field as it has been also observed in the experiments. The flow of the plasma along the walls and the strong electric field due to the plasma sheath in that region, results in what seems to be Kelvin-Helmholtz instability. These instabilities cause the roughness of the plasma near the walls. These instabilities are suppressed at higher pressures due to higher collision rates with neutral atoms, as it can be noticed in figures 3.7.b and 3.7.c. The average speed of the rotation of the plasma due to $E \times B$ drift of the electrons and ions was measured to be approximately *300 m/s* for the case presented in figure 3.7.d which is enough to generate Kelvin-Helmholtz instability [115].

3.2.2 Filamentation Under Variation of Background Plasma Density

In another set of simulations, the background plasma density was varied while all other parameters were kept constant (*P = 12 Pa*, *B = 0.8 T*, *Te = 2.5 eV*, and *Ti = 0.025 eV*). Due to the

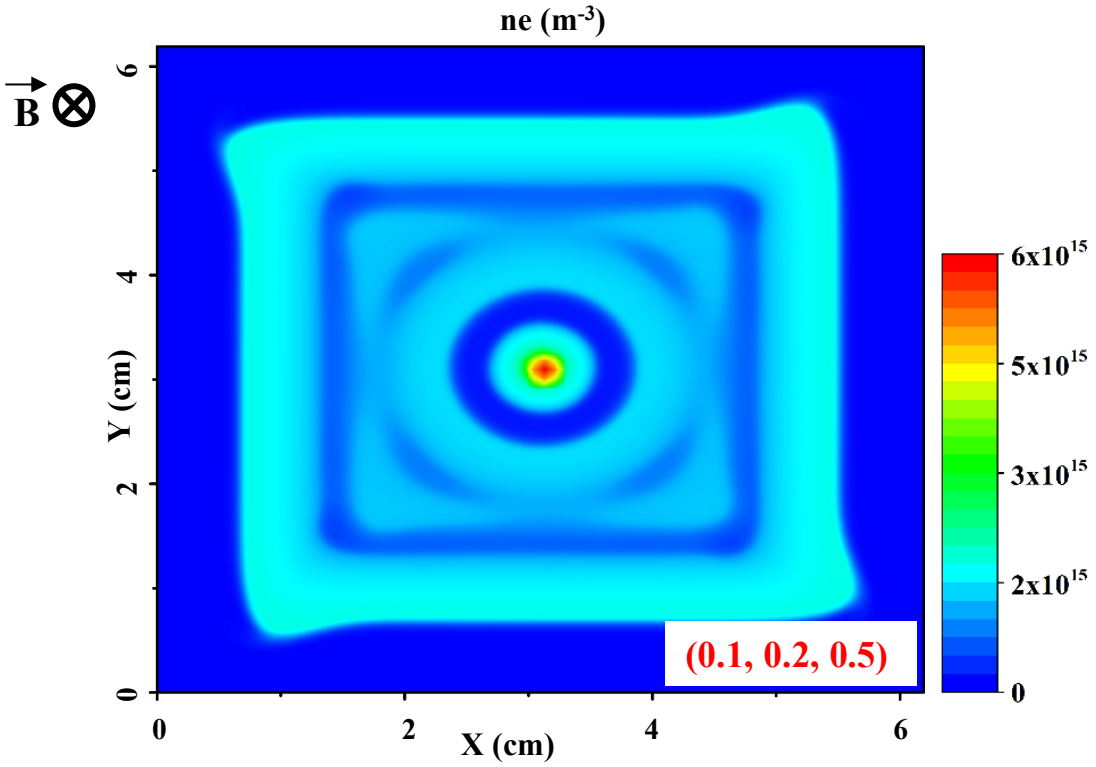

Figure 3.10: **X-Y cross section of the electron density profile in argon plasma for *P = 46 Pa* and *ne = ni = 5.4 ×10^14 m^-3*, *T_e = 2.5 eV* and *T_i = 0.025 eV*, exposed to 1.6 T magnetic field. The set of three length parameters; (*r_i (mm)*, *λ_i (mm)*, *λ_{De} (mm)*), is also displayed on the graph. This graph compared to graph 3.7.a and 3.9.a, shows the formation of filamentary structures in magnetized plasma, when the ion mean-free-path is larger than the ions gyro-radius in the plasma.**

contribution of the electron density to the electron Debye length (equation 3.3), this set of simulations is equivalent to changing electron Debye length while keeping other length parameters constant. The X-Y cross section of the electron density profiles for these simulations are displayed in figure 3.11.

It can be seen in figure 3.11 that, by increasing the electron Debye length (decreasing the electron/ion densities), the number of rectangular filamentary loops in the plasma decrease and these patterns get wider. Also, similar to the role of ion mean-free-path, if the electron Debye length is less than the ions gyro-radius, no significant pattern forms in the plasma (see figure 3.11.a). Filamentation parameter for argon plasma as a function of the electron Debye length is given in figure 3.12. The filamentation parameter decreases exponentially as the electron Debye length increases.

The variation of the filamentation parameter with the electron Debye length behaves differently from than the role of collisions. One concern is whether the scale size and/or boundaries of the simulation region are affecting the formation of the filaments. The plasma sheath is typically a couple of electrons Debye lengths in size [7] (~ 0.5-1 cm from each side) extending from the boundaries of the simulation space. The total width of the simulated chamber is only about *6 cm* which by considering the central perturbation region (about *2 cm*) does not leave enough room for the filamentary patterns to develop in the plasma.

Despite this exponential increasing of filamentation with decreasing electron Debye length, it drops to zero as the Debye length becomes smaller than the ions gyro-radius. To check this observation, the ion gyro-radius (r_i) was reduced to *0.1 mm* by increasing the magnetic field from *0.8 T* to *1.6 T*. Figure 3.13, depicts the horizontal electron density profile for this case in which narrow filamentary structure forms in the plasma as the r_i drops below the Debye length.

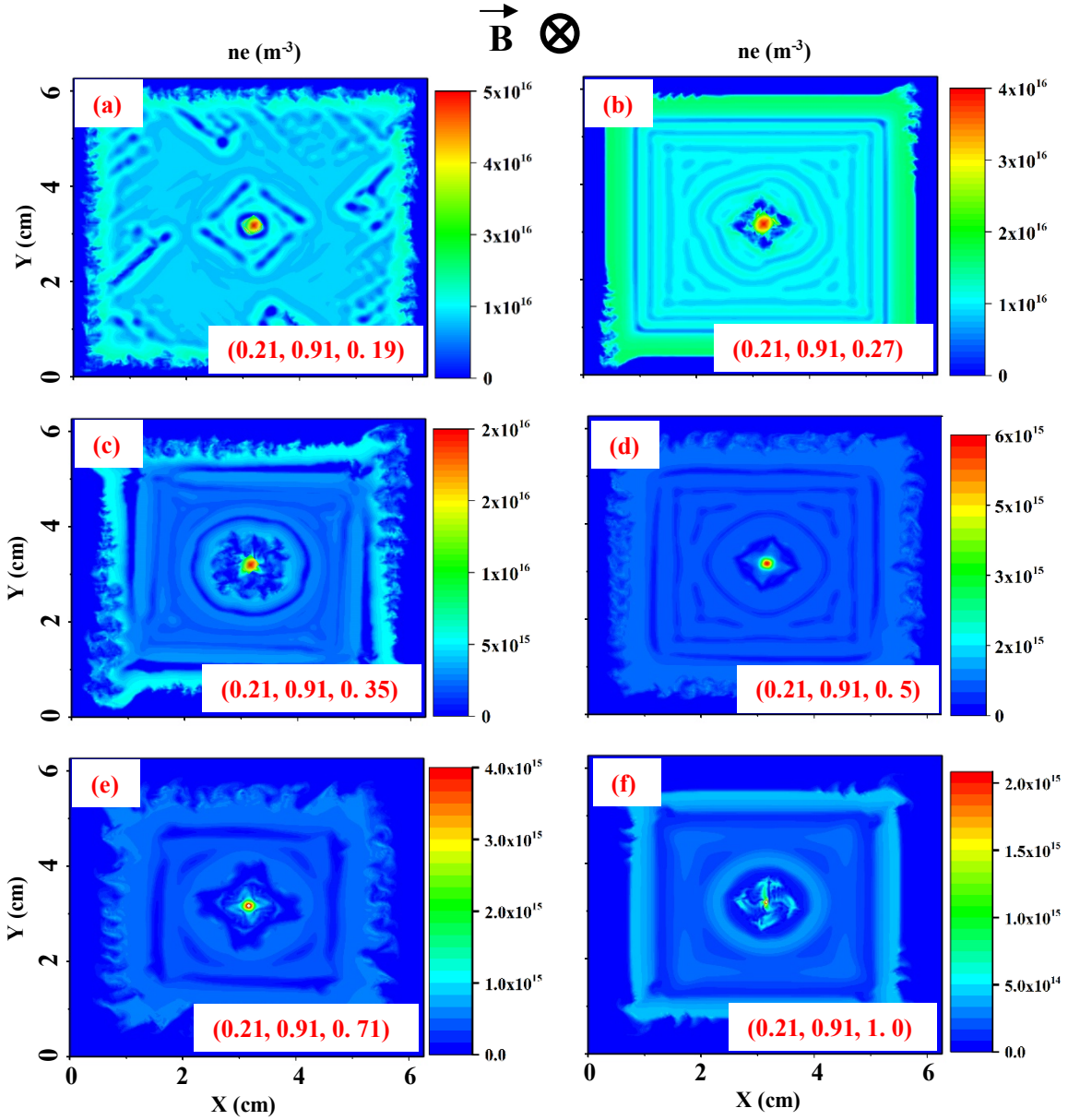

Figure 3.11: X-Y cross section of the electron density profile in magnetized argon plasma at different electron/ion densities. a) *3.4 ×10^15 m^-3*, b) *2 ×10^15 m^-3*, c) *1.1 ×10^15 m^-3*, d) 5.4 ×10^14 m^-3, e) 2.7 ×10^14 m^-3, f) 1.35 ×10^14 m^-3*. Except for case (b), in all other cases, neutral gas pressure is *P = 12 Pa*, the plasma is exposed to *B = 0.8 T* magnetic field, *T_e = 2.5 eV* and *T_i = 0.025 eV*. The set of three length parameters; (*r_i (mm)*, *λ_i (mm)*, *λ_{De} (mm)*), is also displayed on each graph. By decreasing the electron/ion density (increasing Debye length) the pattern formed in the plasma get wider and include less filamentary rectangular loops. The graph of filamentation parameter for these plots is given in figure 3.12.

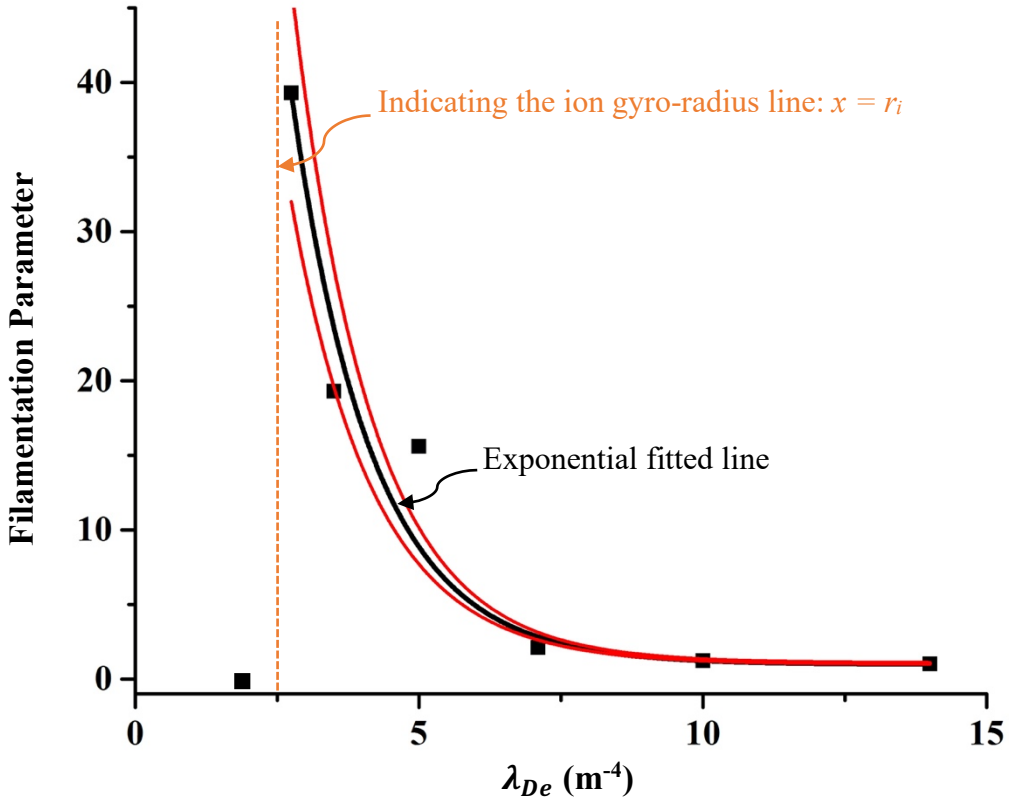

Figure 3.12: Filamentation parameter of argon plasma as a function of the electrons Debye length. The red lines show upper and lower error margins in the measurement of the filamentation parameter. Filamentation parameter increases exponentially by decreasing the Debye length and drops to zero as Debye length becomes smaller than the ions gyro-radius

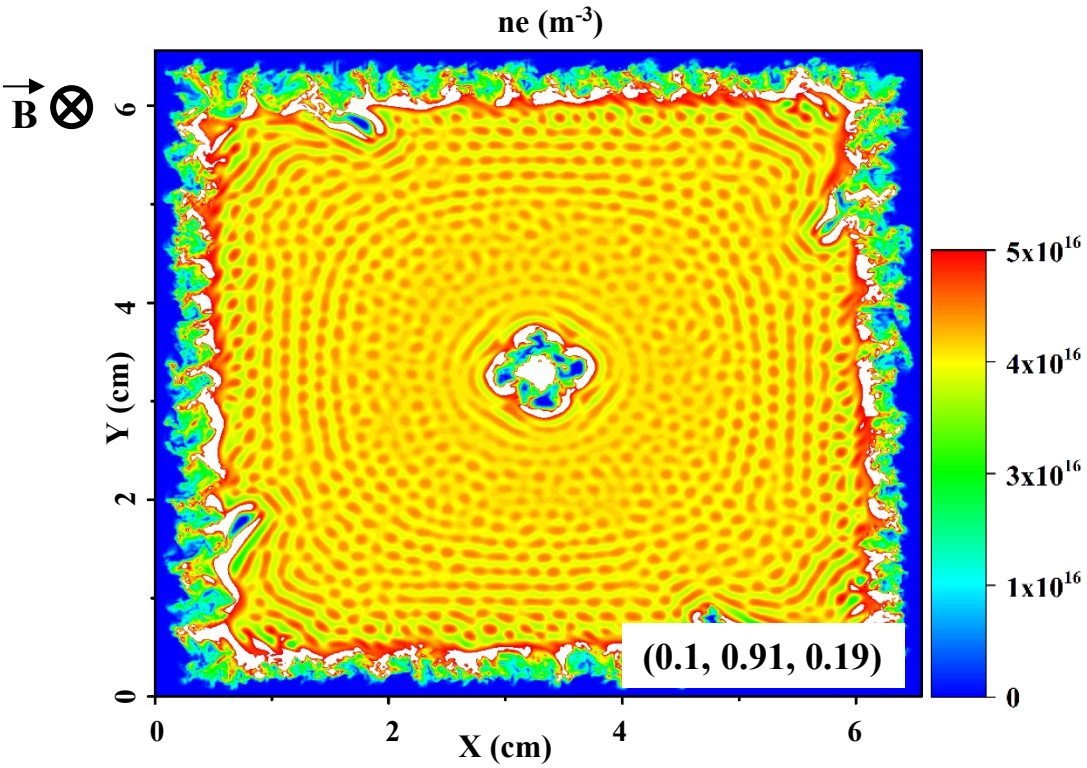

Figure 3.13: X-Y cross section of the electron density profile in argon plasma for *P = 10 Pa* and *ne = ni = 3.4 ×10^15 m^-3*, *T_e = 2.5 eV* and *T_i = 0.025 eV*, exposed to 1.6 T magnetic field. The set of three length parameters; (*r_i (mm)*, *λ_i (mm)*, *λ_{De} (mm)*), is also displayed on the graph. This graph compared to graph 15.a, shows that when the ion gyro-radius is made smaller than the electron Debye length, the filaments can re-form in the plasma.

3.2.3 Filamentation Under Variation of the Gap Between the Electrodes

It was observed in the experiments that the pattern formation in magnetized plasmas can be also affected by the gap between the top and the bottom electrodes; increasing the gap between the top and the bottom electrodes weakens the filamentation. This observation was also tested through numerical simulations. Figure 3.14 depicts the variation of the pattern formation in magnetized argon plasma at pressure of $P = 9\ Pa$ exposed to $B = 1.0\ T$ magnetic field. Shown in this figure are the formation of filaments with increasing gap size from (a) 1 cm to (f) 10.4 cm. Case (c) is the "nominal" gap of 4.2 cm. The graphs in figure 3.14 show that with increasing separation between the electrodes, there is a suppression of the filamentation. Notably, with gaps that are > 8cm, the filamentary patterns are not effectively forming in the argon plasma. The maximum vertical distances between the electrodes of the discharge to facilitate the formation of filamentary patterns, might change depending on other plasma parameters. Figure 3.15 displays the variation of the filamentation parameter with the gap between the electrodes which shows how significantly it increases as the gap between the electrodes is decreased.

3.2.4 Filamentation under Variation of Gas Type

Finally, the formation of filamentary patterns in different gas types (Ne, Ar, Kr) at a constant plasma density of $5\times10^{14}\ m^{-3}$, pressure of $9\ Pa$ and $B = 1.0\ T$, is shown in figure 3.16. In this figure, the magnetization parameter is 78.4, 30.5 and 5.8 for Ne, Ar, and Kr respectively meaning the filamentary structures are narrower and closer to one another for Ne and get wider for Ar and Kr. Since the collision cross-sections for heavier atoms are higher, the ion-neutral collision mean-free-path will be shorter for heavier atoms at the same electron/ion temperatures. The mass of the ions also affects the ion gyro-radius and the ion gyro-radius of Kr is twice of that of Ar and

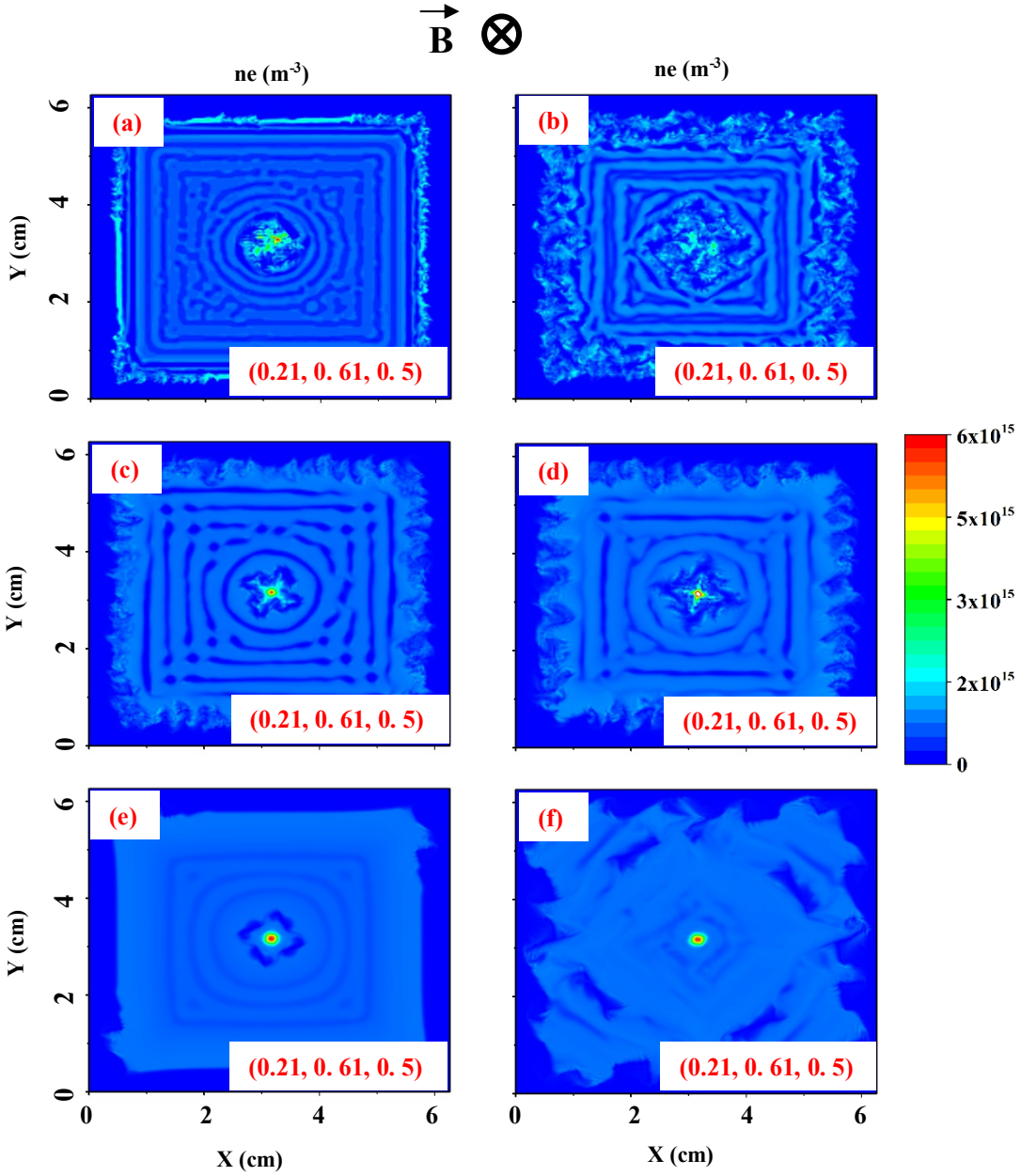

Figure 3.14: X-Y cross section profile of filamentary pattern formation in magnetized argon plasma at pressure of $P = 9\ Pa$, $T_e = 2.5\ ev$, $T_i = 0.025\ ev$, and $ne = ni = 5.0 \times 10^{14}\ m^{-3}$, exposed to $B = 1.0\ T$ magnetic field. The vertical gap between the top and the bottom electrode is different for different graphs. a) *1 cm*, b) *2.1 cm*, c) *4.2 cm*, d) *6.1 cm*, e) *8 cm*, and f) *10.4 cm*. The set of three length parameters; ($r_i\ (mm)$, $\lambda_i\ (mm)$, $\lambda_{De}\ (mm)$), is also displayed on each graph. If the electrodes are too close or too far from each other, filamentary patterns are not effectively forming in the plasma. The graph of filamentation parameter for these plots is given in figure 3.15.

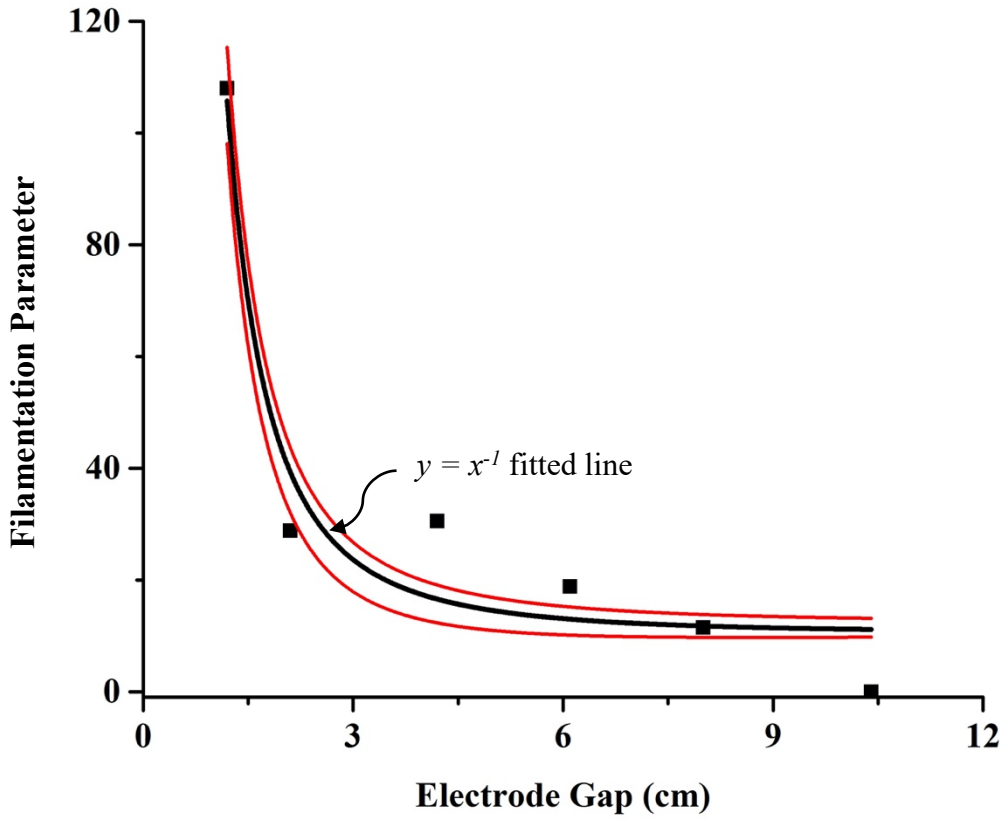

Figure 3.15: Variation of filamentation parameter with the gap between the electrodes. The red lines show upper and lower error margins in the measurement of the filamentation parameter. Filamentation parameter significantly increases as the gap between the electrodes is decreased.

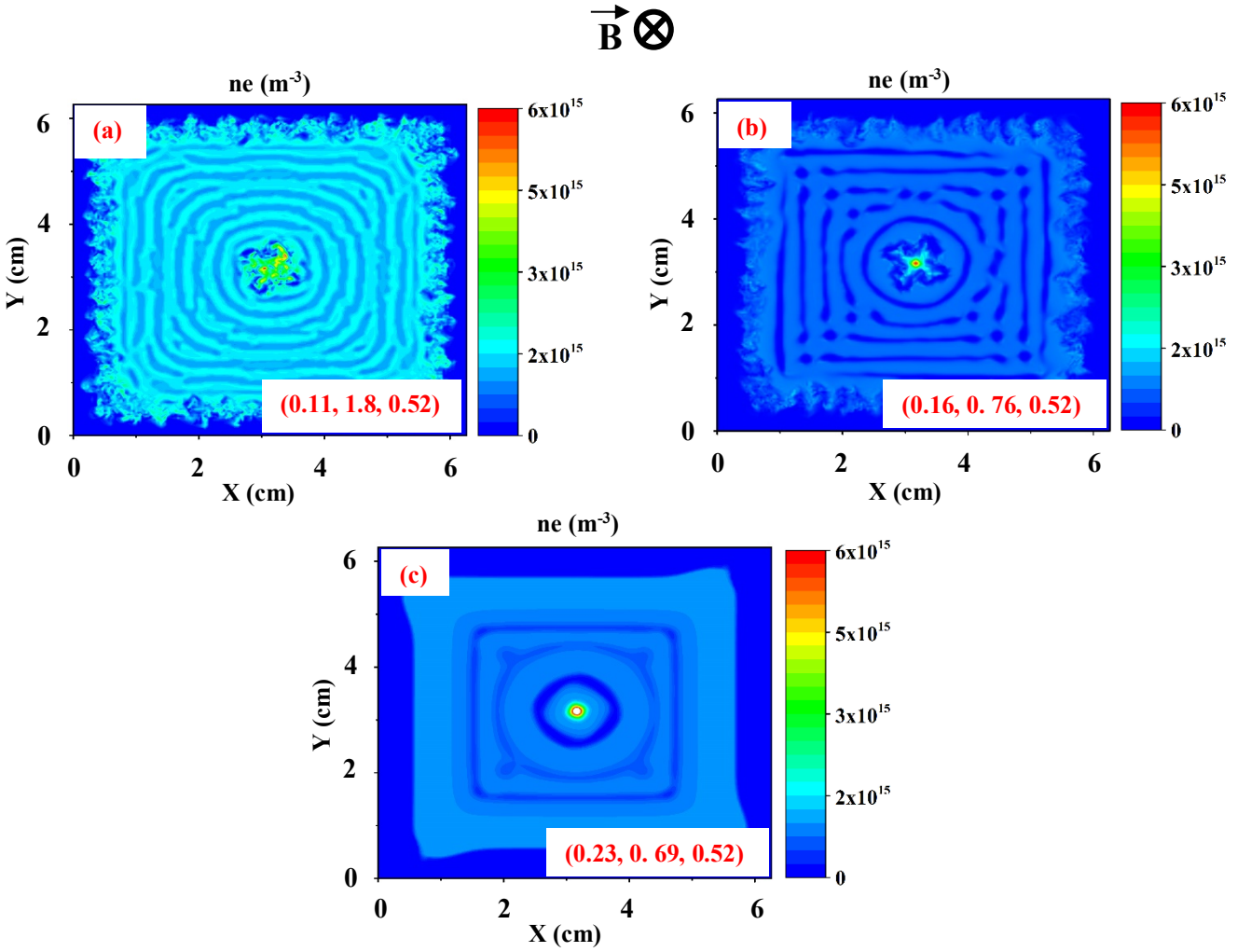

Figure 3.16: Pattern formation in Ne, Ar, and Kr at plasma density of $5\times10^{14}\ m^{-3}$ and neutral gas pressure of *10 pa*. a) Ne, b) Ar, c) Kr. In all the cases, the plasma is exposed to $B = 1.0\ T$ magnetic field, $T_e = 2.5\ eV$, and $T_i = 0.025\ eV$.

is quadruple the ion gyro-radius of Ne. This suggests again that with lower fraction of $\frac{\lambda_i}{r_i}$, the filamentation parameter of the plasma is reduced. These results are consistent with the graphs presented in figures 3.7 and 3.8.

3.3 Discussion on the Results of Filamentation Simulations

Without collisions with other species, the electrons and ions would not be able to diffuse across the magnetic field in a highly magnetized plasma. The derivation of the cross magnetic field diffusion of the electrons and ions in a magnetized plasma is described in many standard plasma physics textbooks [6] [7]. If electron/ion temperatures in the plasma are assumed to be constant ($\boldsymbol{\nabla} P_\alpha = K_b T_\alpha \boldsymbol{\nabla} n_\alpha$), equation 2.4 can be rewritten as:

$$q_\alpha n_\alpha (\boldsymbol{E} + \boldsymbol{V}_\alpha \times \boldsymbol{B}) - K_b T_\alpha \boldsymbol{\nabla} n_\alpha - m_\alpha n_\alpha \upsilon_\alpha \boldsymbol{V}_\alpha = 0 \tag{3.5}$$

where, q_α is charge, n_α is density, $\boldsymbol{E}$ is electric field, $\boldsymbol{V}_\alpha$ is velocity vector, $\boldsymbol{B}$ is magnetic field vector, P_α is pressure, m_α is mass, and υ_α is collision frequency with neutral atoms.

In cylindrical coordinate system, if it is assumed that $\mathbf{B} = \mathrm{B}_0 \hat{\boldsymbol{z}}$, the radial and azimuthal elements of the electrons/ions fluxes (fluxes of the particles perpendicular to the magnetic field) can be derived as described in [6] [7]:

$$\Gamma_{\alpha_r} = \pm \mu_\alpha n_\alpha E_r - D_\alpha \nabla n_r + \frac{\omega_{c\alpha}}{\upsilon_\alpha} \Gamma_{\alpha_\varphi} \tag{3.6}$$

$$\Gamma_{\alpha_\varphi} = \pm \mu_\alpha n_\alpha E_\varphi - D_\alpha \nabla n_\varphi - \frac{\omega_{c\alpha}}{\upsilon_\alpha} \Gamma_{\alpha_r} \tag{3.7}$$

in which Γ_{α_r} is the radial element of the flux, Γ_{α_φ} is the azimuthal element of the flux, μ_α is mobility, D_α is diffusion coefficient, $\omega_{c\alpha}$ is cyclotron frequency, and υ_α is the collision frequency with neutral atoms for species α. The coefficients in equations 3.6 and 3.7 are defined as below:

$$\mu_\alpha = \frac{q_\alpha}{m_\alpha \upsilon_\alpha} \tag{3.8}$$

$$D_\alpha = \frac{K_b T_\alpha}{m_\alpha \upsilon_\alpha} \tag{3.9}$$

$$\omega_{c\alpha} = \frac{q_\alpha B_0}{m_\alpha} \tag{3.10}$$

$$\upsilon_\alpha = n_g \sigma_\alpha V_{th}, \tag{3.11}$$

Solving for Γ_{α_r} and Γ_{α_φ} in equations 3.6 and 3.7, the general form of the electrons/ions flux components perpendicular to the magnetic field ($\Gamma_{\alpha_\perp}$) can be derived as:

$$\overrightarrow{\Gamma_{\alpha_\perp}} = \pm \mu_{\alpha_\perp} n_\alpha \overrightarrow{E_\perp} - D_{\alpha_\perp} \overrightarrow{\nabla n_\perp} + \frac{\overrightarrow{\Gamma_{\alpha_E}} + \overrightarrow{\Gamma_{\alpha_D}}}{1 + \frac{\upsilon_\alpha{}^2}{\omega_{c\alpha}{}^2}} \tag{3.12}$$

$$\mu_{\alpha_\perp} = \frac{\mu_\alpha}{1 + \frac{\omega_{c\alpha}{}^2}{\upsilon_\alpha{}^2}} \tag{3.13}$$

$$D_{\alpha_\perp} = \frac{D_\alpha}{1 + \frac{\omega_{c\alpha}{}^2}{\upsilon_\alpha{}^2}} \tag{3.14}$$

Although derivation of equation 3.12 was done in cylindrical coordinate system, the form of the cross magnetic field diffusion is general and can be used for any other coordinate systems.

In this equation, $\Gamma_{\boldsymbol{\alpha_E}}$ and $\Gamma_{\boldsymbol{\alpha_D}}$ are the fluxes due to $\boldsymbol{E}\times\boldsymbol{B}$ and diamagnetic drift ($\boldsymbol{\nabla} n \times \boldsymbol{B}$) respectively. These terms indicate the contribution of azimuthal components of electric field and density gradient into the radial element of the flux and vice versa. The $\boldsymbol{E}\times\boldsymbol{B}$ and diamagnetic drift exist only in presence of magnetic field and are defined as below:

$$\Gamma_{\boldsymbol{\alpha_E}} = n_\alpha \frac{\boldsymbol{E}\times\boldsymbol{B}}{{B_0}^2} \tag{3.15}$$

$$\Gamma_{\boldsymbol{\alpha_D}} = -\frac{K_b T_\alpha}{q_\alpha {B_0}^2} \boldsymbol{\nabla} n \times \boldsymbol{B} \tag{3.16}$$

In the last term in equation 3.12, the diffusion due to $\boldsymbol{E}\times\boldsymbol{B}$ and diamagnetic drift, ($\Gamma_{\boldsymbol{\alpha_E}}$ and $\Gamma_{\boldsymbol{\alpha_D}}$), are slowed down by collisions while the first two terms will have non-zero values only due to the collisions of electrons/ions with each other and with the neutral gas atoms. It has to be noted that mobility and diffusion coefficients perpendicular to the magnetic field are modified by a factor of $(1 + \frac{{\omega_\alpha}^2}{{\upsilon_{c\alpha}}^2})^{-1}$ and decrease with increasing the applied magnetic field. Also, the fraction of $\frac{\omega_\alpha}{\upsilon_{c\alpha}}$ in the modification coefficients is the Hall parameter and is mathematically the same as $\frac{\lambda_\alpha}{r_\alpha}$, as discussed in the previous section.

Moreover, as it can be seen in the schematic drawing in figure 3.18, when target like filamentary patterns are formed in the magnetized plasma, E_φ and $\frac{\partial n_\alpha}{\partial \varphi}$ are equal to zero due to the symmetry of the structure. Therefore, from equation 3 .12 we get:

$$\Gamma_{\boldsymbol{\alpha r}} = \pm\mu_{\alpha\perp} n_\alpha E_r - D_{\alpha\perp} \nabla n_r \tag{3.17}$$

$$\Gamma_{\alpha\varphi} = \frac{1}{1+\frac{{\upsilon_\alpha}^2}{{\omega_{c\alpha}}^2}} \left(-\frac{n_\alpha E_r}{B_0} + \frac{K_b T_\alpha}{q_\alpha B_0} \nabla n_r\right) \tag{3.18}$$

Considering equations 3.8-3.11 and 3.13-3.14, it can be easily obtained from equation 3.18 that [7]:

$$\Gamma_{\alpha_\varphi} = -\frac{\omega_{c\alpha}}{\upsilon_\alpha}\,\Gamma_{\alpha_r} \tag{3.19}$$

$$\Gamma_{\alpha_\varphi} = -\frac{\omega_{c\alpha}}{\upsilon_\alpha}(\pm\mu_{\alpha_\perp} n_\alpha E_r - D_{\alpha_\perp}\nabla n_r) \tag{3.20}$$

Therefore, for target-like (circular) filamentary patterns, it can be said that E_r and ∇n_r cause a flux of particles not only in radial direction but also in the azimuthal direction due to the presence of the magnetic field. Equation 3.17 is specifically interesting in the limit that $\upsilon_i = \omega_{ci}$ ($\lambda_i = r_i$), from equation 3.16-3.19 we get:

$$\Gamma_{i_\varphi} = -\Gamma_{i_r} = -\frac{1}{2}(\mu_i n_i E_r - D_i \nabla n_r) \tag{3.21}$$

which means that that E_r and ∇n_r contribute equally to the radial and azimuthal ion fluxes. This is the threshold limit for magnetization of the ions (where ions' Hall parameter equals one). At high pressure for which $\upsilon_i > \omega_{ci}$, where the ions are not magnetized enough to make at least one full rotation before colliding with a neutral gas atom.

Figure 3.18 displays the variation of perpendicular mobility and diffusion coefficient of the electrons and ions with pressure, for a magnetized argon plasma exposed to *0.8 T* magnetic field. The electron and ion temperatures are assumed to be *2.5 eV* and *0.025 eV* respectively. It can be seen in this figure that the perpendicular mobility and diffusion coefficients of the electrons/ions first increase with the pressure and then decrease, but the mobility and diffusion coefficient of the ions reach their maxima before the electrons. At a critical pressure (*P = 44.75 Pa* for the presumed plasma parameters here) we get $\upsilon_i = \omega_{ci}$ ($\lambda_i = r_i$) and the mobility and diffusion coefficient of

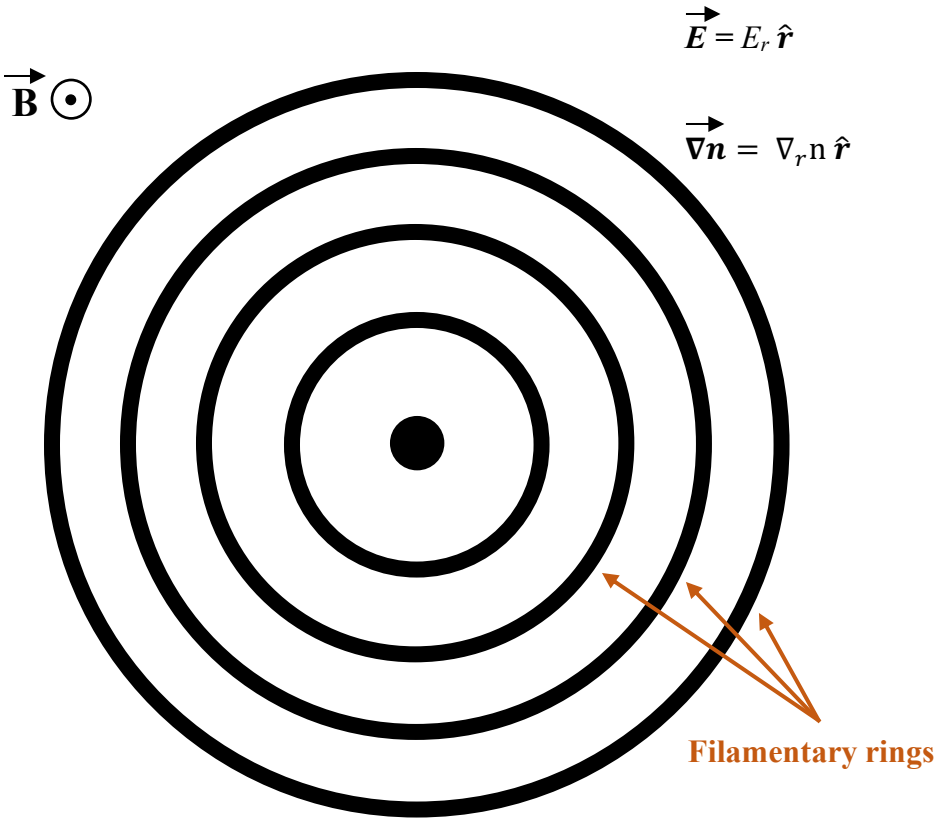

Figure 3.17: Schematic drawing of target like filamentary structure formed in a magnetized plasma. Due to symmetry of the structure, both electric field and gradient of density are radial in the body of the plasma far enough from the walls.

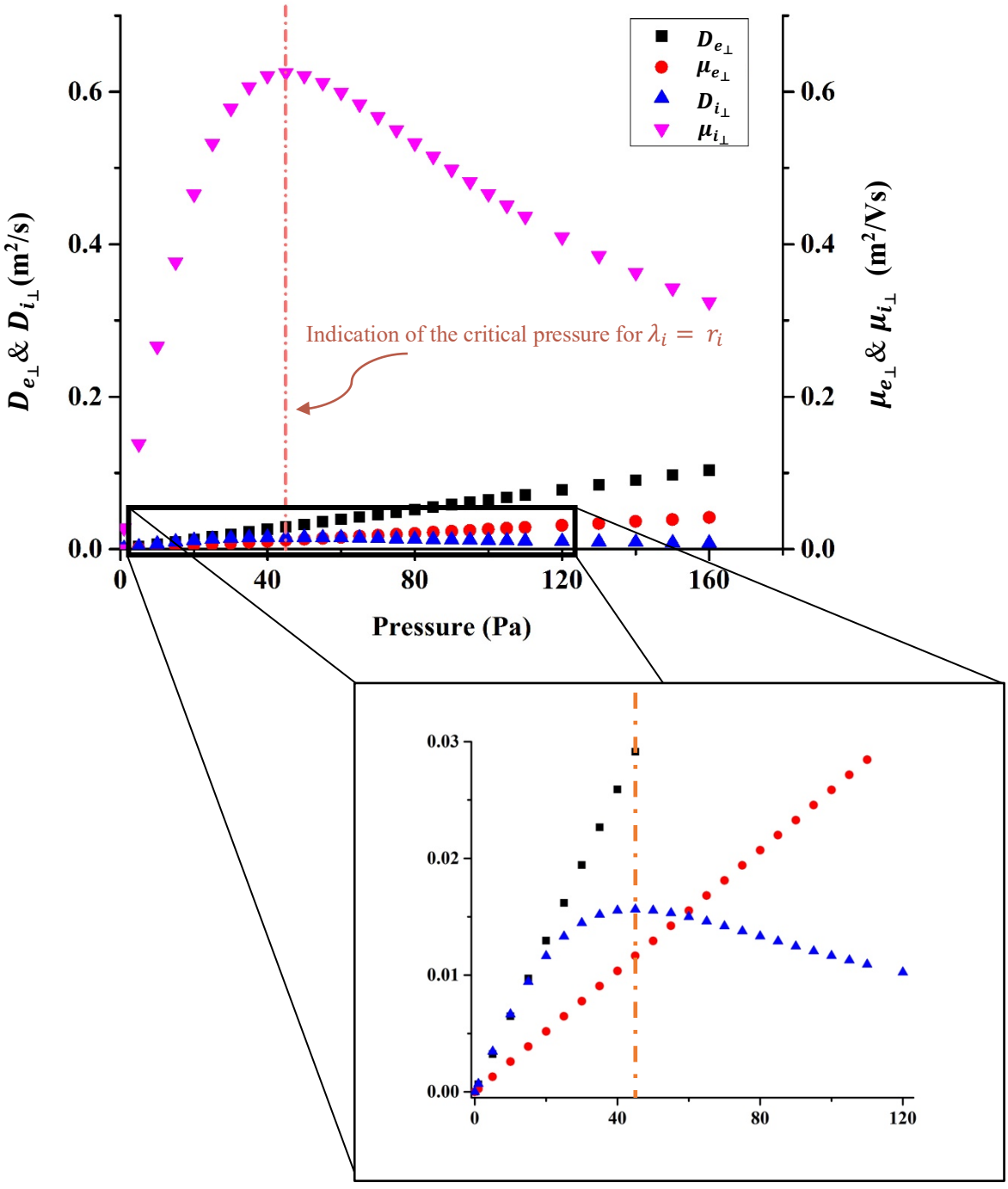

Figure 3.18: The variation of perpendicular mobility and diffusion coefficients of the electrons and ions with pressure, for magnetized argon plasma exposed to *0.8 T* magnetic field. The electron and ion temperatures are assumed to be *2.5 eV* and *0.025 eV* respectively.

the ions start to decrease with pressure. By contrary, the mobility and diffusion of the electrons are still increasing with pressure at this limit. These effects together, will wash out the patterns formed in the plasma and as a result, filamentary patterns are not forming in the magnetized plasma as λ_i gets smaller than r_i or when the pressure goes beyond the critical pressure.

The approach for deriving the limit of $\upsilon_i = \omega_{ci}$ ($\lambda_i = r_i$) was based on the assumption that a radial electric field exists in filamented magnetized plasmas perpendicular to the magnetic field. To justify the presence of such an electric field, it has to be noted that although the filamentary patterns in the electron and ion density profile are exactly the same, the numerical values of these densities are slightly different from each other. Figure 3.19 shows the filamentary patterns formed in electron and ion density profiles in an argon plasma at pressure of *9 Pa* exposed to *1.0 T* magnetic field. As it can be seen in figure 3.19.c, the electron density in the depletion regions of a filamented magnetized plasma, drops more than the ions, resulting in a higher number of the ions in these regions. This higher number of the ions in the depletion region gives rise to a pattern in the plasma potential profile (figure 3.19.d), which is the same as that of the electron/ion density profiles. Due to symmetry, this potential profile creates only a horizontal component in the central part of the plasma, as displayed in figure 3.20.

Another interesting point in figures 3.19 and 3.20 is the waveform (sine and cosine function form) of the electron/ion density, plasma potential and electric field profiles. If a filament and its neighboring depletion region is considered to have different width in general, piecewise functions can be assumed for describing the electron/ion densities:

$$n_e = \begin{cases} n_0 + n_{e1}\sin(\frac{\pi r}{w_f}) & 0 \le r < w_f \\ n_0 - n_{e2}\sin(\frac{\pi(r-w_f)}{w_d}) & w_f \le r \le w_f + w_d \end{cases} \tag{3.22}$$

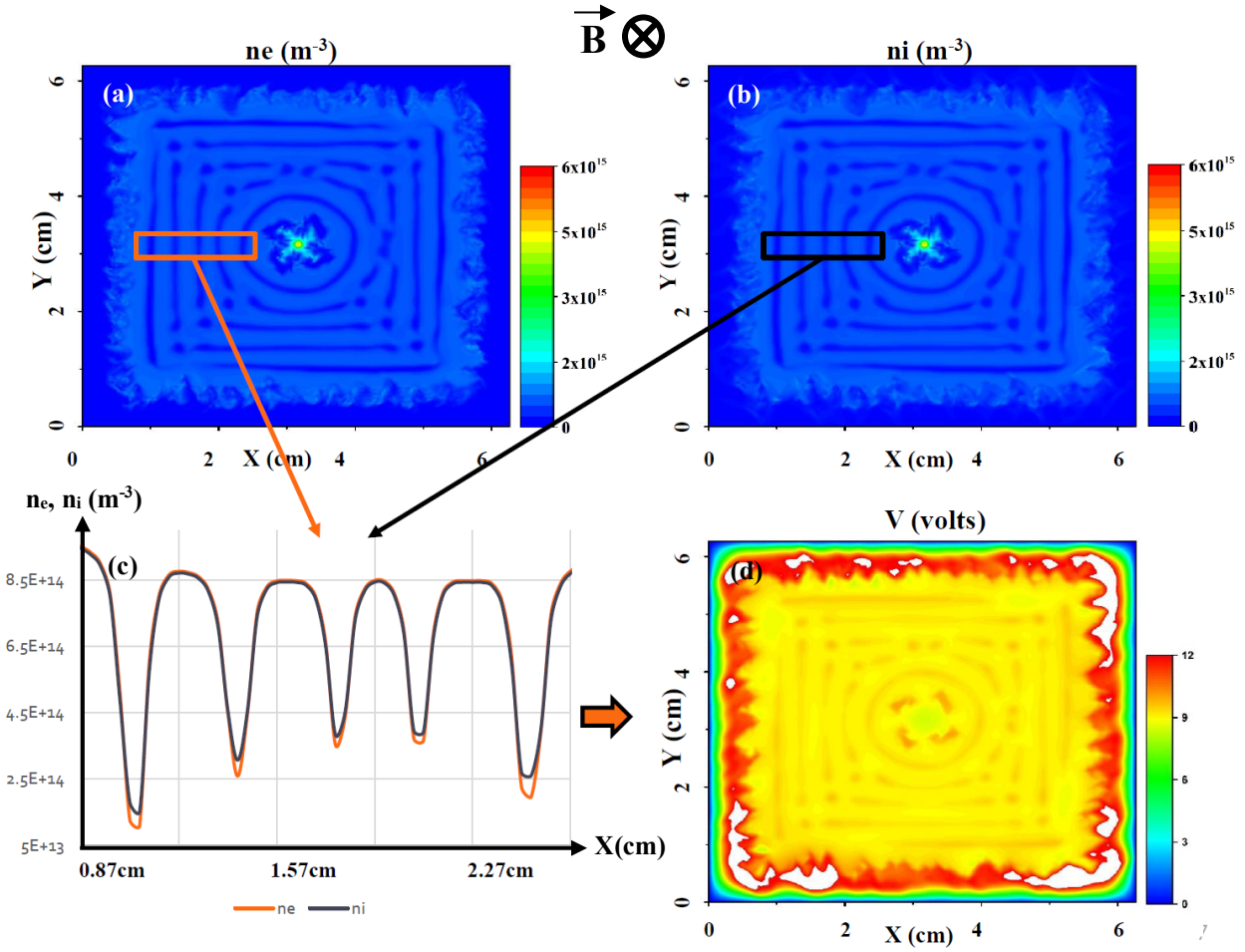

Figure 3.19: X-Y cross section electron density profile (a), ion density profile (b), their differences in the filamentary and depletion regions (c), and the resultant plasma potential profile (d), in the middle of an argon plasma chamber at pressure of *9 Pa*, exposed to *1.0 T* magnetic field. Initial plasma density is uniform of the order $5\times10^{14}\ m^{-3}$ and electron and ion temperature are $T_e = 2.5\ eV$ and $T_i = 0.025\ eV$ respectively. The electron density drops more than the ion density in the depletion regions, resulting in a higher number of ions in these regions which gives rise to a pattern in the plasma potential profile which is exactly the same as that of electron/ion density profiles.

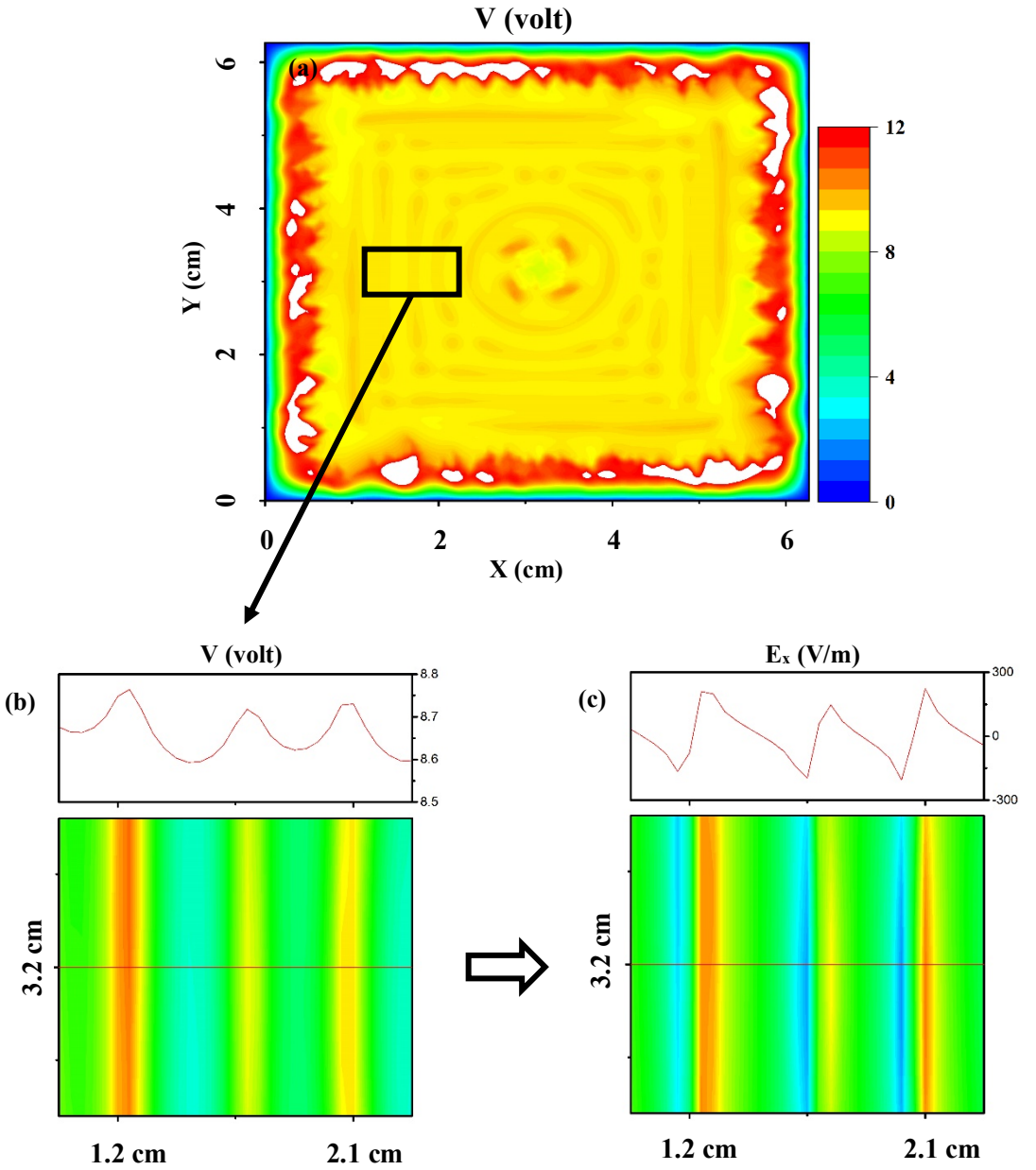

Figure 3.20: a) X-Y cross section of plasma potential profile in the middle of a magnetized argon plasma chamber at pressure of *9 Pa* exposed to *1.0 T* magnetic field. Initial plasma density is uniform of the order $5\times10^{14}\ m^{-3}$ and electron and ion temperature are $T_e = 2.5\ eV$ and $T_i = 0.025\ eV$ respectively. b) Magnified plasma potential in the section indicated with a black box in part (a), c) The resultant electric field due to the plasma potential displayed in part (b). The electric field in this part of the plasma only has a horizontal component (E_x).

$$n_i = \begin{cases} n_0 + n_{i1} \sin\left(\frac{\pi r}{w_f}\right) & 0 \le r < w_f \\ n_0 - n_{i2} \sin\left(\frac{\pi (r - w_f)}{w_d}\right) & w_f \le r \le w_f + w_d \end{cases} \quad (3.23)$$

in which n_0 is the background electron/ion density (mostly $n_0 = 5.4 \times 10^{14}\ m^{-3}$ in the presented simulations), n_{1e} is the rise of electron density in the filament relative to n_0, n_{2e} is the drop of electron density in the depletion region relative to n_0, n_{1i} is the rise of ion density in the filament relative to n_0, n_{2i} is the drop of ion density in the depletion region relative to n_0, w_f is the width of the filament, and w_d is the width of the depletion region. These quantities are displayed on the schematic drawing in figure 3.21.

Although both electric field and gradient of density push the electrons from the filament to the depletion region, the mobility and diffusion coefficient of the electrons in magnetized plasmas is too small (at pressures below the critical pressure), to make this process happen. Also, at the boundary of the filament and depletion region ($r = w_f$ in figure 3.21), the repulsive force from the excess of the ions in the depletion region cancels out the gradient of ions density from the filament to the depletion region. These two effects together maintain the filamentary structure formed in the magnetized plasma. Therefore, when the filamentary pattern is fully established, the cross magnetic field diffusion of the ions becomes zero and from equation 3.17 we get:

$$\mu_{i_\perp} n_i E_r = D_{i_\perp} \nabla n_i \quad (3.24)$$

Also, using electron and ion density, Poisson's equation in the plasma can be written as:

$$\nabla \cdot \boldsymbol{E} = \frac{e(n_i - n_e)}{\varepsilon_0} \quad (3.25)$$

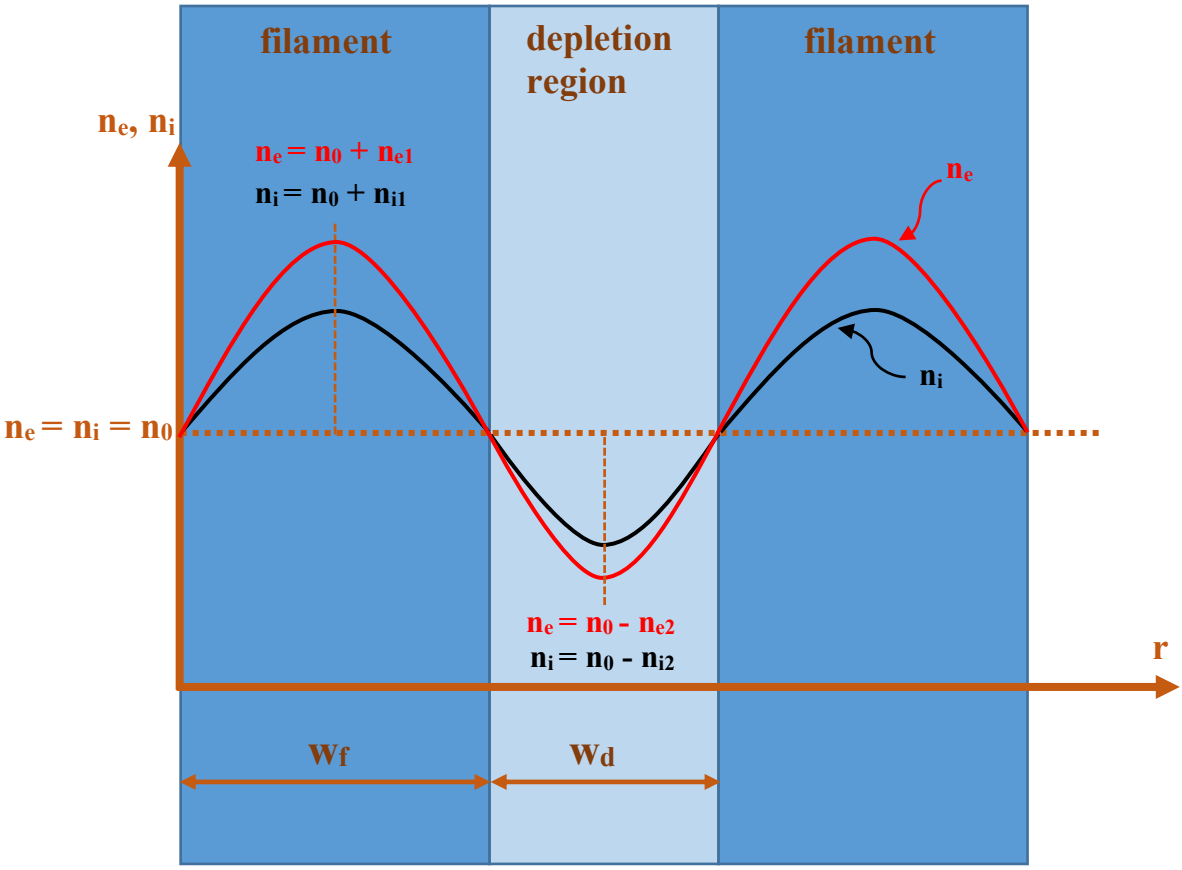

Figure 3.21: Schematic drawing of consecutive filament and depletion region in "r" direction for a cylindrically symmetric filamentary pattern (like the one shown in figure 28). Also, the graph of the electron and ion densities as a function of position is drawn on the figure. The graph of electron density is drawn in red and the graph of ion density is drawn in black.

in which $\boldsymbol{E}$ is the electric field vector, and e is unit charge. Plugging in for the densities from equations 3.22 and 3.23, and by considering cylindrical symmetry in target like filamentary patterns ($\boldsymbol{E} = \boldsymbol{E_r}$):

$$\frac{\partial E_r}{\partial r} = \frac{e(n_{i1}-n_{e1})}{\varepsilon_0}\sin(\frac{\pi r}{w_f}) \qquad 0 \le r < w_f \tag{3.26}$$

$$\frac{\partial E_r}{\partial r} = \frac{e(n_{e2}-n_{i2})}{\varepsilon_0}\sin(\frac{\pi(r-w_f)}{w_d}) \qquad w_f \le r \le w_f + w_d \tag{3.27}$$

By considering $E_r = -E_0 cos(\frac{\pi r}{w_f})$ in the filamentary region ($0 \le r < w_f$), and plugging it into equation 3.26 we get:

$$E_0 = \frac{e(n_{i1}-n_{e1})}{\pi\varepsilon_0} w_f \tag{3.28}$$

Therefore, at the boundary of the filament and depletion region ($r = w_f$ in figure 3.21), equation 3.24 gives:

$$-\mu_{i\perp}(n_0 + n_{i1}\, sin\frac{\pi r}{w_f})\, E_0 cos(\frac{\pi r}{w_f}) = D_{i\perp}\frac{\partial}{\partial r}(n_0 + n_{i1}\, sin(\frac{\pi r}{w_f})) \qquad \text{at} \qquad r = w_f \tag{3.29}$$

$$\Rightarrow \quad -\mu_{i\perp} n_0 \mathrm{E}_0 = D_{i\perp}\frac{\pi n_{i1}}{w_f} \tag{3.30}$$

By plugging in for $\mu_{i\perp}$, $D_{i\perp}$, and E_0 from equations 3.13, 3.14 and 3.28 respectively:

$$\Rightarrow \quad \frac{e^2 n_0}{\pi\varepsilon_0}(n_{e1} - n_{i1}) w_f = K_b T_i \frac{\pi n_{i1}}{w_f} \tag{3.31}$$

$$\Rightarrow \quad w_f^2 = \frac{\varepsilon_0 K_b T_i}{e^2 n_0}\frac{\pi^2 n_{i1}}{(n_{e1}-n_{i1})} \tag{3.32}$$

$$\Rightarrow \quad w_f^2 = \lambda_{Di}^2 \frac{\pi^2 n_{i1}}{(n_{e1} - n_{i1})} \tag{3.33}$$

in which λ_{Di} is the ions Debye length.

In the same way, by starting from equation 3.27 and following the same steps, we can calculate the width of the depletion regions as:

$$w_d^2 = \lambda_{Di}^2 \frac{\pi^2 n_{i2}}{(n_{e2} - n_{i2})} \tag{3.34}$$

Although equations 3.33 and 3.34 need the unknown variables of n_{i1}, n_{e1}, n_{i2}, and n_{e2} to give the exact equation for calculating the width of filaments and depletion regions in a filamentary structure, they are still very interesting equations. According to these equations, by increasing the background plasma density (decreasing λ_{Di}), the width of the filaments and depletion regions or equivalently filamentation parameter (equation 3.4) should increase. This conclusion is consistent with the results depicted in figure 3.12.

At steady state, by integrating the continuity equations for electrons and ions over the volume of one depletion region or one filament, we can get two more equations in each region to be solved along with equations 3.33 and 3.34 to get the exact value of w_f and w_d. Unfortunately, these sets of equations can only be solved numerically. These sets of equations are given below:

$$\begin{cases} \int (\nabla . \Gamma_i - \sigma_I + \sigma_L) dv = 0 \\ \int (\nabla . \Gamma_e - \sigma_I + \sigma_L) dv = 0 \\ w_f^2 = \lambda_{Di}^2 \frac{\pi^2 n_{i1}}{(n_{e1} - n_{i1})} \end{cases}$$

(Solve over the full volume of one filament)

$$\begin{cases} \int(\nabla.\Gamma_i - \sigma_I + \sigma_L)dv = 0 \\ \int(\nabla.\Gamma_e - \sigma_I + \sigma_L)dv = 0 \\ w_d^2 = \lambda_{Di}^2 \frac{\pi^2 n_{i2}}{(n_{e2} - n_{i2})} \end{cases}$$ (Solve over the full volume of one depletion region)

The variables n_{i1}, n_{e1}, n_{i2}, and n_{e2} can be functions of the gap between the electrodes and plasma parameters such as pressure and magnetic field.

Based on all data presented in this section through fluid simulations of filamentary pattern formation in magnetized plasmas, the following procedure can be assumed for the formation of filamentary structures in electric discharges exposed to strong magnetic fields:

1- In a highly magnetized plasma, a fluctuation in the plasma density grows in time as the electrons and ions are trapped in the magnetic field and local instabilities in the plasma do not simply get washed out as they would in a non-magnetized plasma. The enhanced plasma density can only expand parallel to the magnetic field, finally becoming a single filament parallel to the magnetic field lines.

2- In the filament as well as the rest of the plasma, electrons which are much more magnetized and much lighter than ions diffuse faster than ions to the walls parallel to the magnetic field, leaving the heavy ions behind. Since the density is enhanced in the filament, the loss of the electrons will be relatively higher too, giving the filament a relatively higher potential than the neighboring points. This relatively higher potential results in a radial electric field pointed out of the filament and perpendicular to the magnetic field.

3- Although the strong magnetic field reduces the cross magnetic field diffusion of the electrons and ions, these cross magnetic field diffusions are never reduced to zero. Specifically for the ions, their larger mass compared to the electrons helps them have a limited diffusion across magnetic field through their collisions with the neutral atoms [7].

This is mostly because the cross magnetic field mobility of the ions is much more than that of the electrons as it was also noted in figure 3.17. With the help of this relatively high mobility, the radial electric field of the positively charged filament expels the nearby ions outward.

4- The expelled ions sit at a distance from the filament where the electric field is not as strong and the inward gradient of density of the ions can cancel out the repulsive force of the electric field. Now, the first filamentary ring around the central filament has been stablished. These rippled ions in the first filamentary ring, repel the nearby ions and therefore establishing the next filamentary ring through the same process.

5- The slightly higher density of the ions in the established filamentary rings, slightly hinders the parallel diffusion of the electrons, creating a region with enhanced electron and ion densities which as it grows further in time, forms what we call here a filamentary ring extended in the plasma parallel to the magnetic field.

6- The regions in between the filamentary rings that a fraction of their ions has been repelled, allow for more electrons to diffuse to the walls parallel to the magnetic field to compensate for the repelled ions. As the time passes, these regions get more repelled ions and more diffused electrons parallel to the magnetic field resulting in a region which we call a depletion region. In this process the diffusion of plasma is non-ambipolar in cross-field direction which is one of the important outcomes of the transport of electrons/ions under the effects of strong magnetic field.

7- Having an excess of ions in the depletion region makes up for the gradient of density pointing from filamentary rings towards the depletion regions and therefore maintains the filamentary structure. If the electrons could have some effective diffusion across magnetic

field, they would move from the filamentary rings into the depletion region as both electric field and gradient of density are pushing them to these regions.

8- If the pressure is too high (more than the critical pressure), then the cross magnetic field diffusion coefficient of the electrons will be high to help electrons diffuse from the filamentary regions to the depletion regions. Also, the high number of collisions of the ions with the neutral atoms at high pressure, no longer helps them diffuse across the magnetic field but decreases the cross magnetic field mobility and diffusion coefficient of the ions as it was shown in figure 3.17. These two effects together interrupt the filamentary pattern formation in magnetized plasmas at pressure beyond critical pressure.

9- Moreover, if the vertical distance between the top and bottom electrodes is too long, then the electrons have enough time to diffuse across the magnetic field before the excess of the electrons could diffuse to the electrodes parallel to the magnetic field. In this case the diffusion of plasma will be ambipolar in cross-field direction. This explains why the filamentary patterns do not form in a long column of plasma.

10- In presence of the magnetic field, the random walk diffusion of the ions, due to collisions, across the magnetic field happens at steps equal to the gyro-radius of the ions rather than ions mean-free-path [7]. Therefore, if the Debye length is smaller than the ions gyro-radius, the electric field gets shielded by the plasma over lengths smaller than the random walk steps and filamentary patterns do not form in the magnetized plasma. Based on this fact and the balance between density gradient and electric force on the ions at the filament-depletion boundary, the dependency of the width and center to center distance between the filaments on electron's Debye length and ion mean-free-path is justified.

11- Therefore, in a given time interval, the rate of the electron loss in the depletion regions is more than the filamentary rings. This loss occurs parallel to the magnetic field to the electrodes. As a result, the currents (and equivalently the horizontal electric field) in the electrodes should be pointing from the filamentary rings to the depletion regions. Since electrons move in opposite direction of the electric field, these currents prevent accumulation of the electron at the top and bottom of the depletion regions to guarantee an equipotential metallic surface. Figures 3.22 and 3.23 which show the electric field vector at the top electrode (perpendicular to the magnetic field lines) of an argon plasma chamber, confirm this assumption.

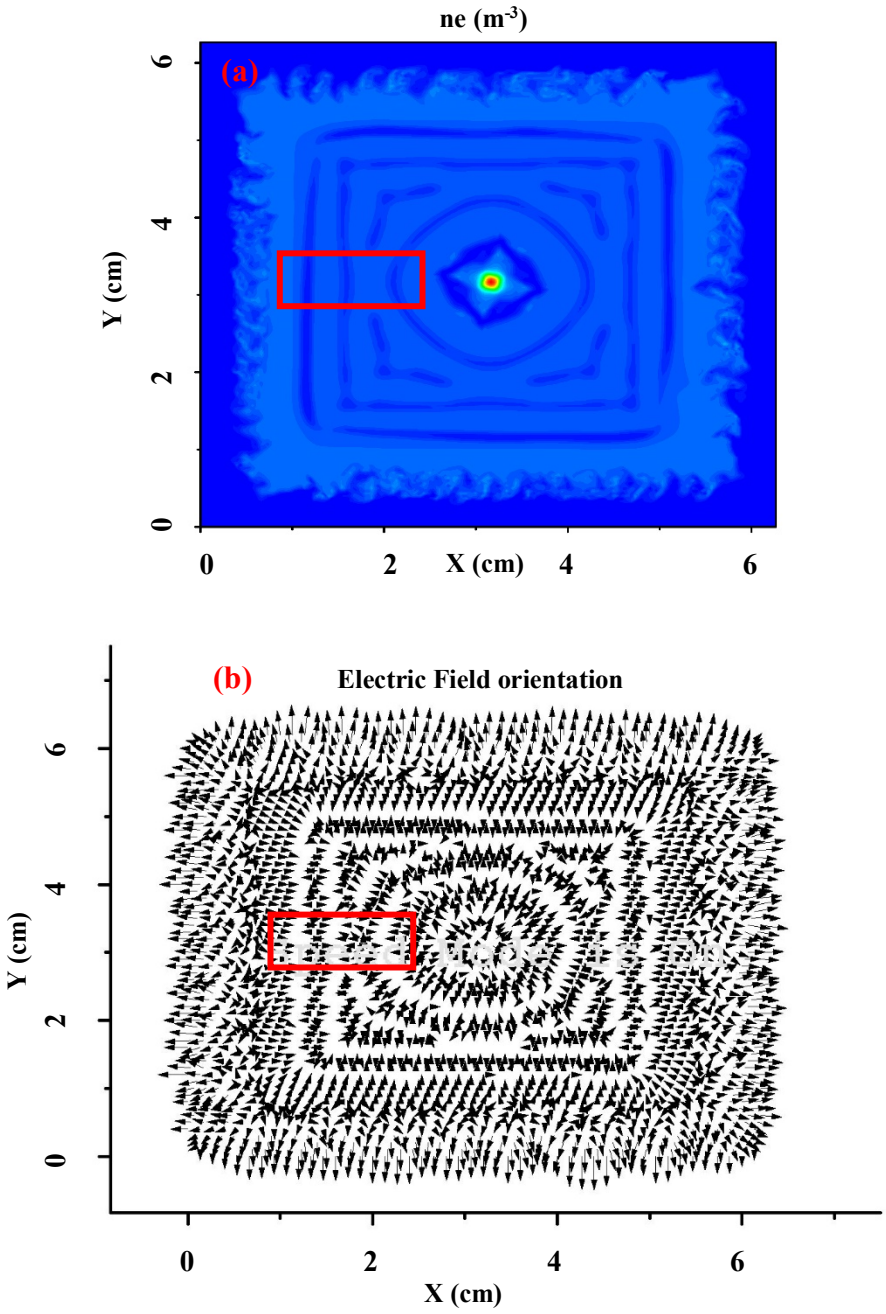

Figure 3.22: (a) X-Y cross section of electron density profile in the middle of an argon plasma chamber at pressure of 10 Pa exposed to 0.8 T magnetic field. Initial plasma density is uniform of the order $5.4\times10^{14}\ m^{-3}$ and electron and ion temperature are $T_e = 2.5\ eV$ and $T_i = 0.025\ eV$ respectively. (b) the electric field vector orientation at the top electrode (perpendicular to the magnetic field lines). Also, the X-Y regions of interest are indicated with red boxes which are displayed in more details in figure 3.23.

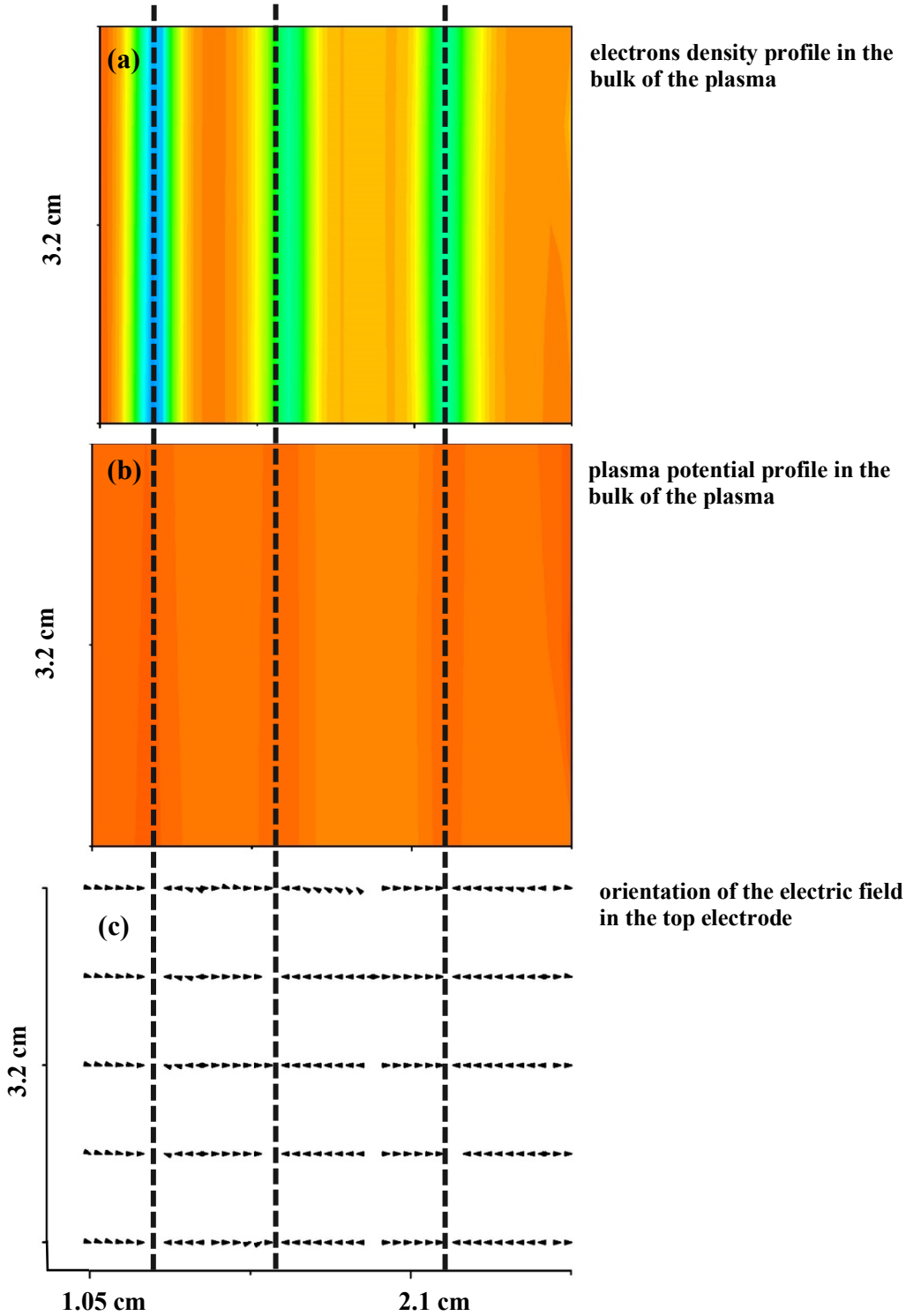

Figure 3.23: X-Y cross section of electron density profile (a), Plasma potential (b) in the middle of the argon plasma chamber, and the electric field vector orientation at the top electrode (c). All three plots are from the same X-Y region of interest indicated with red boxes in figure 3.22.

4 Gridding of Dust Particles in Magnetized Dusty Plasmas

In a magnetized dusty plasma experiment, gridding phenomenon, as referred to in this work, is defined as the organization of dust particles into "imposed, ordered structures" whose spatial patterns reflect the spatial ordering of a wire mesh placed in the bulk of the plasma [26]- [28]. The investigation on different aspects of filamentation phenomenon in the previous chapter helped us to gain an insight into the physics of gridding phenomenon. Through the simulation of filamentation phenomenon, we know how the imposed filamentation by a wire mesh can create a potential structure to trap the dust particles in magnetized dusty plasmas. Not only are the results of the simulation phenomenon going to be used in studying gridding phenomenon, but also, the 3D model used in the simulation of filamentation is slightly modified to be applied in the simulation of gridding phenomenon.

In this chapter, section 4.1 will introduce the model/geometry for the simulations of gridding phenomenon and presents a benchmarking simulation of the phenomenon. In section 4.2, the simulation results for gridding phenomenon under variation of different plasma parameters and mesh configurations will be presented. Finally, these results will be discussed in section 4.3.

4.1 Benchmarking Simulations For Gridding Phenomenon

The numerical model used in the simulation of the gridding phenomenon is similar to the one used for the simulation of the filamentation. The key difference between the two models is the presence of a grounded metal mesh added below the top electrode in the gridding model. In this model, the metal mesh breaks the symmetry of the plasma to form the gridding structure in the plasma and no density perturbation is needed. Figure 4.1 displays a schematic picture of the plasma

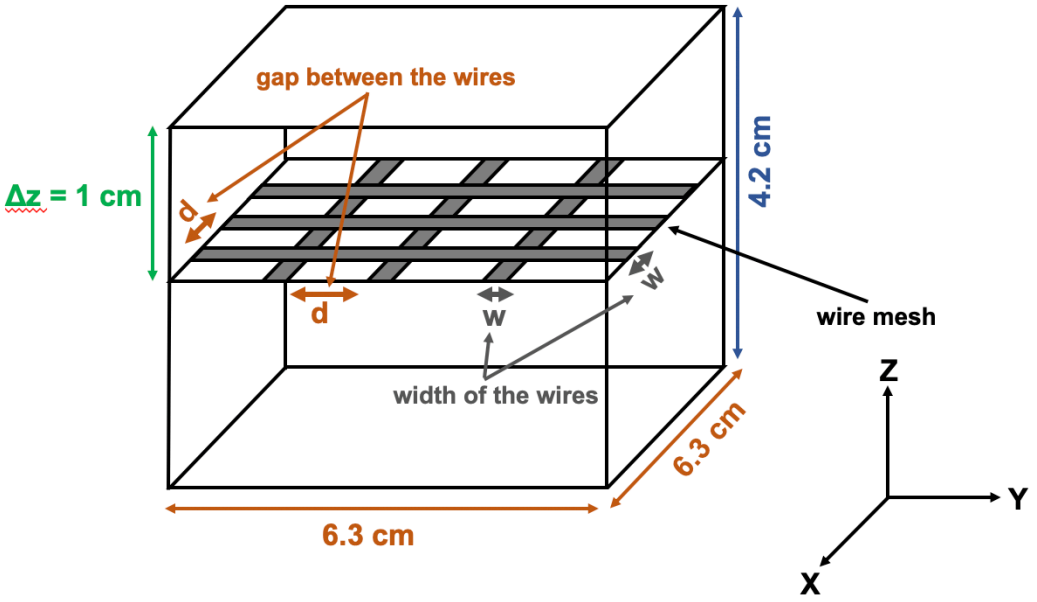

Figure 4.1: Schematic picture of the rectangular plasma chamber with a metal mesh placed below the top electrode as it is considered in the numerical simulations of gridding phenomenon. The picture is not drawn to scale.

chamber considered in the simulation of gridding phenomenon.

All of the walls of the plasma chamber as well as the wire mesh placed below the top electrode in the simulations are assumed to be grounded. In the gridding experiments a bias voltage is often applied to the metal mesh. However, the nature of the gridding phenomenon does not significantly depend on the bias voltage, and despite some slight differences, the experimental results with unbiased mesh are in agreement with the results with biased mesh. Also, since the energy equation is not included in our model, applying a bias voltage to the mesh would cause unnecessary technical difficulties.

The plasma gas is assumed to be argon with uniform electron/ion densities throughout the plasma chamber ($n_e = n_i = 5.0 \times 10^{14}\, m^{-3}$). The constant temperatures of the electrons and ions are set to be $2.5\ eV$ and $0.025\ eV$ respectively. Through different simulations it was observed that the filamentary patterns due to the presence of the metal mesh appear in the magnetized plasma at time scale of about $20\text{-}40\ \mu s$ which was also confirmed previously in the simulations of filamentation phenomenon. Therefore, the numerical data shown, represent 25 μs simulation of the plasma. The time step in the simulations is assumed to be $\Delta t = 1\times10^{-11}\, s$, spatial step size in Z direction to be $h_z = 6\times10^{-4}\, m$, and in X /Y directions to be $h_x = 3.5\times10^{-4}\, m$.

Before trying to simulate gridding phenomenon, it is useful to check the performance of the model in the absence of magnetic field. A metal mesh with wires of width $w = 1.4\ mm$ is considered in the bulk of the plasma at $\Delta z = 1$ cm below the top electrode and the gap between the wires of the mesh is $d = 8\ mm$ (see figure 4.1). The neutral gas pressure is set to be $P = 12\ Pa$. Figure 4.2 displays the top view (X-Y cross section)) of the electron density profile and the plasma potential profile obtained from the simulation of the unmagnetized plasma in presence of the metal mesh. The ion density profile is similar to that of the electrons and is not shown here.

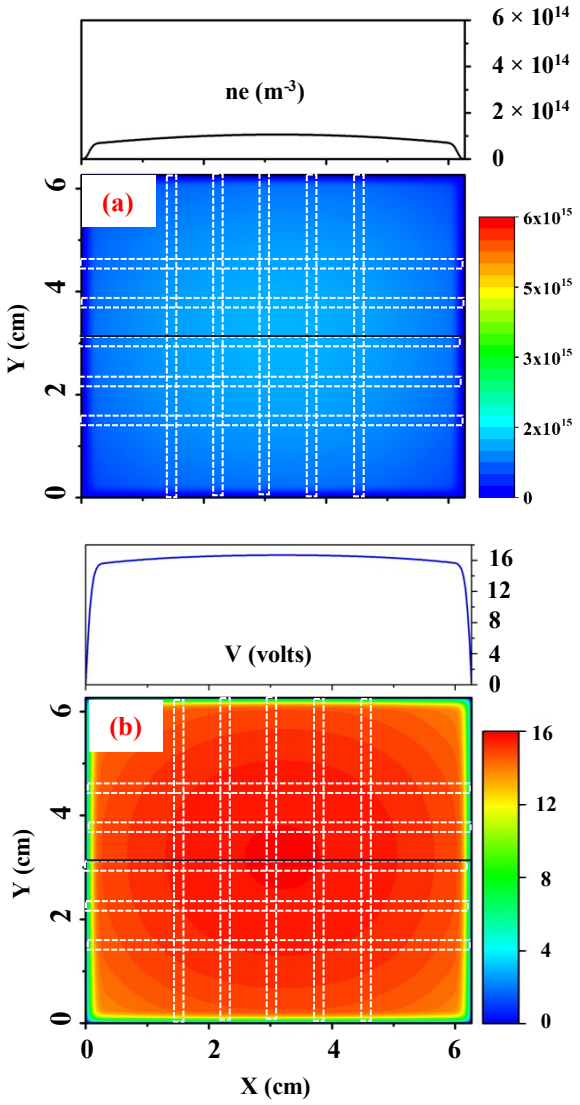

Figure 4.2: X-Y cross section of: (a) electron density profile, and (b) plasma potential profile, in an unmagnetized plasma in presence of a metal mesh with wires of width *w = 1.4 mm*. The white dashed lines indicate the location of the mesh wires. The solid black line indicates where the top plots have been taken from. Initial plasma density is uniform of the order $5\times10^{14}\ m^{-3}$, electron and ion temperature are $T_e = 2.5\ eV$ and $T_i = 0.025\ eV$ respectively, and $P = 12$ Pa. In the absence of magnetic field, no patterns are forming in the plasma in presence of the metal mesh.

The simulation is terminated at $t = 30\ \mu s$ and the cross-section profiles are taken from the middle of the plasma chamber at $Z = 2.1\ cm$. It can be seen in these figures that, in the absence of magnetic field, the metal mesh has not affected the plasma at all. Since similar to the chamber walls, the metal mesh is assumed to be grounded, the electrons/ions simply diffuse to the walls and to the metal mesh and recombine there. Consequently, no pattern is forming in the unmagnetized plasma in presence of the metal mesh.

In order to evaluate the performance of the gridding model in presence of magnetic field, $1.0\ T$ magnetic field is applied to the plasma in negative Z direction. The top-view of the electron density profile and plasma potential and the side-view of the electron density profile for this simulation are displayed in figure 4.3. The side-view of the electron density profile is presented only for the region beneath the metal mesh and away from the sidewalls of the plasma chamber. The spatial profile of the ion density is the same as electron density profile and therefore not shown here. It can be seen in this figure that the presence of the metal mesh has imposed filamentary patterns in the electron density and plasma potential profiles parallel to the magnetic field. The same as the graphs presented for filamentation phenomenon, each gridding phenomenon graph is also labeled with a set of three length values; ($r_i\ (mm)$, $\lambda_i\ (mm)$, $\lambda_{De}\ (mm)$), which represent ion gyro-radius, ion mean-free-path and electron Debye length respectively.

In the presence of the strong magnetic field, the diffusion of electrons and ions perpendicular to the magnetic field is reduced and they mostly diffuse parallel to the magnetic field to the mesh and to the electrodes. Consequently, depletion regions form right below the wires of the mesh which will be called primary depletion regions. Additional depletion regions appear

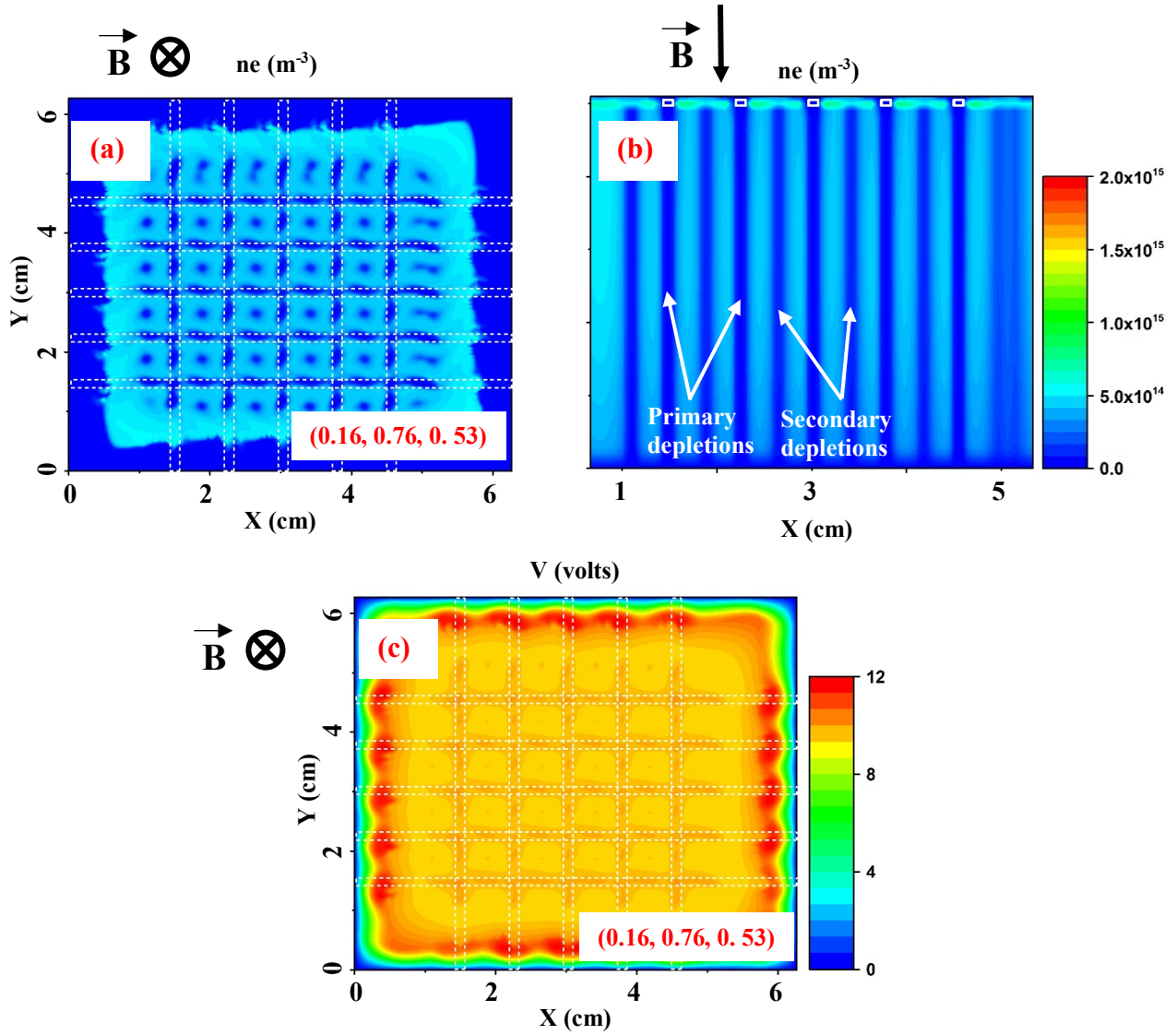

Figure 4.3: (a) X-Y and (b) X-Z cross section of the electron density profile, and (c) X-Y cross section of the plasma potential profile of an argon plasma at pressure of *12 Pa* exposed to *B = 1.0 T* magnetic field. Initial plasma density is $5\times10^{14}\ m^{-3}$ and electron and ion temperature are $T_e = 2.5\ eV$ and $T_i = 0.025\ eV$ respectively. A metal mesh with wires of width *w = 1.4 mm* is placed $\Delta z = 1\ cm$ below the top electrode. The X-Y profile is taken at *Z = 1.5* cm and the X-Z profile is taken at *Y = 3 cm*. The X-Z cross section is only displayed from the bottom electrode to the mesh in Z direction and away from the sheath regions in X direction. The locations of the mesh wires are indicated using white lines. The filamentary patterns imposed by the metal mesh can be seen in both electron density and plasma potential profiles and are extended in the bulk of the plasma parallel to the magnetic field.

halfway between the primary depletion regions in the gap between the wires, which will be called secondary depletion regions (see figure 4.3 (b)). The secondary depletion regions did not appear in plasmas where the gap between the mesh wires was less than $d = 3\ mm$. Because of the very fine structure of the narrow meshes which is comparable to the size of the most probes, the formation of the secondary depletion regions has not yet been experimentally investigated.

Also, it is clear in figure 4.3.c that similar to the filamentation phenomenon, the plasma potential in the depletion regions is higher than the neighboring points. This plasma potential structure that is extended into the bulk of the plasma parallel to the magnetic field may be responsible for the observation of gridding phenomenon in dusty plasma experiments in presence of a metal mesh.

4.2 Simulation Results

The simulations of gridding phenomenon (without added dust particles) will show how the presence of a metal mesh imposes filamentary structures to the plasma and in return, these filamentary structures impose a potential structure that extends along the external magnetic field in the plasma. This potential structure is responsible for trapping the dust particles in a dusty plasma experiment and causes the phenomenon that is called gridding of the dust particles. Also, in addition to varying pressure, electron/ion density, and magnetic field, the gridding phenomenon is studied using three different metal meshes with the wires of width $w = 1.4\ mm$, $2.8\ mm$ and $5.2\ mm$.

4.2.1 Variation of Gridding Phenomenon with Pressure

To investigate the effect of varying pressure on imposed filamentation by a metal mesh (gridding phenomenon), the simulation for the mesh with narrow wires of width $w = 1.4\ mm$, and gap of $d = 8\ mm$, was repeated for pressures of *4 Pa*, *6 Pa*, *9 pa*, *18 Pa*, and *30 Pa*. Figure 4.4 displays the electron density profile for these simulations.

It can be seen in figure 4.4 that, by decreasing pressure (increasing the ion mean-free-path), the secondary depletion regions do not form in the plasma and at very low pressures even the imposed patterns by the mesh, get disturbed. Similar to filamentation in chapter 3, the evolution of imposed filamentation also depends on the cross magnetic field diffusion of the ions from beneath the wires (depletion regions) to the gap regions. The simulation results presented here are believed to arise from a similar physical mechanism as discussed in Sec. 3.3.

The cross magnetic field diffusion of the ions increases with pressure as long as the pressure is below a critical pressure (see figure 3.18). If the gap between the wires is large enough compared to the ion mean-free-path and electron Debye length, the cross magnetic field diffusion of the ions from beneath the mesh wires to the gap between the wires, not only guarantees the formation of the imposed filamentation (gridding phenomenon), but also can lead to the emergence of secondary depletion regions in the gap between the mesh wires. By decreasing the neutral pressure, the cross magnetic field diffusion of the ions also decreases, resulting in elimination of the secondary depletion regions (at $P = 9\ Pa$ for the given plasma parameters in the presented simulations), and at even lower pressures (*4 Pa* and *6 Pa* in the presented simulations) disturbing the formation of the imposed filamentation in presence of the metal mesh.

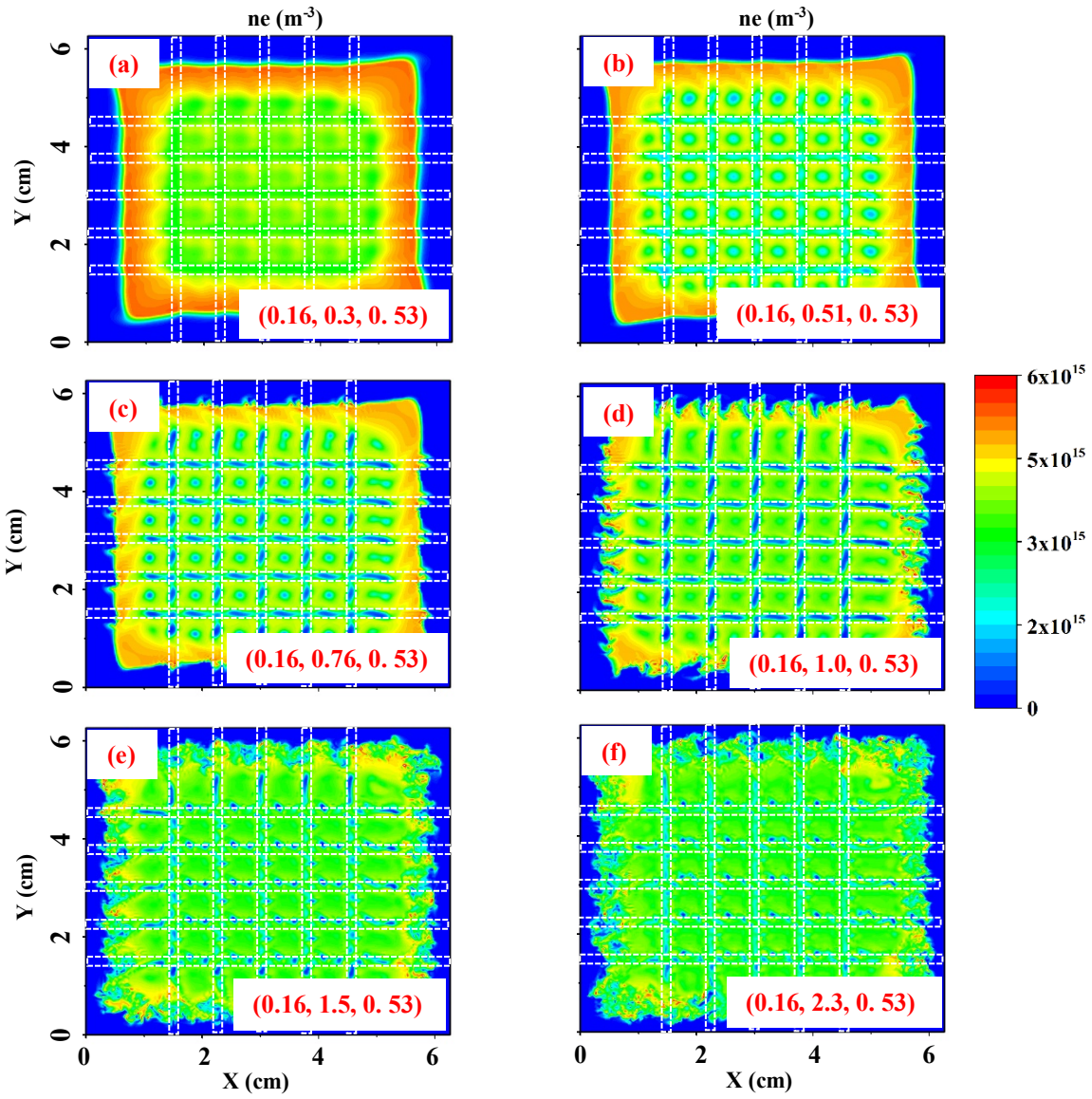

Figure 4.4: Electron density profile in a magnetized argon plasma in presence of a metal mesh placed below the top electrode. The width of the mesh wires is *w = 1.4* mm and the gap between these wires is *d = 8 mm*. Initial plasma density is uniform of the order $5\times10^{14}\ m^{-3}$, electron and ion temperature are T_e = *2.5 eV* and T_i = *0.025 eV* respectively, and *B = 1.0 T*. The neural pressure is different for different graphs, a) 30 Pa, b) 18 Pa, c) 12 Pa, d) 9 Pa, e) 6 Pa, f) 4 Pa. By decreasing pressure (increasing ion mean-free-path), the secondary depletion regions don't form in the plasma and at very low pressures even the imposed pattern by the mesh gets disturbed. The white dashed lines indicate the location of the mesh wires.

4.2.2 Variation of Gridding Phenomenon with Background Plasma Density

Variation of plasma density in the simulations is equivalent to the variation of power deposition into the plasma in the experiments. Figure 4.5 displays the variation of the imposed filamentation with background plasma density (electron's Debye length). The metal mesh considered in these simulations has again wires of width $w = 1.4$ mm with gaps of $d = 8$ *mm* between them. Also, the neutral gas pressure is assumed to be *12 Pa*. It is noticed in this figure that, by increasing background plasma density (decreasing electron Debye length), additional filamentary patterns form in the gap between the mesh wires.

In the simulations of the filamentation phenomenon, the width of the filamentary patterns and the center-to-center distance between them is controlled by different plasma parameters including plasma density and neutral gas pressure. In these simulations, the plasma density and neutral gas pressure also play a similar role. These results first show the presence of a higher plasma potential beneath the mesh wires (see figure 4.3.c) generates an outward electric field to repel a fraction of the extra ions. These repelled ions then remain at a distance few Debye length away, where there is a balance between the electric force and density gradient on the ions. Since ions are repelled into the gaps from the depletion regions beneath two neighboring wires, when the gap between the mesh wires is more than a couple of Debye lengths, it enables the formation of secondary filamentary structures in the gap between the wires. This is consistent with the observation that when the Debye length is *1.2 mm* ($n_e = 1.0 \times 10^{14}\, m^{-3}$) in figure 4.5.a the secondary filaments are not forming in the gap between the wires while as the Debye length gets smaller in the next figures, secondary filamentary structures appear in the gap regions.

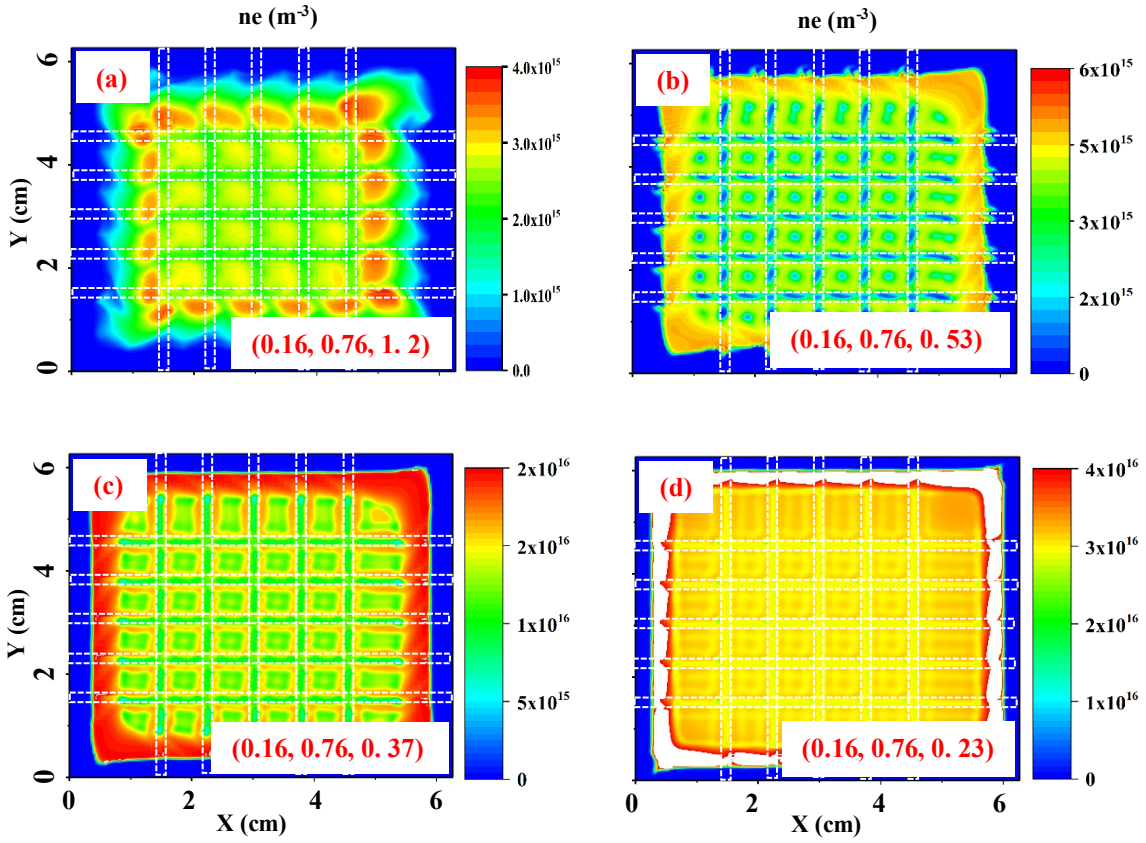

Figure 4.5: X-Y cross section of Electron density profile in a magnetized argon plasma in presence of a metal mesh placed below the top electrode. Electron and ion temperature are $T_e = 2.5\ eV$ and $T_i = 0.025\ eV$ respectively, $P = 12$ Pa and $B = 1.0\ T$. The width of the mesh wires is $w = 1.4$ mm and the gap between these wires is $d = 8\ mm$. The background plasma density is different for different graphs, a) 1.0 $\times 10^{14}\ m^{-3}$, b) 5.0 $\times 10^{14}\ m^{-3}$, c) 1.0 $\times 10^{15}\ m^{-3}$, d) 2.5 $\times 10^{15}\ m^{-3}$. By increasing background plasma density (decreasing electron Debye length), additional filamentary pattern form in the gap between the mesh wires. The white dashed lines indicate the location of the mesh wires.

4.2.3 Variation of Gridding Phenomenon with the Applied Magnetic Field

Variation of the magnetic field can affect the cross magnetic field diffusion of the electrons and ions. The variation of the imposed filamentation by a metal mesh in an argon plasma with the applied magnetic fields is displayed in figure 4.6. The metal mesh considered in these simulations has wires of width $w = 1.4$ mm with a gap of $d = 8$ *mm* between them, neutral pressure is assumed to be *12 Pa* and the background plasma density is considered to be 5.0 $\times 10^{14}\, m^{-3}$. It can be seen in this figure that, by increasing the applied magnetic field, the imposed filamentation gets more organized with sharp edges, and secondary filamentary structure do not appear in the plasma. This is because by increasing the magnetic field applied to the plasma, the ions gyro-radius decreases. As mentioned before, the random walk diffusion of the ions due to collisions across the magnetic field lines happens at steps equal to the gyro-radius of the ions rather than ions mean-free-path [7]. Equivalently, in highly magnetized plasmas the cross magnetic field mobility and diffusion coefficient of the ions decreases (see equations 3.13 and 3.14). Therefore, as the cross magnetic field diffusion of the ions is interrupted at higher magnetic fields, the formation of secondary depletion regions is disturbed and even the primary depletion regions would need more time to appear in the plasma.

4.2.4 Variation of Gridding Phenomenon with the Width of Mesh Wires

In order to further investigate the gridding phenomenon, the simulations at P = 12 Pa and plasma density of 5.0 $\times 10^{14}\, m^{-3}$ were repeated using two other meshes with wires of width w = *2.8 mm* and $w = 5.2$ *mm.* The gap between the mesh wires was still considered to be $d = 8mm$. The electron density profile and the plasma potential for these two cases are presented in figures 4.7 and 4.8 respectively. It is clear from these figures that by increasing the width of the mesh wires

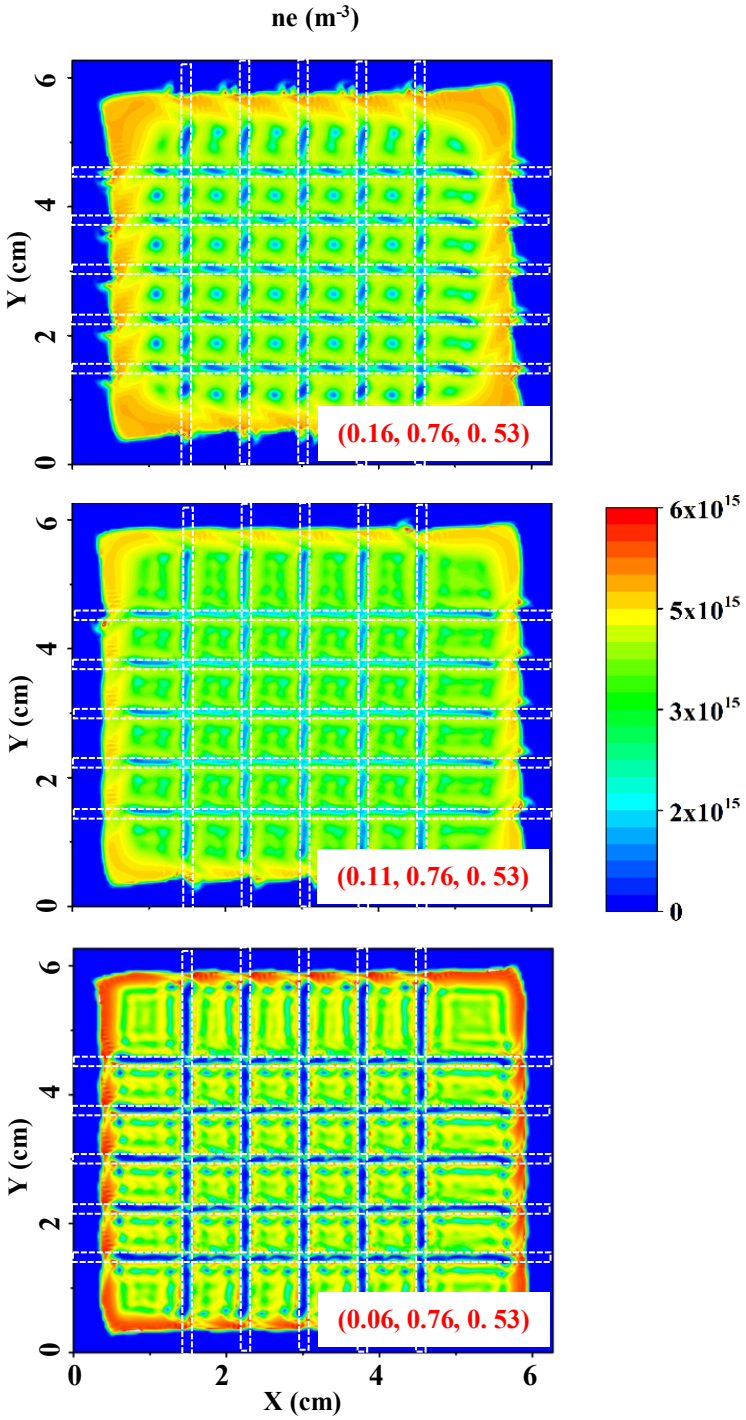

Figure 4.6: Electron density profile in a magnetized argon plasma in presence of metal mesh placed below the top electrode. The width of the mesh wires is *w = 1.4* mm and the gap between these wires is *d = 8 mm*. The plasma is exposed to different magnetic fields, a) 1.0 T, b) 1.5 T, c) 2.5 *T*. The white dashed lines indicate the location of the mesh wires. By increasing the applied magnetic field, the imposed filamentation gets more organized with sharp edges and secondary filamentary structure do not appear in the plasma.

(w), the density and potential profiles transition from one depletion region to two depletion regions beneath the wires of the mesh. Also, these two depletion regions tend to form at the edges of the wires compared to the one depletion region for the narrow meshes that would appear right below the wires of the mesh (see figure 4.2). This difference in the location of the depletion regions, also shifts the regions with higher plasma potential to the locations corresponding to the edges of the wide mesh wires. To display this difference between the imposed potential profile by the narrow and wide meshes, the plasma potentials in X-Z plane for meshes with $w = 1.4\ mm$ and $w = 5.2\ mm$ are shown in figure 4.9. It can be seen in this figure that for the wide mesh ($w = 5.2\ mm$), the regions at higher plasma potential form beneath the edges of the wires while for the narrow mesh ($w = 1.4\ mm$), there is only one region at higher potential right below its wires. These results are consistent with the observations presented in figure 1.5 that in magnetized dusty plasma experiment with the "waffle" electrode the dust particles were trapped beneath the edges of the mesh wires.

4.3 Discussion on the Simulations of Gridding Phenomenon

One of the most important results from the simulation of filamentation phenomenon was the fact that electron and ion densities differ in the filamentary and depletion regions. As it is displayed in figure 4.10.a, this observation is also confirmed in the simulation of gridding phenomenon. The simulation parameters in Figure 4.10 are the same as figure 4.3 that is, the width of the mesh wires *is* $w = 1.4\ mm$ at a distance of $d = 8\ mm$ from each other, background plasma density is $5\times10^{14}\ m^{-3}$, electron and ion temperature are $T_e = 2.5\ eV$ and $T_i = 0.025\ eV$ respectively, neutral pressure is $P = 12$ Pa and the applied magnetic field is $B = 1.0\ T$.

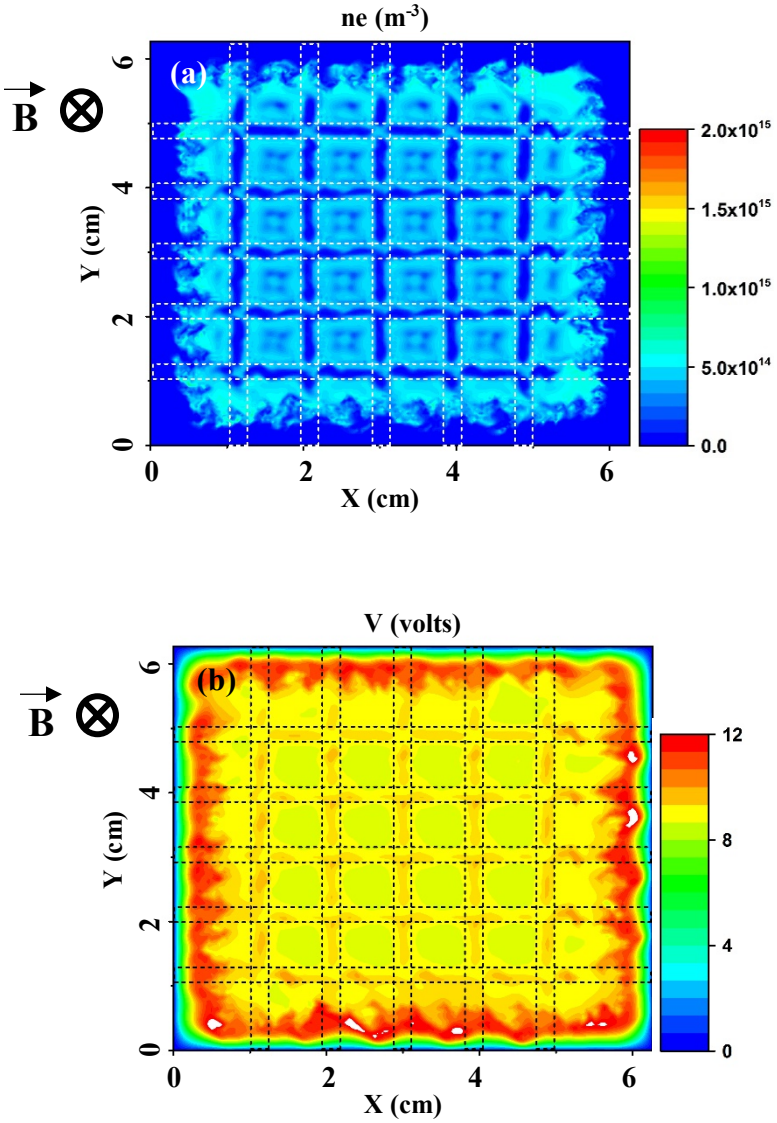

Figure 4.7: X-Y cross sections of the electron density profile (a) and plasma potential (b) of an argon plasma at pressure of *12 Pa* exposed to *1.0 T* magnetic field. A metal mesh with wires of width *w = 2.8 mm* is placed *Δz = 1 cm* below the top electrode. The profiles are taken at *Z = 1.5* cm. The white spots in the potential graph refer to points which are out of bound (V > 12 volts). The position of the metal mesh is indicated using dashed lines.

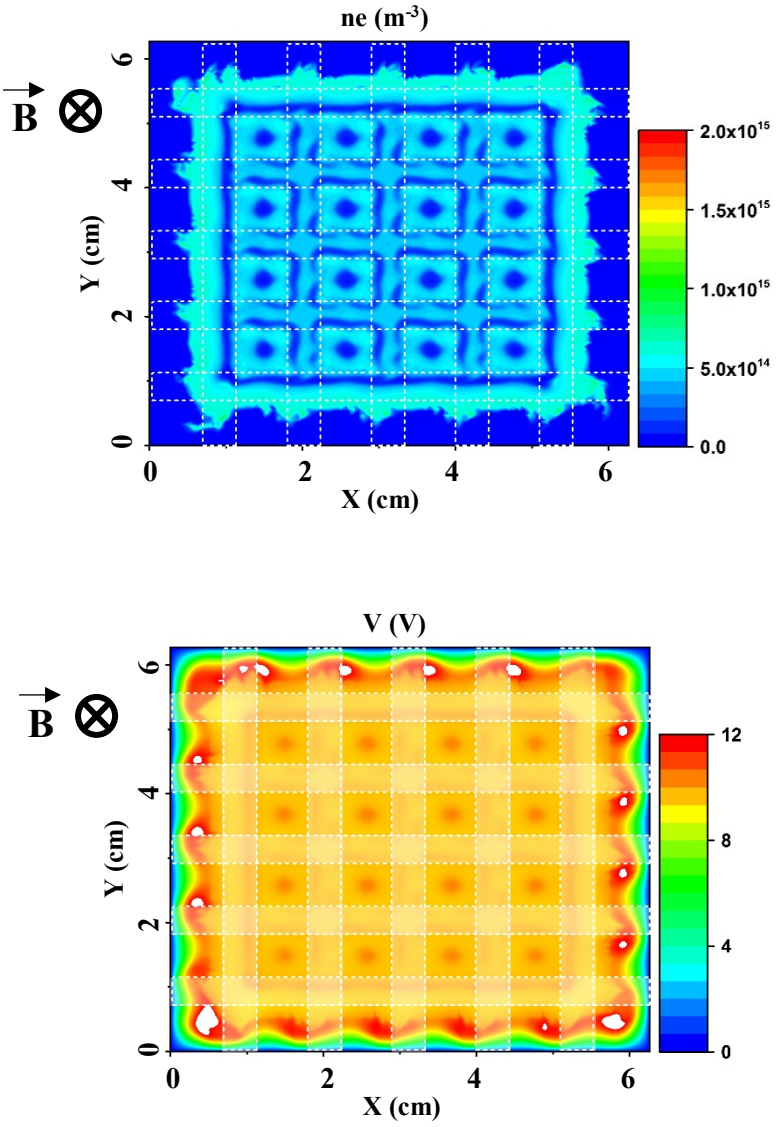

Figure 4.8: X-Y cross sections of the electron density profile (a) and plasma potential (b) of an argon plasma at pressure of *12 Pa* exposed to *1.0 T* magnetic field. A metal mesh with wires of width *w = 5.2 mm* is placed *Δz = 1 cm* below the top electrode. The profiles are taken at *Z = 1.5* cm. The white spots in the potential graph refer to points which are out of bound (V > 12 volts). The position of the metal mesh is indicated using white masks on the graph.

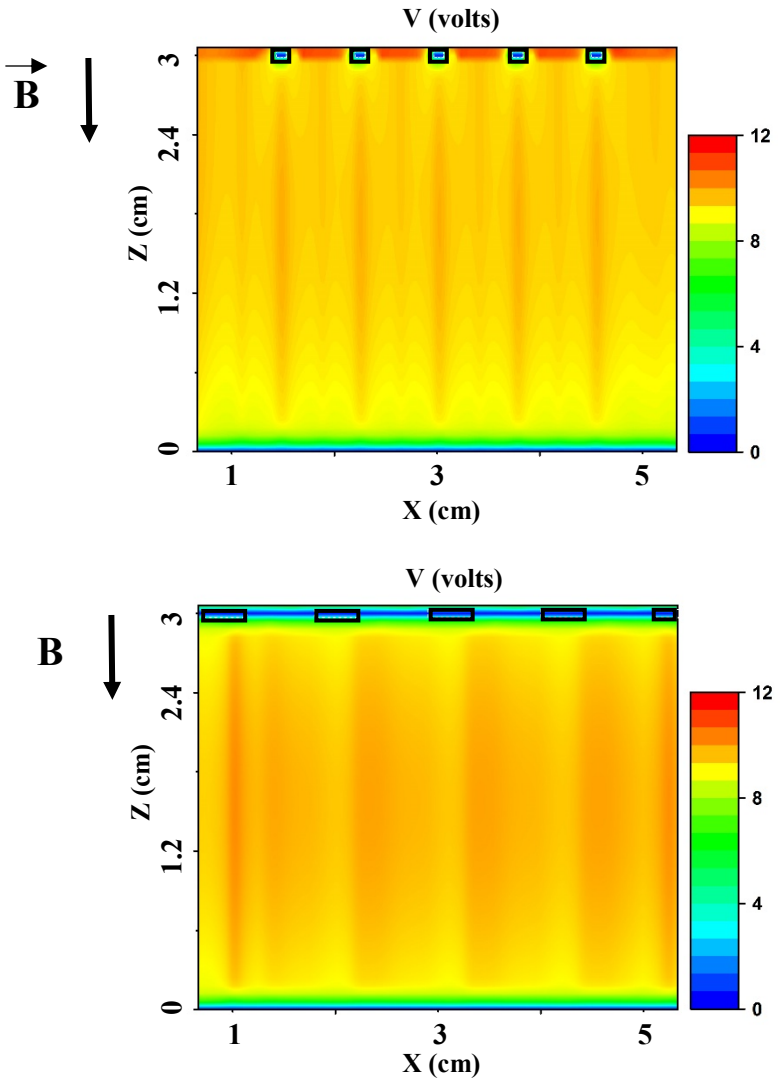

Figure 4.9: X-Z cross section of the plasma potential profile of an argon plasma with initial density of $5\times10^{14}\ m^{-3}$ at pressure of *12 Pa* exposed to *1.0 T* magnetic field. (a) A metal mesh with wires of width *1.4 mm* is placed *1 cm* below the top electrode. (b) A metal mesh with wires of width *5.2 mm* is placed *1 cm* below the top electrode. The X-Z profile is taken at $Y = 3$ *cm* and is only displayed from the bottom electrode to the mesh in Z direction and away from the sheath region in X direction. It is obvious from these figures that the locations of the higher plasma potential to trap the dust particles are shifted to the edge of the wires for the wide mesh ($w = 5.2$ *mm*). The locations of the mesh wires are indicated using small black rectangles.

Similar to the filamentation phenomenon, in the imposed patterns by the metal mesh in magnetized plasmas, the density of ions is more than the density of the electrons in depletion regions (see figure 4.10.a). To explain this density imbalance, one has to notice that, in high magnetic field regime ($B \geq 1.0\ T$), both electrons and to some extent ions are magnetized and their diffusions across the magnetic field are reduced. Also, due to the much larger mass of the ions, their diffusion rate parallel to magnetic field is much smaller than that of the electrons. Therefore, electrons leave the regions beneath the mesh wires parallel to the magnetic field more than the heavy ions.

It has been already mentioned that, the larger mass of the ions enables them to have a limited diffusion across the magnetic field [7]. The same as what was observed for the filamentation phenomenon, the ions beneath the mesh wires that are left behind by the electrons, partially diffuse across the magnetic field to the gaps between the mesh wires. The repelled ions to the gap regions, decrease the diffusion of the electrons (parallel to the magnetic field) at the gap, resulting in an enhanced plasma density in the gap regions (see figure 4.10.a).

The outcome of this process is an imposed filamentary pattern similar to the spatial structure of the wire mesh. Due to the difference between electron and ion densities in the filamentary and depletion region of this imposed patterns, the plasma potential profile is also following the spatial structure of the metal mesh as depicted in figure 4.10.b. Despite the fact that we are not exactly simulating the experimental set up, the results and the magnitude of the plasma potential are comparable to the observations in previous experiments performed using a narrow mesh with $w \leq 1mm$ [27] [28].

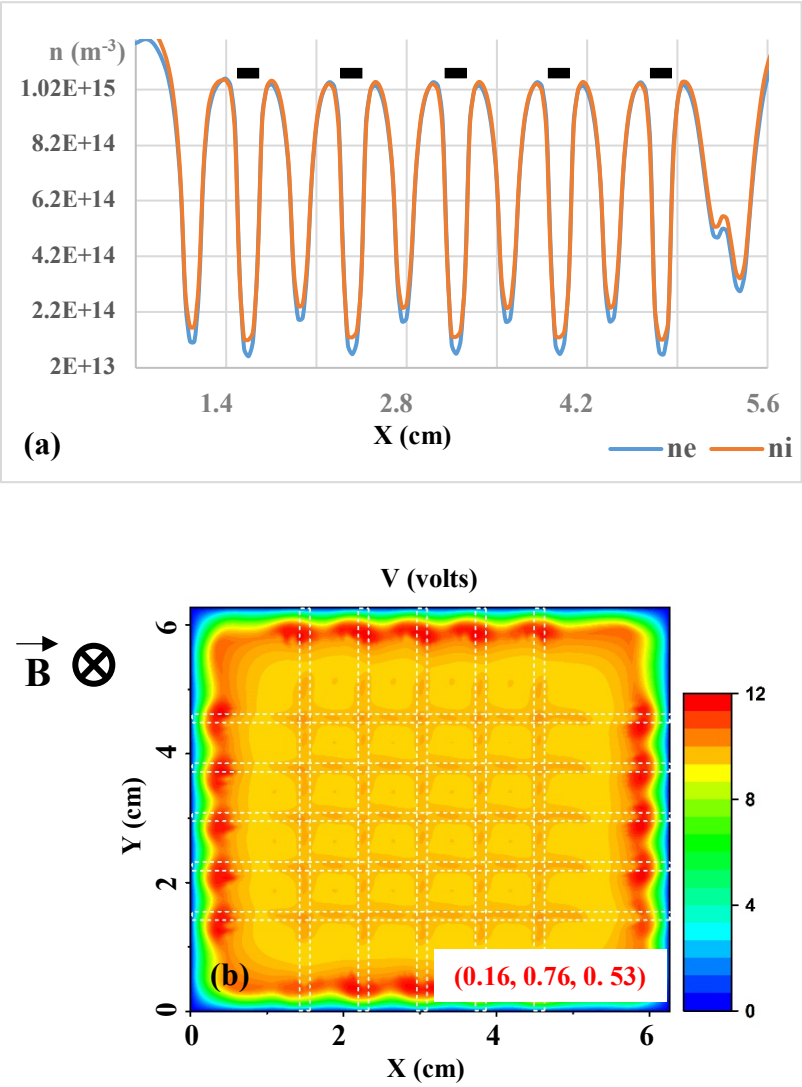

Figure 4.10: a) Electron and ion densities along X axis at *Y = 3* cm and *Z = 1.5* cm which shows a difference in electron and ion densities especially in the depletion regions (due to the presence of the metal mesh). The locations of the mesh wires with width *w = 1.4 mm* are indicated using white dashed lines and small black boxes. b) The plasma potential profile in X-Y plane as a result of this density difference. Initial plasma density is uniform of the order $5\times10^{14}\ m^{-3}$, electron and ion temperature are $T_e = 2.5\ eV$ and $T_i = 0.025\ eV$ respectively, $P = 12$ Pa and $B = 1.0\ T$. This potential profile is extended along the magnetic field in Z direction.

The mechanism that maintains the imposed filamentary structure in gridding phenomenon is shown to arise from the same physical processes as the filamentation as described in chapter 3. Similar to the observations in the filamentation phenomenon, the balance between the force from the electric field due to the excess of the ions in the depletion regions (see figure 4.11.a) and the gradient of density from the filamentary to depletion regions maintains the imposed filamentary pattern. Also, the electrons are strongly magnetized and the density imbalance between electrons and ions beneath the wires cannot be compensated for by electrons diffusion from the neighboring points as it would be expected in an un-magnetized plasma.

Figure 4.11 displays the X-Y cross section profile of the X element of the electric field (E_x) halfway between the metal mesh and the bottom electrode and the X-Z cross section profile of Z element of the electric field (E_z) beneath the metal mesh. Due to symmetry of the model, the plot of E_y in X-Y plane would be the same as the E_x profile only at the location of horizontal mesh wire along X axis. It is clear that the relatively higher plasma potential beneath the mesh wires creates electric fields pointing away from the depletion regions. The horizontal elements of the electric field not only are important in maintaining the imposed filamentary pattern but also, in a magnetized dusty plasma, these horizontal electric fields would push negatively charge dust particles to regions beneath mesh wires. Figure 4.11.b shows the variation of E_z along Z axis and the white solid line schematically displays where a layer of silica dust particles ($\rho = 2.65\ gr/cm^3$) would be levitated above the bottom electrode due to the balance between the upward electric force and the downward gravity on these particles. These two effects together are responsible for trapping the dust particles in the imposed patterns above the bottom electrode.

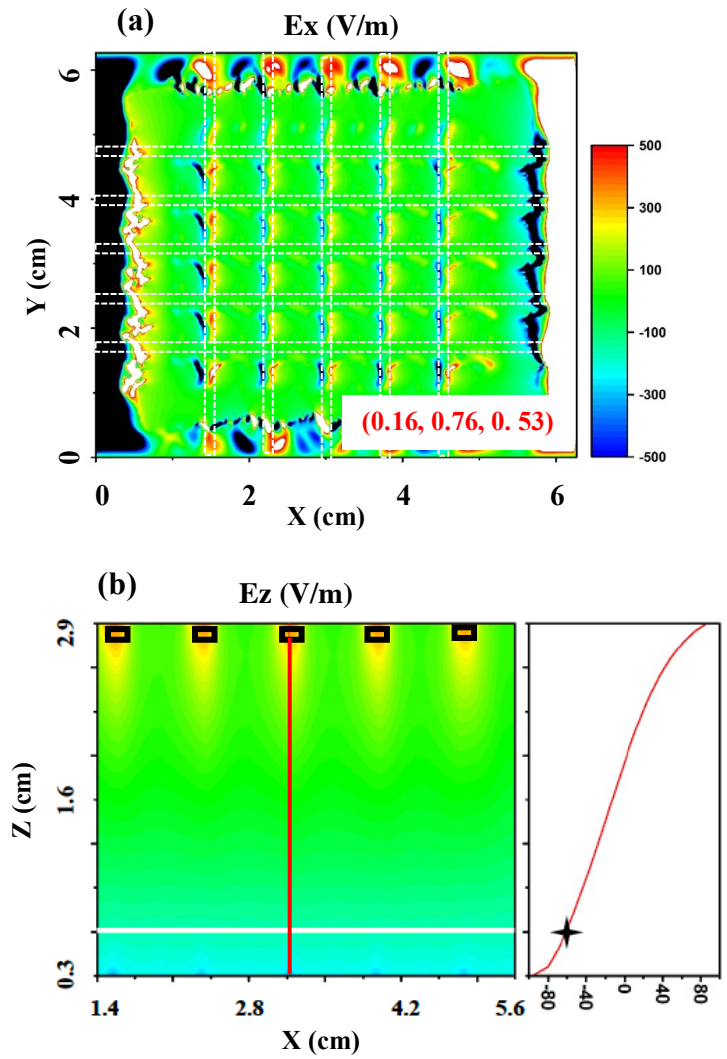

Figure 4.11: X-Y cross section profile of the X element of the electric field (E_x) halfway between the metal mesh and the bottom electrode and the X-Z cross section profile of Z element of the electric field (E_z) beneath the metal mesh wires. The locations of the mesh wires with width *w = 1.4 mm* are indicated using white dashed lines and small black boxes. Initial plasma density is uniform of the order 5×10^{14} m^{-3}, electron and ion temperature are $T_e = 2.5$ *eV* and $T_i = 0.025$ *eV* respectively, *P = 12* Pa and *B = 1.0 T*. In (a), the relatively higher plasma potential beneath the mesh wires creates horizontal electric fields pointing away from the depletion regions. The white solid line in (b) schematically displays where a layer of silica dust particles ($\rho = 2.65 \frac{gr}{cm^3}$, radius of 1 μm and "1000 e" charge) would be levitated above the bottom electrode due to the balance between the upward electric force and the downward gravity on these particles.

If the ions could not diffuse at all across the magnetic field from beneath the wires to the gap regions, the excess of the ions beneath the mesh wires would decrease the diffusion of the electrons parallel to the magnetic field and interrupt the formation of the imposed patterns. Therefore, the cross magnetic field diffusion of the ions, plays an important role in the formation of imposed filamentary patterns. Also, it is already noticed that if enough space is considered between the mesh wires (few times the ions mean-free-path and electron Debye length), this process that leads to the formation of imposed patterns beneath the wires can propagate in the gap between the wires to create secondary depletion regions.

To further study the formation of secondary filaments in the magnetized plasma due to the presence of a metal mesh, a mesh with only 4 wires (2 in X and 2 in Y direction) with wires of width $w = 1.4\ mm$ are considered. The gap between the wires is $d = 2.24\ cm$, to provide enough space for the formation of possible secondary depletion regions. Figure 4.12 displays the X-Y cross section of the electron density profile for this simulation in the middle of the plasma chamber. The background plasma density is $5.0 \times 10^{14}\ m^{-3}$, and applied magnetic field is $1.0\ T$. The results are shown for pressures of 6.5 and 12 Pa. Since a big gap between the mesh wires is considered, additional filamentary pattern form in the gap. At lower pressure ($P = 6.5\ Pa$), the secondary patterns are narrower and closer to one another so, more secondary patterns have appeared in the gap. This is in agreement with the filamentation simulations at low pressure presented in figures 3.7 and 3.8.

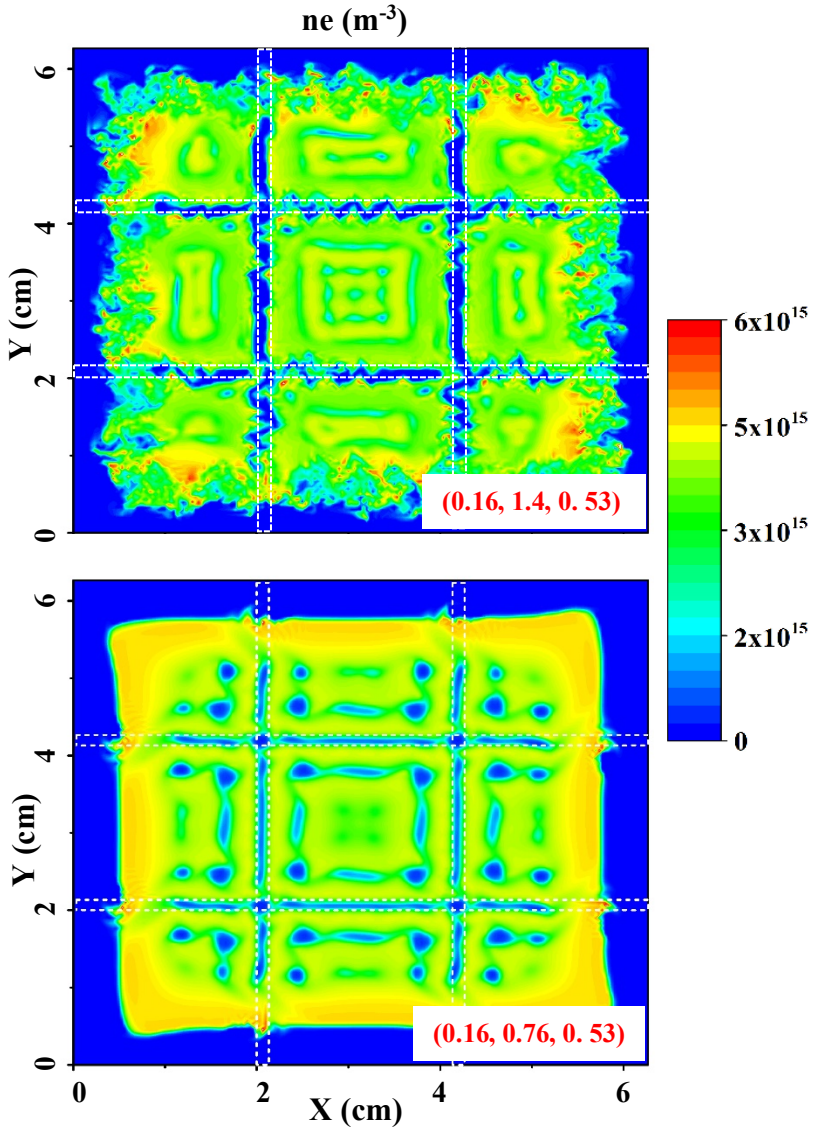

Figure 4.12: X-Y cross section of electron density profile in a magnetized argon plasma in presence of a metal mesh with only two wires, placed below the top electrode. The width of the mesh wires is $w = 1.4$ mm and the gap between these wires is $d = 2.24$ cm. The background plasma density is 5.0 $\times 10^{14}$ m^{-3}, applied magnetic field is 1.0 T, and electron and ion temperature are $T_e = 2.5$ eV and $T_i = 0.025$ eV respectively. a) $P = 6.5$ Pa, b) $P = 12$ Pa. Since a big gap between the mesh wires is considered, additional filamentary pattern form in the gap. At lower pressure in (a), the secondary patterns are narrower and closer to one another so, more secondary patterns have appeared in the gap. The white dashed lines indicate the location of the mesh wires.

Finally, based on the results from the simulations and the discussions on these results, the following explanation can be given for the appearance of double depletion regions beneath the edges of the "waffle" electrode placed in the magnetized plasma (see figure s1.5, 4.8, and 4.9). As discussed in the previous sections, at high magnetic fields, electrons and ions diffuse mostly parallel to the magnetic field, making the plasma in the regions beneath the mesh wires quasi-independent from the plasma in the regions beneath the gaps between the wires. Each of these regions will be slightly positively charged as the electrons diffuse faster than the ions to the mesh and the top/bottom walls. The boundary conditions being different beneath the wires and in the gap between the wires, the plasma losses and consequently, the density imbalance between ions and electrons ($n_i - n_e$), are different in these two regions. When the mesh wires are wide, in the areas beneath the central parts of the wide wires, the electric field is quasi-null. Indeed, the region directly beneath the edge of the wires is a transition region that connects the quasi-independent plasmas beneath the mesh and in the gap between the mesh wires. Since the plasma potential on the sides of these transition regions are different, there must be a strong electric field with an important X component. This electric field structure extends along the magnetic field and can be sufficient to trap the dust particles and lead to the trapping of dust particles beneath the edges of the wide mesh ("waffle" electrode).

5 Conclusion and Future Works

At the beginning of this work, the goal of studying filamentation and the formation of imposed patterns by placing a wire mesh in low-pressure low-temperature magnetized plasmas was introduced. This goal was achieved by looking into variation of these phenomena with different plasma parameters along with the geometry of the plasma chamber and the metal mesh. Through this work we now have a better understanding of the physical mechanism of these phenomena and in this chapter a summary of the work and possible future works on these topics will be presented.

In chapter 1 of this dissertation, an introduction to filamentation and gridding phenomena was given. These two phenomena were introduced, the early experimental and numerical works on them were discussed, and the similarities between these phenomena were pointed out. Both phenomena highly depend on the magnetic field and neutral gas pressure, mostly appear in plasmas/dusty plasmas that are exposed to strong magnetic fields ($B \geq 1.0\ T$), and they both are controlled by the ions dynamics. Also, these two phenomena can occur simultaneously in the plasma and if the dust particles number density is not too high, the presence of the dust particles does not significantly affect the filamentation. Finally, the motivation of the work was explained at the end of this chapter. This work was intended to investigate if filamentation and gridding phenomena arise from the same physical mechanism and suggest an explanation for appearance of these phenomena in low-pressure electric discharges that are exposed to strong magnetic field.

In chapter 2, the previous 2D simulations of filamentation are presented and their limitations which urge for a 3D model was discussed. These simulations were not able to capture the full physics of the phenomenon and could not distinguish between different filamentary structures by only providing the side view of these structures. The base set of equations that are considered in building the 3D fluid model were introduced in this chapter. These equations included plasma fluid

equations (excluding energy balance equation) solved along with the Poisson's equation. Moreover, different numerical methods that are used in discretizing and solving these equations were explained in detail. The last section of chapter 2 introduced the computational space of the model and the algorithm for solving the base equations in the model. In order to simplify the model a rectangular plasma chamber with metal walls was considered which is discretized using a multi-mesh configuration.

In the next chapter, filamentation and pattern formation in magnetized plasmas was investigated. A set of benchmarking simulations was presented to check the performance of the model in unperturbed, unmagnetized plasma and observe its capability in displaying different characteristics of the plasma such as electropositivity, and formation of sheath layers at the boundaries. It was then showed that by adding a perturbation to the magnetized plasma, the model could successfully produce filamentary patterns. A "filamentation parameter" was introduced to quantitively compare filamentation of the magnetized plasma under different conditions. Filamentation under variation of neutral gas pressure, plasma density, gas type, and the gap between the electrodes was studied. It was shown that by decreasing the neutral gas pressure and the gap between the electrodes and by increasing the background plasma density, the filamentation parameter of the plasma increases. It was also observed that when the electron Debye length and ion-neutral mean free path falls below the ions gyro-radius, filamentary patterns don't form in the plasma.

In the last section of chapter 3, the results from the simulations of filamentation phenomenon were discussed. The key finding of this work was to show that the densities of electrons and ions in the depletion regions of the filamentary patterns are different. It was shown that due to the effects of the strong magnetic field on the cross-field transport of the electrons and

ions, the density of ions is slightly higher than the electrons in the depletion regions. This excess of the ions creates an electric field that helps to maintain the filamentary structures. Based on the findings through the simulations, a theoretical model was suggested for filamentation that could successfully related the phenomenon to neutral gas pressure and plasma density.

Finally, in chapter 4, the formation of imposed filamentary patterns by placing a metal wire mesh in the bulk of magnetized plasmas was studied. After presenting benchmarking simulations, the gridding phenomenon was investigated under variation of different plasma parameters and the geometry of the wire mesh. It was observed that the physics behind the gridding phenomenon indeed is the same as for the filamentation. The presence of the metal mesh causes the formation of imposed filaments that reproduce the spatial structure of the mesh. In the filamentation phenomenon, the density of the ions is higher than electrons in the depletion regions. The result of this density discrepancy is a plasma potential profile that also copies the spatial structure of the wire mesh. This potential structure that is extended from the mesh to the sheath region above the bottom electrode can trap the dust particles in a magnetized dusty plasma experiment and generated gridding phenomenon.

It was also observed that the variation of imposed filamentary patterns with neutral gas pressure and background plasma density can be explained through the same mechanism used to study filamentation. Through the dependence of the imposed patterns on the width of the mesh wires, the simulations were able to reproduce the experimental observations made in the presence of the so called “waffle” electrode. If the width of the mesh wires is more than few Debye lengths and/or ion-neutral mean-free-path, the depletion region (and consequently the regions at higher plasma potential) from beneath the edges of the wide mesh wires. This would cause trapping of

the dust particles beneath the edges of the mesh as it was observed in the experiments with "waffle" electrode.

Another interesting observation in chapter 4 was the formation of secondary depletion regions. It was noticed that when the gap between the mesh wires was more than few Debye lengths secondary depletion regions could form in the gap. This observation and the formation of depletion region beneath the edges of a wide mesh were explained through the same process. Due to larger mass of the ions, they will be left behind beneath the mesh wires by the electrons. These ions can have a limited cross-field diffusion due to their large mass and partially diffuse to the gap between the wires which create a region of enhanced plasma density. If enough space is provided in the gap between the wires, these diffused ions can repel the neighboring ions in the gap and create a secondary depletion region. In the case of the wide wire mesh, only the regions beneath the edges of the wires can interact with the plasma in the gap and therefore the depletion regions can only form there.

In general, this work could reveal some crucial aspects of the physics of filamentation and gridding phenomena. This work was able to exhibit the similar underlying physics of these phenomena and proposed an explanation for them. Despite all the positive sides of this work, there is still room for developing the model and discover the last pieces of the physics of these phenomena. A very important step towards this goal would be including the energy equation in the model to see how filamentary patterns affect electron/ion temperatures. This would also allow for the calculation of the local collision frequencies in the simulations which seem to be playing an important role in the phenomena and thus give a more realistic picture of the organized patterns. Besides, secondary electron emission from the surface can be included to see their effects on the onset of filamentation and gridding phenomena.

In all the simulations presented here, the neutral atoms were assumed to be stationary, contributing to the model only through collisions with electrons and ions. As stated in chapter 3, the drift of the ions can be of the order of sound speed. Therefore, the neutral atoms could also gain a drift velocity due to momentum transfer with the ions. The motion of the neutral atoms can affect the collision frequencies and considering the neutral atoms as the third flowing species in the model could give a better insight into filamentation and gridding phenomena.

As mentioned before, all the walls of the plasma chamber in the 3D model were assumed to be metallic. To further investigate the effect of the electrodes on pattern formation in the plasma, the electrons and ions are allowed to accumulate in a few layers on and near the bottom electrode, instead of considering full absorption of the incoming electrons/ions at the electrode, as it was necessary for the metallic electrode. This is equivalent to having a layer of high-density dust particle near the bottom electrode or placing a dielectric plate on the bottom electrode. As it can be noted in figure 5.1, letting the charged particles accumulate at the bottom of the chamber and considering zero conductivity for those layers, results in preventing the filamentary patterns to form in the plasma. This simulation implies that the surface interaction of the electrons and ions with the electrodes play and important role in filamentation phenomenon in magnetized plasmas [55] [2].

The presented 3D fluid model could only consider two extreme cases of having electrode that are fully metallic or fully dielectric. With some more work the model can be enabled to allow for considering different material for the electrodes to investigate this aspect of filamentation more precisely. In this case, secondary electron emission from the surfaces can be also included. This effect must be also experimentally studied to see how the structure of the electrodes can affect the formation of filaments in the magnetized plasma.

The simulations of gridding phenomena can also inspire further numerical and experimental work. From the numerical point of view, adding dust particles to the model would be an ultimate goal. Through the presented work the predicted position of the dust particles was assumed to be at the location of highest plasma potential while the exact location of the dust particles would be also affected by neutral and ion drag forces. Although due to the small charge to mass ration of the dust particles their dynamics times scale would be very different from electrons and ions, this goal may be achieved through efficient parallel programing and application of supercomputers. Such a model would be useful not only in the simulation of gridding phenomenon but also in the investigation of many other aspects of magnetized and unmagnetized dusty plasmas.

Furthermore, the formation of secondary depletion regions was suggested in the simulation and it would be very interesting to study them in the experiments. This would require experiments at higher pressures and higher magnetic field as in the low-pressure regime, the random instabilities in the bulk of the plasma may result in the ordinary depletion region and interfere with the formation of imposed patterns by metal wires.

In another interesting simulation, a metal sheet with four small square holes was placed below the top electrode of a magnetized plasma. The width of the square holes is *1.4 mm* and the background plasma density is 5.0 $\times 10^{14}\ m^{-3}$, applied magnetic field is *1.0 T*, and pressure is $P = 12\ Pa$. Figure 5.2 shows the X-Y cross section of the electron density profile in the middle of the plasma chamber for this simulation. The small holes in the metal sheet break the symmetry of the configuration and act as the seeds for the formation of target like filamentary structures in the magnetized plasma. For the simulation of filamentation phenomenon, an initial perturbation in form of a high-density column was added to the background plasma to initiate the formation of

filamentary structures. This observation can be further investigated in experiments. It can be considered as a method for generating controlled filamentary patterns.

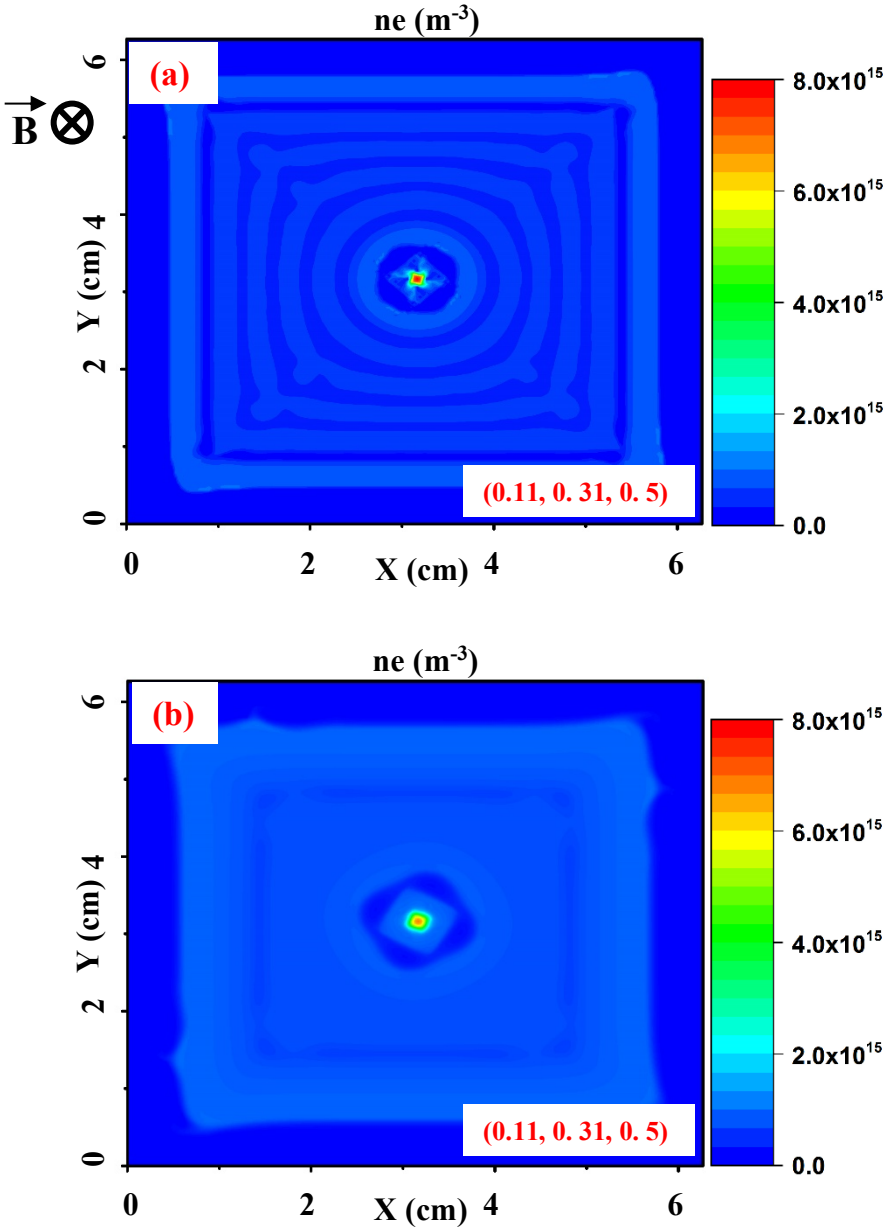

Figure 5.1: X-Y cross-section of electron density profile in magnetized argon plasma at pressure of $P = 19\ Pa$, $T_e = 2.5\ ev$, $T_i = 0.025\ ev$, and $ne = ni = 5 \times 10^{14}\ m^{-3}$, exposed to $B = 2.0\ T$ magnetic field. a) All walls of the chamber are metallic with full absorption of incoming electrons/ions. b) Allowing electrons/ions to accumulate in a few layers at the bottom of the chamber. The accumulation of the charged particles prevents the formation of filamentary patterns in the magnetized plasma.

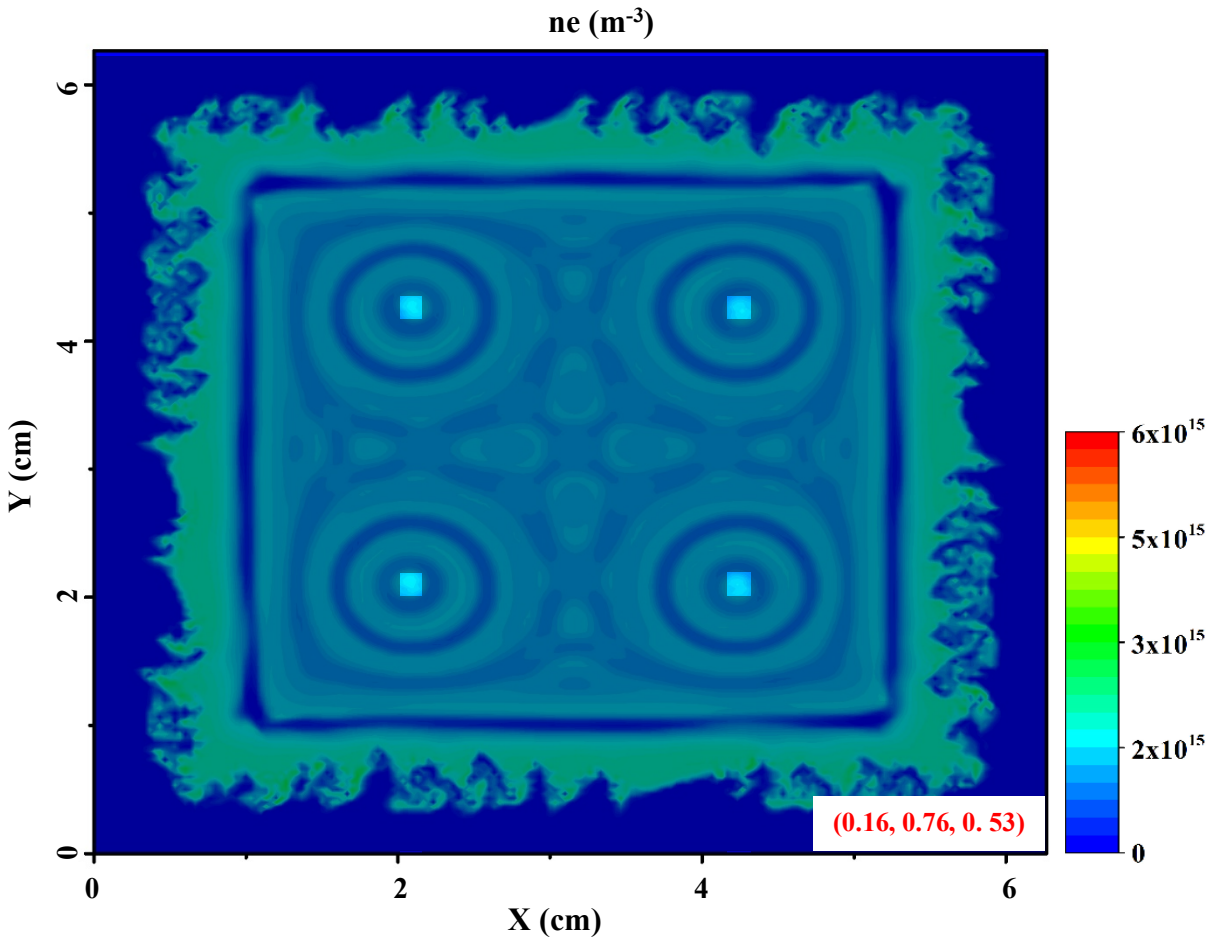

Figure 5.2: X-Y cross section of electron density profile in a magnetized argon plasma in presence of a metal sheet with four small square holes, placed below the top electrode. The width of the square holes *1.4* mm. The background plasma density is 5.0 $\times 10^{14}$ m^{-3}, applied magnetic field is *1.0 T*, and pressure is *P = 12 Pa*. The small holes in the metal sheet break the symmetry of the configuration and cause the formation of filamentary structures in the magnetized plasma without adding an initial perturbation to it. The dark mask on the graph indicates the location of the metal sheet.

References

[1] M. Menati, E. Thomas, and M. J. Kushner, Phys. Plasmas **26**, 063515 (2019).

[2] M. Menati, B. Rasoolian, E. Thomas, and U. Konopka, Phys. Plasmas **27**, 022101 (2020).

[3] M. Menati, T. Hall, B. Rasoolian, L. Couedel, E. Thomas, and U. Konopka, Plasma Sources Sci. Technol. **29**, (2020) https://doi.org/10.1088/1361-6595/aba7ed.

[4] E. Thomas, B. Lynch, U. Konopka, M. Menati, S. Williams, R. L. Merlino, and M. Rosenberg, Plasma Phys. Control. Fusion **62**, 014006 (2020).

[5] S. Jaiswal, M. Menati, L. Couëdel, V. H. Holloman, V. Rangari, and E. Thomas, Jpn. J. Appl. Phys. **59**, SHHC07 (2020).

[6] M. A. Lieberman and A. J. Lichtenberg, *Principles of Plasma Discharges and Materials Processing* (John Wiley & Sons, Inc., Hoboken, NJ, USA, 2005).

[7] F. F. Chen, *Introduction to Plasma Physics and Controlled Fusion* (Springer International Publishing, Cham, 2016).

[8] A. Piel and A. Melzer, Adv. Sp. Res. **29**, 1255 (2002).

[9] A. Piel and A. Melzer, Plasma Phys. Control. Fusion **44**, R1 (2002).

[10] P. K. Shukla, Phys. Plasmas **8**, 1791 (2001).

[11] R. L. Merlino and J. A. Goree, Phys. Today **57**, 32 (2004).

[12] A. Barkan, N. D'Angelo, and R. L. Merlino, Phys. Rev. Lett. **73**, 3093 (1994).

[13] B. Walch, M. Horanyi, and S. Robertson, IEEE Trans. Plasma Sci. **22**, 97 (1994).

[14] E. Thomas and M. Watson, Phys. Plasmas **7**, 3194 (2000).

[15] E. Thomas, R. L. Merlino, and M. Rosenberg, Plasma Phys. Control. Fusion **54**, 124034 (2012).

[16] E. Thomas, R. Merlino, and M. Rosenberg, Plasma Sci. IEEE Trans. **41**, 811 (2013).

[17] G. T. Birk and H. Wiechen, Phys. Plasmas **9**, 964 (2002).

[18] S. K. Tiwari, A. Das, D. Angom, B. G. Patel, and P. Kaw, Phys. Plasmas **19**, 073703 (2012).

[19] G. I. Kent, Phys. Fluids **12**, 2140 (1969).

[20] S. Nunomura, N. Ohno, and S. Takamura, Jpn. J. Appl. Phys. **36**, 877 (1997).

[21] M. Salimullah, I. Sandberg, and P. K. Shukla, Phys. Rev. E **68**, 027403 (2003).

[22] M. Salimullah and M. Muniruzzaman, Phys. Scr. **60**, 171 (1999).

[23] U. Konopka, in *AIP Conf. Proc.* (AIP, 2005), pp. 181–184.

[24] M. Schwabe, U. Konopka, P. Bandyopadhyay, and G. E. Morfill, Phys. Rev. Lett. **106**, 215004 (2011).

[25] E. Thomas, U. Konopka, R. L. Merlino, and M. Rosenberg, Phys. Plasmas **23**, 055701 (2016).

[26] E. Thomas, U. Konopka, B. Lynch, S. Adams, S. LeBlanc, R. L. Merlino, and M. Rosenberg, Phys. Plasmas **22**, 113708 (2015).

[27] E. Thomas, B. Lynch, U. Konopka, R. L. Merlino, and M. Rosenberg, Phys. Plasmas **22**, 030701 (2015).

[28] T. Hall, E. Thomas, K. Avinash, R. Merlino, and M. Rosenberg, Phys. Plasmas **25**, 103702 (2018).

[29] M. Cross and H. Greenside, *Pattern Formation and Dynamics in Nonequilibrium Systems* (Cambridge University Press, Cambridge, 2009).

[30] M. Rietkerk and J. van de Koppel, Trends Ecol. Evol. **23**, 169 (2008).

[31] J. Mar. Biol. Assoc. United Kingdom **75**, 1004 (1995).

[32] B. Liebchen, D. Marenduzzo, I. Pagonabarraga, and M. E. Cates, Phys. Rev. Lett. **115**,

258301 (2015).

[33] K. Agladze, L. Budriene, G. Ivanitsky, V. Krinsky, V. Shakhbazyan, and M. Tsyganov, Proc. R. Soc. London. Ser. B Biol. Sci. **253**, 131 (1993).

[34] V. V. Bel'kov, J. Hirschinger, V. Novák, F.-J. Niedernostheide, S. D. Ganichev, and W. Prettl, Nature **397**, 398 (1999).

[35] R. Kapral, Phys. D Nonlinear Phenom. **86**, 149 (1995).

[36] P. Drazin, and J. Crepeau, Appl. Mech. Rev. **56**, B43 (2003).

[37] R. D. Deegan, Phys. Rev. E **61**, 475 (2000).

[38] K. C. Wali, in *A Quest Perspect.* (IMPERIAL COLLEGE PRESS, 2001), pp. 531–649.

[39] H. Brandtstädter, M. Braune, I. Schebesch, and H. Engel, Chem. Phys. Lett. **323**, 145 (2000).

[40] F. G. Baksht, G. A. Dyuzhev, N. K. Mitrofanov, and S. M. Shkol'nik, Tech. Phys. **42**, 35 (1997).

[41] S. Zhang and T. Dufour, Phys. Plasmas **25**, 073502 (2018).

[42] G. Yang and J. Heberlein, Plasma Sources Sci. Technol. **16**, 765 (2007).

[43] D. Schuocker, IEEE Trans. Plasma Sci. **7**, 209 (1979).

[44] M. Wagner, A. Kohut, Z. Geretovszky, M. Seipenbusch, and G. Galbács, J. Aerosol Sci. **93**, 16 (2016).

[45] G. A. Dyuzhev, G. A. Lyubimov, and S. M. Shkol'Nik, IEEE Trans. Plasma Sci. **11**, 36 (1983).

[46] T. Verreycken, P. Bruggeman, and C. Leys, J. Appl. Phys. **105**, 083312 (2009).

[47] H.-G. Purwins, IEEE Trans. Plasma Sci. **39**, 2112 (2011).

[48] H.-G. J. Purwins and J. Berkemeier, IEEE Trans. Plasma Sci. **39**, 2116 (2011).

[49] U. Ebert, W. van Saarloos, and C. Caroli, Phys. Rev. Lett. **77**, 4178 (1996).

[50] U. Ebert and M. Arrayás, in *Pattern Form. Electr. Discharges* (2001), pp. 270–282.

[51] B. Li and J. Ouyang, Phys. Plasmas **23**, 113509 (2016).

[52] L. F. Dong, W. L. Fan, S. Wang, Y. F. Ji, Z. W. Liu, and Q. Chen, Phys. Plasmas **18**, 033506 (2011).

[53] S. N. Abolmasov, T. Shirafuji, and K. Tachibana, IEEE Trans. Plasma Sci. **33**, 941 (2005).

[54] A. Chirokov, A. Gutsol, A. Fridman, K. D. Sieber, J. M. Grace, and K. S. Robinson, Plasma Chem. Plasma Process. **26**, 127 (2006).

[55] J. P. Trelles, J. Phys. D. Appl. Phys. **49**, 393002 (2016).

[56] Y. Amagishi, Y. Yoshikawa, and J. Ohara, J. Phys. Soc. Japan **60**, 2496 (1991).

[57] W. Sun, J. Y. Zhong, S. Zhang, B. W. Tong, L. F. Wang, K. G. Zhao, J. Y. Liu, B. Han, B. J. Zhu, D. W. Yuan, X. X. Yuan, Z. Zhang, Y. T. Li, Q. Zhang, J. M. Peng, J. Z. Wang, Y. L. Ping, C. Q. Xing, H. G. Wei, G. Y. Liang, Z. Y. Xie, C. Wang, G. Zhao, and J. Zhang, High Energy Density Phys. **31**, 47 (2019).

[58] T. Ikehata, H. Tanaka, N. Y. Sato, and H. Mase, Phys. Rev. Lett. **81**, 1853 (1998).

[59] C. F. Driscoll, D. A. Schecter, D. Z. Jin, D. H. E. Dubin, K. S. Fine, and A. C. Cass, Phys. A Stat. Mech. Its Appl. **263**, 284 (1999).

[60] R. KEPPENS, G. TÓTH, R. H. J. WESTERMANN, and J. P. GOEDBLOED, J. Plasma Phys. **61**, 1 (1999).

[61] M. Kono and M. Y. Tanaka, Phys. Rev. Lett. **84**, 4369 (2000).

[62] M. Kono, H. L. Pécseli, and J. Trulsen, Phys. Scr. **61**, 489 (2000).

[63] M. Schwabe, Microparticles as Probes in a Highly Magnetized Dusty Plasma,

Diplomarbeit, Technical University of Munich (TUM), 2006.

[64] P. Bandyopadhyay, D. Sharma, U. Konopka, and G. Morfill, in *AIP Conf. Proc.* (2014), pp. 281–287.

[65] R. L. Merlino, E. Thomas, B. Lynch, S. LeBlanc, T. Hall, U. Konopka, and M. Rosenberg, in *AIP Conf. Proc.* (2018), p. 020011.

[66] H. Ikezi, Phys. Fluids **29**, 1764 (1986).

[67] A. Melzer, A. Homann, and A. Piel, Phys. Rev. E **53**, 2757 (1996).

[68] R. A. Quinn and J. Goree, Phys. Plasmas **7**, 3904 (2000).

[69] O. S. Vaulina, I. E. Drangevski, X. G. Adamovich, O. F. Petrov, and V. E. Fortov, Phys. Rev. Lett. **97**, 195001 (2006).

[70] V. Nosenko, S. Zhdanov, A. V. Ivlev, G. Morfill, J. Goree, and A. Piel, Phys. Rev. Lett. **100**, 025003 (2008).

[71] D. Samsonov, A. V. Ivlev, R. A. Quinn, G. Morfill, and S. Zhdanov, Phys. Rev. Lett. **88**, 095004 (2002).

[72] T. E. Sheridan, V. Nosenko, and J. Goree, Phys. Plasmas **15**, 073703 (2008).

[73] J. H. Chu and L. I, Phys. Rev. Lett. **72**, 4009 (1994).

[74] H. Thomas, G. E. Morfill, V. Demmel, J. Goree, B. Feuerbacher, and D. Möhlmann, Phys. Rev. Lett. **73**, 652 (1994).

[75] Y. Hayashi and K. Tachibana, Jpn. J. Appl. Phys. **33**, L804 (1994).

[76] C. K. Goertz, Rev. Geophys. **27**, 271 (1989).

[77] T. W. Hartquist, W. Pilipp, and O. Havnes, Astrophys. Space Sci. **246**, 243 (1996).

[78] L. Mestel and L. Spitzer, Mon. Not. R. Astron. Soc. **116**, 503 (1956).

[79] M. Horányi, J. R. Szalay, S. Kempf, J. Schmidt, E. Grün, R. Srama, and Z. Sternovsky,

Nature **522**, 324 (2015).

[80] M. Horanyi, G. Morfill, and E. Grün, Nature **363**, 144 (1993).

[81] M. Horanyi and D. A. Mendis, Astrophys. J. **294**, 357 (1985).

[82] D. A. Mendis and M. Horányi, Rev. Geophys. **51**, 53 (2013).

[83] J. Pelletier, Plasma Phys. Control. Fusion **42**, 227 (2000).

[84] U. de Angelis, Phys. Plasmas **13**, 012514 (2006).

[85] J. Winter, Plasma Phys. Control. Fusion **40**, 1201 (1998).

[86] H. Kobayashi, Jpn. J. Appl. Phys. **50**, 08JE01 (2011).

[87] M. Santos, B. Reeves, P. Michael, R. Tan, S. G. Wise, and M. M. M. Bilek, Commun. Phys. **2**, 52 (2019).

[88] U. R. Kortshagen, R. M. Sankaran, R. N. Pereira, S. L. Girshick, J. J. Wu, and E. S. Aydil, Chem. Rev. **116**, 11061 (2016).

[89] E. Thomas, J. Plasma Fusion Res. **93**, 1 (2017).

[90] I. V. Schweigert and M. Keidar, J. Phys. Conf. Ser. **927**, 012048 (2017).

[91] J. Nickolls, I. Buck, M. Garland, and K. Skadron, Queue **6**, 40 (2008).

[92] A. Hecimovic and A. von Keudell, J. Phys. D. Appl. Phys. **51**, 453001 (2018).

[93] R. Kawashima, K. Hara, and K. Komurasaki, Plasma Sources Sci. Technol. **27**, 035010 (2018).

[94] M. J. Kushner, J. Phys. D. Appl. Phys. **42**, 194013 (2009).

[95] S.-H. Song, Y. Yang, P. Chabert, and M. J. Kushner, Phys. Plasmas **21**, 093512 (2014).

[96] Y. Tomita, R. Smirnov, and S. Zhu, Plasma Sci. Technol. **7**, 2657 (2005).

[97] N. Sternberg, V. Godyak, and D. Hoffman, Phys. Plasmas **13**, 063511 (2006).

[98] A. R. Niknam, T. Haghtalab, and S. M. Khorashadizadeh, Phys. Plasmas **18**, 113707

(2011).

[99] L. C. Pitchford, L. L. Alves, K. Bartschat, S. F. Biagi, M. C. Bordage, A. V. Phelps, C. M. Ferreira, G. J. M. Hagelaar, W. L. Morgan, S. Pancheshnyi, V. Puech, A. Stauffer, and O. Zatsarinny, J. Phys. D. Appl. Phys. **46**, 334001 (2013).

[100] M. C. Bordage, S. F. Biagi, L. L. Alves, K. Bartschat, S. Chowdhury, L. C. Pitchford, G. J. M. Hagelaar, W. L. Morgan, V. Puech, and O. Zatsarinny, J. Phys. D. Appl. Phys. **46**, 334003 (2013).

[101] L. L. Alves, K. Bartschat, S. F. Biagi, M. C. Bordage, L. C. Pitchford, C. M. Ferreira, G. J. M. Hagelaar, W. L. Morgan, S. Pancheshnyi, A. V. Phelps, V. Puech, and O. Zatsarinny, J. Phys. D. Appl. Phys. **46**, 334002 (2013).

[102] D. B. Graves and K. F. Jensen, IEEE Trans. Plasma Sci. **14**, 78 (1986).

[103] Y. Oh, N. Choi, and D. Choi, J. Appl. Phys. **67**, 3264 (1990).

[104] M. H. Wilcoxson and V. I. Manousiouthakis, IEEE Trans. Plasma Sci. **21**, 213 (1993).

[105] A. Bogaerts, R. Gijbels, and W. J. Goedheer, J. Appl. Phys. **78**, 2233 (1995).

[106] H. Akashi, Y. Sakai, N. Takahashi, and T. Sasaki, J. Phys. D. Appl. Phys. **32**, 2861 (1999).

[107] S. Medina, K. Yanallah, L. Mehdaoui, A. Belasri, and T. Baba-Hamed, Plasma Devices Oper. **13**, 1 (2005).

[108] A. Derzsi, P. Hartmann, I. Korolov, J. Karácsony, G. Bánó, and Z. Donkó, J. Phys. D. Appl. Phys. **42**, 225204 (2009).

[109] T. Samir, Phys. Plasmas **21**, 083511 (2014).

[110] S. I. Eliseev, E. A. Bogdanov, and A. A. Kudryavtsev, Phys. Plasmas **24**, 093503 (2017).

[111] M. N. O. Sadiku, *Numerical Techniques in Electromagnetics with MATLAB®* (CRC

Press, 2015).

[112] E. Alberto and O. Sigmund, Lat. Am. J. Solids Struct., **1**, 169 (2004).

[113] M. A. Onabid, African J. Math. Comput. Sci. Res. **5**, 204 (2012).

[114] M. S. Barnes, T. J. Cotler, and M. E. Elta, J. Comput. Phys. **77**, 53 (1988).

[115] A. C. Jones and T. P. Downes, Mon. Not. R. Astron. Soc. **418**, 390 (2011).